JOURNAL OF GEOPHYSICAL RESEARCH, VOL. 92, NO. C5, PAGES 4971–5029, MAY 15, 1987

Radar Scattering and Equilibrium Ranges in Wind-Generated Waves With Application to Scatterometry

MARK A. DONELAN

National Water Research Institute, Canada Centre for Inland Waters, Burlington, Ontario

WILLARD J. PIERSON, JR.

Institute of Marine and Atmospheric Sciences, The City College, City University of New York

A composite divided scale model for radar backscatter from the ocean surface is constructed. The primary scattering mechanism is assumed to be Bragg scattering for which the normalized radar backscattering cross section is proportional to the spectral density of the resonant Bragg water waves. The form of the high-wave number equilibrium spectrum is derived on the assumption that the shortwave energy density reflects a balance between direct wind forcing and dissipation due to breaking and to viscosity. This theoretical equilibrium spectrum links the wave spectrum to the wind. This spectrum is then used in a two-scale Bragg-scattering model to link backscattering cross section to the full wave spectrum, which is this high-wave number spectrum plus a gravity wave spectrum for fully developed seas. The effects of tilt and modulation of the Bragg resonant waves by the longer waves are included along with the contribution from specular reflection at low incidence angles. The model is tested against aircraft circle flight K_u band radar backscatter measurements with encouraging results for vertical polarization. It is demonstrated that particularly at low wind speeds, scatterometry is sensitive to surface water temperature through its effect on the viscous dissipation of short waves. Also for low wind speeds and low incidence angles (20° or so) an additional source of specular backscatter needs to be considered: that due to gravity waves that may be left over from previously higher winds or that enter the area as swell. For high incidence angles and high winds, the two-scale Bragg model yields values that are somewhat low compared with the data for vertical polarization. For horizontal polarization the model is somewhat low for a 40° incidence angle and much too low for higher incidence angles by amounts that cannot be explained by a combination of possible wind speed measurement errors and bias errors in the measurement of the backscatter. An explanation for these results is offered in terms of recent studies of backscatter from wedges and spilling breakers for K_u band. The model is then exercised over a much wider wind speed range from L band to K_a band. For high wind speeds at anemometer height, except at L band, according to the model, the backscattering cross section becomes less sensitive to wind speed and at very high speeds decreases as the wind speed increases. The wind speed at which this "rollover" occurs is dependent on radar wavelength and incidence angle, being as low as 30 m s^{-1} for K_u band for vertical polarization at some incidence angles. The effect of wedges and breakers may overcome the predicted "rollover," especially for horizontal polarization, but there are data to support a tendency toward saturation for vertical polarization at perhaps a somewhat higher wind speed. The two-scale model does not appear to be sensitive to variations in the slopes of the tilting waves that would be present for nonfully developed seas. The number and size of wedges and spilling breakers will be a function of fetch and duration and, along with sea surface temperature effects, will need to be incorporated in models that recover wind speed and direction from scatterometer measurements. This rather complicated dependence of radar backscatter on wind speed, water temperature, and fetch and duration dependent wave properties contrasts strongly with current power law models. Some of the inconsistencies that have arisen in the analysis of scatterometer data to date are explained.

CONTENTS

Paper number 6C0679.
0148-0227/87/006C-0679$05.00

1. INTRODUCTION

1.1. *Present Status*

The demonstration that satellite-borne instruments can yield information on marine surface winds is an extremely important advance in remote sensing. The stated objectives of the Seasat-A satellite scatterometer (SASS) program appeared at first to have been met (*Journal of Geophysical Research*, volume 87, number C5, and volume 88, number C3), but more recent studies, including this paper, raise doubts. The absence of conventional data made the Seasat SASS–derived wind data, though now questionable, of great value in many applications [*Peteherych et al.*, 1984; *Duffy and Atlas*, 1986; *Pierson et al.*, 1984; *Ross et al.*, 1985; *Black et al.*, 1985; *Woiceshyn et al.*, 1985].

The instruments used for this purpose are active microwave devices operating at GHz frequencies called scatterometers. To date, efforts have been devoted to making anemometers of scatterometers by the empirical determination of transfer functions, i.e., equations of the form $\sigma^0 = \sigma^0\ (\bar{U}, \chi, \theta)$, relating normalized backscattered power to some aspect of the surface wind vector $\bar{U}(19.5)$, the radar incidence angle θ, and the wind direction relative to the radar beam direction, χ. Most of the work has been based on regarding the effective neutral wind at 19.5-m height as the basic sensed variable [*Moore and Fung*, 1979; *Jones et al.*, 1982; *Pierson and Salfi*, 1982; *Schroeder et al.*, 1982*a*, *b*; *Pierson*, 1983], though the friction velocity has not escaped attention [*Jones and Schroeder*, 1978; *Liu and Large*, 1981; *Brown*, 1983].

In a recent paper, *Woiceshyn et al.* [1986] have shown that the transfer (or model) functions used for horizontal incident–horizontal scattered polarization (electric field vector perpendicular to the plane of incidence, abbreviated HH) are inconsistent with those used for vertical-vertical polarization (abbreviated *VV*). The differences in estimated wind speeds are quite large (up to 9 m s^{-1} for high winds) and imply perhaps that the process of deducing the wind from the backscatter measurements was partially incorrect, that the model functions, $\sigma_{VV}{}^0(\bar{U}, \chi, \theta)$ and $\sigma_{HH}{}^0(\bar{U}, \chi, \theta)$, when combined with the sum of squares (SOS) wind recovery algorithm [*Jones et al.*, 1982; *Pierson*, 1984] were in error; or that a combination of both caused the discrepancies. Both model functions were determined empirically in the same way. A power law wind speed dependence was assumed over a restricted midrange of surface wind speeds (5 to 16 m s^{-1}) from the Joint Air-Sea Interaction (JASIN) program, for which good surface observations were available. The then available National Aeronautics and Space Administration (NASA) circle flight data [*Jones et al.*, 1977] were also used. The approach taken by *Woiceshyn et al.* [1986] is novel and very valuable, for it avoids the slippery question of the quality or suitability of a particular set of surface data used in verifying the scatterometer's anemometry and demonstrates the internal inconsistency of the methods that were used.

The results of this internal *HH-VV* comparison, especially for strong winds, call for a new look at the basis for scatterometer-anemometry, and Woiceshyn et al. point out that there is a need for a new model to relate backscatter to the winds.

In a recent paper, *Donelan and Pierson* [1984], hereinafter referred to as DP1 (see also *Pierson et al.* [1986]), demonstrate that the wind parameter most closely related to microwave Bragg scattering is the wind very near the surface at a height of the order of the wavelength of the Bragg resonant water wave. Frequency spectra of short but distinctly gravity waves (wavelength $\lambda = 20.7$ cm) are used to support the analysis. The results are therefore of value in the interpretation of L band synthetic aperture data. In particular, DP1 demonstrated that neither wind speed $\bar{U}(19.5)$ nor friction velocity u_* is uniquely related to the wave spectral density, $\Phi(\omega)$ when data for various states of wave development are considered. A closer relationship between the normalized spectrum $\Phi(\omega)\omega^5/g^2$ and $\{[(\bar{U}(\pi g/\omega^2))\omega/g] - 1\}$ was shown. DP1 indicated a possible new approach to scatterometry but did not attempt to verify the approach using actual backscatter observations.

1.2. *Extension of Previous Research*

In this paper we extend the ideas presented by DP1 for frequency spectra to wave number spectra. We obtain a theoretical form for the high-wave number spectrum that requires some empirically determined constants. The theoretical equilibrium spectrum links the waves to the wind. This spectrum is included in a two-scale Bragg scattering model to relate backscattering cross section first to the wave spectrum and then to the wind that generated the waves. Some interesting results on the relationship between backscatter and wind emerge from this analysis.

The low–wave number (gravity wave) part of the spectrum is for a fully developed wind-generated sea. It is used to calculate the required slope variances for a two-scale model. Such a model has shortcomings for both light winds and high winds because the gravity waves on the ocean are usually higher than the corresponding fully developed sea when winds are light and lower than the corresponding fully developed sea when winds are high. Ways to take these effects into account are given.

Observational results on wave growth and physical reasoning lead to a form of the wave number spectrum for capillary-gravity waves (wave number $k = 2\pi/\lambda$ in the range 10^{-1} to 10^{+1} cm^{-1}, which is in accord with observations. The dependence of spectral density on surface wind is deduced and demonstrates that power law model functions are inadequate and will in general underestimate the wind speed at both low and high speeds and overestimate the wind speed for the midrange of speeds.

The predicted *VV* and *HH* normalized backscatter cross sections $\sigma_{VV}{}^0(\bar{U}, \chi, \theta)$ are compared with the circle flight data from *Schroeder et al.* [1984]. They yield the observed microwave frequency, incidence angle, wind speed, and direction dependence for vertical polarization. However, the *HH* backscatter $\sigma_{HH}{}^0(\bar{U}, \chi, \theta)$ is much more sensitive to whitecapping and wave steepness.

Our results are a blend of theory and empiricism. The empiricism is based on the analysis of wave data so as to determine the properties of the gravity wave spectra to be used in a two-scale model. The properties of capillary-gravity wave spectra are deduced from a theoretical balance of wave amplification by direct wind forcing and wave attenuation by dissipative processes. The conventional method of trying to fit backscatter to a power law for wind speed (or friction velocity) by regression techniques depends too much on empiricism and is incapable of coping with the very complex physical processes involved in the generation of an equilibrium wave spectrum for a given wind speed. This is especially true in attempting to understand the effects of viscosity and to cover the entire range of radar wave numbers from *L* band to K_a band. The power law empirical model is the weak point of all previous efforts to relate backscatter to wind.

The assumption that backscatter must increase by the same amount in decibels as the wind at 19.5 m increases from 1 to 2 m s^{-1}, from 4 to 8 m s^{-1}, from 16 to 32 m s^{-1}, and from 64 to 128 m s^{-1} (impossible) must fail for some winds over this range even for a constant viscosity. Our results show that this assumption fails for all wind ranges, but especially for light winds, and that it may well fail for high winds of even greater importance. The effect of viscosity is important for the recovery of a correct wind for all wind speeds.

1.3. *Previous Work on Two-Scale Models*

It has been clearly established that the backscattered power for incidence angles well away from nadir and grazing (i.e., approximately 25° to 65°) is largely due to Bragg resonance. The theory has been developed by *Rice* [1951], *Valenzuela* [1968], and others; see *Valenzuela* [1978] for a review. *Wright* [1966] has shown that the scattering cross section is proportional to wave height squared of monochromatic waves. It was later shown [*Wright and Keller*, 1971; *Keller and Wright*, 1975] that first-order Bragg scattering theory is appropriate in the capillary-gravity region at midrange incidence angles in the absence of longer and higher gravity waves that tilt the surface on which the "Bragg scatterers" ride.

For a first-order Bragg theory for radar backscatter to depend on wind speed, wind direction, and incidence angle at, say, K_u band, the wave number spectrum for water wavelengths from about 2.5 cm to about 1 cm must be a function of wind speed and the direction of travel of the waves relative to the mean wind direction. The joint probability density function of the upwind and crosswind slopes of the longer waves in the wave number spectrum must be known as a function of wind speed in order to use a two-scale Bragg-scattering theory. Two-scale theories as in the review by *Valenzuela* [1978] thus require some knowledge of the slopes of the longer waves as a function of wind speed and detailed knowledge of that portion of the spectrum appropriate to Bragg scattering.

The methodology used closely parallels the work of *Chan and Fung* [1977] and *Fung and Lee* [1982]. However, it is based on newly derived theories, verified in part by experiment, on the growth and equilibrium form of the wave number spectrum for the Bragg-scattering waves and on a different model for the slope of the longer waves.

Fung and Lee [1982] have provided a model based on the spectrum proposed by *Pierson and Moskowitz* [1964] as extended (with corrections by *Bjerkaas and Riedel* [1979]) to higher wave numbers by *Pierson and Stacy* [1973] so as to include the measurements of the spectra of high-frequency waves by *Mitsuyasu and Honda* [1975]. *Fung and Lee* [1982] also include the result of Pierson and Stacy concerning the absence of a wave spectrum below a wind corresponding to a friction velocity of about 12 cm s^{-1}.

For numerous reasons, backscatter models based on these results can now be questioned because of more recent scientific measurements and theories. A saturated spectrum, independent of wind speed, at high gravity wave numbers of the form Bk^{-4} modified to include direction effects, is no longer tenable.

The results to follow show that the high-wave number capillary-gravity part of the spectrum is not simply a function of wind speed. It is also a function of sea surface temperature and salinity because of the variation of the viscosity of water with temperature and salinity. Thus the solely wind speed dependent spectra used by Fung and Lee, as for example in their Figures 1 and 2, are inadequate. Our results indicate that entire families of spectra exist as a function of wind speed when the effect of viscosity is included.

There are other differences between the methods used by Fung and Lee and the results to follow (the form for the angular spreading of the spectrum, for example).

An important result of *Chan and Fung* [1977] is that the probability density function for the slopes of the longer waves that tilt the Bragg waves as referred to the level sea surface is corrected for the effect of off nadir angles. Our results include this effect and also take into account shadowing for all aspect angles.

The equilibrium spectrum for the Bragg wave numbers requires the determination of two parameters so as to provide a balance between energy from the wind and dissipation as a result of breaking, microbreaking, and viscosity. The angular spread of the Bragg wave number spectrum must also be adjusted to fit the cross-wind data. Two parameters related to the modulation of short waves by long waves are also needed.

Papers by *Wentz* [1977, 1978] and *Wentz et al.* [1984, 1986] have also been concerned with the development of a two-scale scattering model. These papers differ from the work of *Chan and Fung* [1977] and *Fung and Lee* [1982] and the results to follow in that specific forms for the Bragg-scattering part of the wave number spectrum are not given and equations that relate the wave spectra and the slopes of the longer waves to the backscatter are not used. Two-scale backscatter theory is used as a rationale to justify the methods that were used to fit backscatter measurements to a function of incidence angle, aspect angle, and either wind speed or friction velocity. In one way or another, depending on the choice of $\bar{U}(19.5)$ or u_* with either some assumed neutral drag coefficient C_{DN} or $z_0 = z_0(u_*)$ closure, these papers eventually all reduce to some form of a regression analysis of backscatter values in bels or decibels against a straight line, more or less, in log-log space with $\log_{10} \bar{U}(19.5)$ or $\log_{10} u_*$ as the other variable and coefficients, perhaps weakly dependent on wind speed, to be determined as a function of aspect angle and incidence angle.

The backscatter model proposed by *Wentz et al.* [1984, 1986] is a variation of the concepts used for the SASS 1 model function that was used for the recovery of winds from Seasat SASS data by means of the sum of squares algorithm as described by *Jones et al.* [1982] and *Schroeder et al.* [1982*b*]. As in the work of *Britt and Schroeder* [1984], the power law model is introduced into the analysis of the data in such a way that the subtleties of the relationship between the waves that cause the backscatter and the backscatter are lost. The effect of viscosity (which is not treated in any of these analyses); the generally poor quality of the wind measurements by conventional means, and the random fluctuations of the backscatter measurements about their expected value, in a statistical sense, all then combine to produce variations from one power law fit to another that depend upon the actual data base that was used, the particular form of the regression equations that were used, and the analytical form that was used for the aspect angle dependence. A comparison of the power laws given by *Wentz et al.* [1984], *Britt and Schroeder* [1984], *Schroeder et al.* [1982*b*], and *Schroeder et al.* [1984] shows wide variations from one fit to another, especially for the higher incidence angles. See for example, Figure 4 of *Schroeder et al.* [1984] on pages 95 to 100 of that reference.

Other recent models for a two-scale theory are those of *Plant* [1986] and *Durden and Vesecky* [1985]. These models differ from ours in the form of the wave number spectrum, especially at the Bragg wave numbers, and in the way the spectrum is assumed to vary about the mean wind direction. The assumptions that are made for these different models need to be compared with the assumptions made in the model to be developed in this paper.

1.4. *Wedges and Spilling Breakers*

Nonlinear theories for random short-crested wind-generated waves are at best third- or fourth-order perturbation expansions that do not model important properties of actual waves. Two of these properties of importance to radar backscatter are the wedgelike shapes of wave crests with an interior angle of about 120° just before those particular portions of the waves break and the spilling breakers that occur after the waves break. Very high order Fourier expansions would be needed to produce a wedge. Spilling breakers no longer satisfy the equations usually used to describe wind-generated waves, but their properties have been investigated by *Longuet-Higgins and Turner* [1974] and *Banner* [1985], who have developed models for a spilling breaker.

Radar backscatter from wedges has been treated theoretically by *Lyzenga et al.* [1983] and experimentally and theoretically by *Kwoh and Lake* [1984]. *Wetzel* [1986] has developed several theoretical aspects of backscatter from the hydraulic jump at the toe of a spilling breaker based on the work of *Longuet-Higgins and Turner* [1974]. *Banner and Fooks* [1985] have measured backscatter from a spilling breaker. A two-scale Bragg-scattering model does not include these additional effects, which appear to be important at high incidence angles especially for horizontal polarization. The discrepancies at high incidence angles between the model developed in this paper and the observations can probably be explained by a combination of possible bias errors in the measurements and by estimates of the effects of backscatter from wedges and spilling breakers when backscatter is measured from aircraft and spacecraft altitudes. In section 10 we review these results and demonstrate that the addition of backscatter due to breakers and wedges, in an amount consistent with independent experiments, removes these discrepancies.

1.5. *Data Source for K_u Band*

The data to be used for a preliminary verification of the model are subsets of the Advanced Applications Flight Experiment (AAFE) Langley radiometer scatterometer (RADSCAT) circle flight data reported by *Schroeder et al.* [1984]. The criterion for selection of the primary data set was that the correlation coefficient R^2 be greater than 0.5 for the vertically polarized data. This subset, to be described in detail subsequently, consists of backscatter and environmental data for 24 vertically polarized circle flights and 23 horizontally polarized circle flights. Data for *HH* polarization for mission 318, flight 19, line 4, run 17, are missing. The objective is to determine the unknown wind wave parameters as a function of the winds and the waves they generated and to predict from the model the backscatter values given in the tabulations of *Schroeder et al.* [1984]. We also used the data for 29 additional circle flights as a supplementary set to illustrate other properties of our model, including important effects at low incidence angles.

2. WIND FORCING

2.1. *Field and Laboratory Studies of Wave Growth*

Various attempts have been made to estimate the wind input to waves by measuring the pressure at or near the surface. The growth rates of the well-known Bight of Abaco experiment [*Snyder et al.*, 1981] are approximated by

$$\left(\frac{1}{\omega\Phi}\frac{\partial\Phi}{\partial t}\right)\frac{\rho_w}{\rho_a} = \frac{\beta}{\omega}\frac{\rho_w}{\rho_a} \cong (0.2 \text{ to } 0.3)(\mu_1 - 1) \qquad (1)$$

for $1 < \mu_1 < 4$, where Φ is the energy spectrum $\Phi(\omega)$, β is the exponential growth rate, ω is the radian frequency, ρ_a and ρ_w are air and water densities, $\mu_1 = \bar{U}(5) \cos \chi/C$, C is the phase speed, $\bar{U}(5)$ is the mean wind at 5-m height, and χ is the angle between the propagation direction of waves and wind.

The more recent field experiments of *Hasselmann et al.* [1983] and *Hsiao and Shemdin* [1983] show a stronger than linear dependence of β/ω on $(\mu - 1)$. Hsiao and Shemdin's data cover a larger range of $\mu_2 (1 < \mu_2 < 7.4)$ than the previous field experiments. They find that β/ω depends quadratically on

$(\mu_2 - 1)$:

$$\frac{\beta}{\omega}\frac{\rho_w}{\rho_a} = 0.12(\mu_2 - 1)^2 \qquad (2)$$

for $1 < \mu_2 < 7.4$ and where $\mu_2 = 0.85\bar{U}(10) \cos \chi/C$.

Hsiao and Shemdin [1983] point out that within experimental scatter, (2) is an adequate representation of the data that led to (1).

Plant [1982] has shown that β/ω values from several laboratory and field experiments are quadratically dependent on $\mu_*(=u_*(\cos^{1/2} \chi)/C)$ over a wide range of μ_*:

$$\frac{\beta}{\omega} = 0.04\ \mu_*^2 \qquad (3)$$

in agreement with the theory of *Miles* [1959]. However, this relationship fails at small values of μ_* corresponding to μ_1, μ_2 near 1.

Hsiao and Shemdin [1983] include their relationship, Equation (2), in *Plant*'s [1982] summary plot of β/ω versus u_*/C and demonstrate that (2) models β/ω well at low values of μ_*. However, at high values of μ_*, (2) overestimates most of the measurements. This overestimate arises because Hsiao and Shemdin use the equivalent 10-m wind $\bar{U}(10)$ even for the laboratory data obtained in tanks with height of 1 m or so in which the waves corresponding to very high μ_* have wavelengths of 10 cm or less. We will demonstrate below that this and other difficulties are cleared up by a more logical choice of wind speed.

The weight of experimental evidence has shifted toward an expression of the form of (2) to describe wind forcing of water waves. This, of course, has the character of wind input due to form drag, an idea first expounded by *Jeffreys* [1924, 1925]. If the mechanism of wind input to waves is indeed analogous to form drag on a rough wall, then the appropriate reference wind is not that at the "critical height" [*Miles*, 1957] but instead at some height above the roughness elements that is related to their scale. In a recent numerical calculation, *Al-Zanaidi and Hui* [1984] obtain a result of the form of (2) but in which $\bar{U}_\lambda$ is used instead of $\bar{U}(10)$. The choice of wavelength-related height cannot be specified by rigorous argument. In this paper we have chosen one-half wavelength as the reference height, since at this height the disturbance due to a particular wavelength (observed to be exponential by *Snyder et al.* [1981]) has nearly vanished. At the same time, this height is sufficient to clear even the steepest capillaries. $\bar{U}(\lambda/2)$ is thus our reference height or "$\bar{U}_\infty$" for the waves being considered.

Scatterometry is largely concerned with the capillary-gravity transition region of the spectrum where there have been no successful measurements of surface pressure and thereby estimates of direct wind forcing. However, *Larson and Wright* [1975], in a splendid experiment, obtained the exponential growth rates of capillary-gravity waves following an abruptly turned-on wind. The growth rates have been ascribed to instability of interfacial laminar shear layers [*Valenzuela*, 1976], but for nearly all the duration of exponential growth the wave heights exceed the thickness of the laminar sublayer in the air. As was pointed out by *Valenzuela* [1976], the u_* values quoted by *Larson and Wright* [1975] are too large, since they were measured at steady state after the wave spectrum had attained its fetch limit. The exponential growth of the waves being considered (wavelengths in the range of 0.7 to 7 cm) is over in a matter of a few seconds, long before the fetch limit is reached. Thus instead of the u_* values quoted by Larson and Wright, we use the mean of their (steady state) values and the values corresponding to the initial state (i.e., smooth flow; $z_0u_*/\nu_a = 0.137$; where z_0 and ν_a are the roughness length and kinematic viscosity of the air boundary layer). The steady state values of u_* measured by Larson and Wright were 27, 66, and 124 cm s^{-1}; the values computed from the mean of the initial and final values were 24, 53, and 90 cm s^{-1}. Thus the thickness of the laminar sublayer δ $(=11.5\ \nu_a/u_*$ [*Schlichting*, 1968]) varies from 0.07 to 0.02 cm. The theoretical maximum height/wavelength ratio for gravity waves is about 1/7 [*Michell*, 1893] while that for capillary waves is almost 3/4 [*Crapper*, 1957]. However, *Schooley*'s [1958] observations of waves in the capillary-gravity region show maximum height/wavelength ratios of 0.5. If we assume that the shortest waves observed by Larson and Wright ($\lambda = 0.72$ cm) attain a limiting height of 0.36 cm while the longest ($\lambda = 6.98$ cm), which are almost gravity waves, are limited at about 1.0 cm, then for the two extreme cases of smallest wave–deepest laminar layer and largest wave–shallowest laminary layer, the wave eventually exceed the depth of the laminar layer by factors of 5.1 and 50, respectively. Therefore the wave crests would be above the laminar layer, while the observed backscattered power (proportional to height squared [*Wright* 1966]) increased by 1.4 and 3.4 orders of magnitude, respectively. Larson and Wright noted exponential growth in backscattered power over 2 to 5 orders of magnitude. It would seem then that the exponential growth observed by Larson and Wright was associated more with the characteristics of rough flow in the turbulent boundary layer than with the laminar instability of the sheared viscous sublayer. In the following we examine their data from this point of view.

In order to obtain $\bar{U}(\lambda/2)$, we need both u_* and $\bar{U}(z)$ at any height in the logarithmic boundary layer. The exponential growth estimates were obtained at three fetches (1.0, 3.0, and 8.4 m), with most of the data gathered at the intermediate fetch. Therefore we use the profiles supplied by *Larson and Wright* [1975] at that fetch (their Figure 11(*b*)). From this we obtain $\bar{U}(z)$ values of 4.9, 9.7, and 14.5 m s^{-1} at heights of 10.0, 11.5, and 13.4 cm. In Figure 1 we compare the exponential growth rates of Larson and Wright with $\mu_\lambda = (\bar{U}(\lambda/2)/C(\lambda)) - 1$. The data are tightly clustered about the straight line given by

$$\frac{\beta}{\omega}\frac{\rho_w}{\rho_a} = 0.072\ \mu_\lambda^{2.33} \qquad (4)$$

The quadratic best fit is also shown. As we remarked earlier, a quadratic relationship is associated with rough flow, and the relationship of Figure 1 is clearly, though not greatly, steeper than quadratic. It is worth noting that the roughness Reynolds numbers ($R_* = z_0u_*/\nu_a$) are, for the three u_* values given, 0.43, 2.23, and 11.3. The first of these corresponds to transitional roughness, the second is on the border between transitional and fully rough, and the third is fully rough. It could well be (indeed, it must be) that the dynamical roughness state influences the mechanism for form drag. Unfortunately, we are not aware of the results of any suitably designed experiments to clarify this point. However, for our present purposes it is enough to note that the growth rates of capillary-gravity

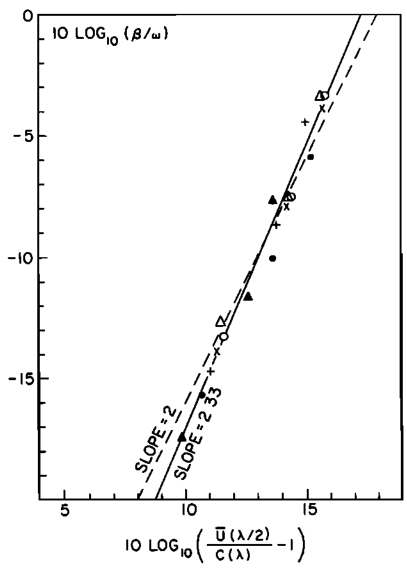

Fig. 1. Normalized exponential growth rates versus $[\bar{U}(\lambda/2)/C(\lambda)] - 1$. The data are taken from *Larson and Wright* [1975], and the different symbols refer to different wavelengths of the growing water wave: solid triangles, 0.72 cm; pluses, 1.25 cm; open triangles, 1.85 cm; open circles, 2.72 cm; crosses, 4.05 cm, and solid circles, 6.98 cm. The dashed line corresponds to (5), and the solid line corresponds to (4).

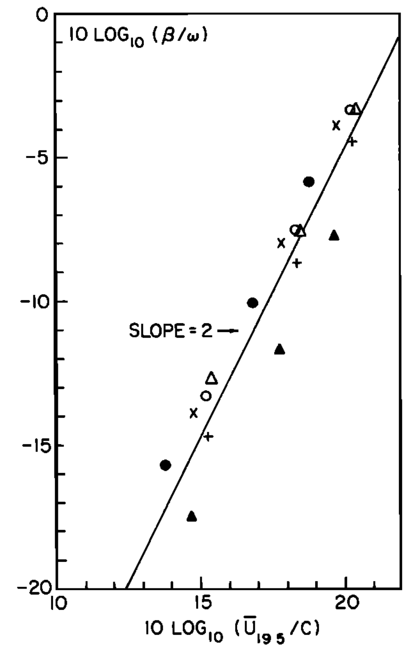

Fig. 3. Normalized exponential growth rates versus $\bar{U}(19.5)/C(\lambda)$. As in Figure 1, the data are from *Larson and Wright* [1975]. The line shown has a slope of 2.

waves are closely correlated with μ_λ, much better than with u_*/C (Figure 2) as was suggested by *Plant* [1982] or with $\bar{U}(19.5)$ (Figure 3), the usual scatterometer "predictor," which was chosen for Seasat purposes because u_* could not be measured routinely by conventional instruments.

A recent paper by *Keller et al.* [1985] provides additional evidence to support the choice of $\bar{U}(\lambda/2)$ over either $\bar{U}(19.5)$ or u_*. Keller et al. made observations of X band microwave backscatter from a tower under various wind and atmospheric stability conditions. The relative backscattering cross section depended on both wind speed (measured at 24.7 m) and atmospheric stability as illustrated in their Figure 7. When they removed the wind dependence, the relative cross section varied much more strongly with stability than with the estimated wind stress. The most unstable cases had relative cross sections 3 times larger than would be expected from the stress. For a given wind speed at 24.7 m, μ_λ is relatively large under unstable conditions, since the wind gradient is relatively weak. The effect is quite pronounced, since μ_λ is evaluated very close to the surface (for X band at a 45° incidence angle, $\lambda/2 = 1.13$ cm).

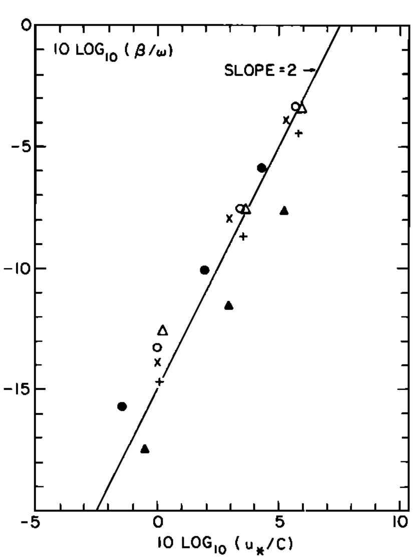

Fig. 2. Normalized exponential growth rates versus $u_*/C(\lambda)$. As in Figure 1, the data are from *Larson and Wright* [1975]. The line shown has a slope of 2.

2.2. *The Model of Wind Forcing*

In this discussion of wind forcing, we have assumed that the input to any particular wave number component of the spectrum is independent of the input elsewhere in the spectrum. The fact that these short waves, so different in wave number from the longer waves at the spectral peak, are freely propagating under natural conditions [*Donelan et al.*, 1985] tends to support this view, since phase coupling is necessary for effective wind forcing. The close agreement between the spectrally uncoupled parameter μ_λ and the observed growth rates suggests that the assumption is justified. Note that the experiments of Larson and Wright avoided the usual tank dilemma of unnaturally steep dominant waves with their attendant harmonic distortions by completing the measurements before they could develop.

In this paper we take the wind forcing for short waves to be that suggested by the quadratic fit to the data of Larson and Wright (Figure 1).

$$\frac{\beta}{\omega}\frac{\rho_w}{\rho_a} = 0.194\ \mu_\lambda{}^2 = 0.194\left(\frac{\bar{U}(\lambda/2)}{C(\lambda)} - 1\right)^2 \qquad (5)$$

Of course, this form of wind input acts only to amplify existing waves. The initiation of wavelets must be brought about by another process, perhaps an instability mechanism such as that suggested by *Valenzuela* [1976]. However, we need not be concerned here with the initiation process, since we are interested in the steady state in which appreciably steep waves are dissipating the energy supplied by the wind.

3. SPECTRAL BALANCE OF SHORT WAVES

3.1. *Wind Forcing as Growth Mechanism*

For the high–wave number part of the spectrum, sufficiently far from the spectral peak, the spectral balance may be dominated by wind input and dissipative processes, with other effects playing a lesser role. Several independent observations of radar backscatter from capillary-gravity waves provide strong evidence to support this contention as, indeed, do the optical slope measurements of *Cox* [1958]. The evidence is in the appearance at low wind speed of a "dip" in the spectrum near the wave numbers corresponding to the minimum in the dispersion relation. *Valenzuela and Laing* [1970] have shown that triad interactions may be possible and that they may cause a flux of wave energy from the slowest waves to their wave number neighbors. They claim that the dip in the spectrum is due to the energy drain from the slowest waves. Good examples of this are seen in the spectra derived from $\sigma_{VV}{}^0$ from aircraft data over the North Atlantic by *Valenzuela et al.* [1971] or *Guinard et al.* [1971] and from tank data for $\sigma_{VV}{}^0$ [*Wright and Keller*, 1971]. In both cases the dip is noticeable only at light winds. *Cox*'s [1958] optical slope measurements in a wave tank show the same effect. The obvious inference is that at all but the lowest wind speeds the nonlinear triad interactions are swamped by wind forcing and dissipation. At wind speeds above a few meters per second it appears reasonable to assume that very short gravity waves, $\lambda < 30$ cm, and capillary waves aligned with the wind receive their energy from the wind and lose it through dissipative processes.

Early work that used theories due to *Rice* [1951] on modeling backscatter [e.g., *Wright*, 1968] was based on the concept [*Phillips*, 1958] of a fully saturated spectrum in the high–wave number gravity and capillary wave region of the spectrum. That is, for the high–wave number part of the spectrum well past the spectral peak, the spectral density depends only on wave number. In models such as *Wright*'s [1968], any wind dependence of radar backscatter must arise through the effects of the tilting of the Bragg scatterers by the longer waves and not by much change in the shortwave density as a function of the wind speed as in the work of *Chia* [1968], who extended what was then believed to be known about gravity waves too far into the capillary region.

It is now generally accepted that the high–wave number part of the spectrum is not fully saturated but is dependent on wind speed [*Kitaigorodskii*, 1983; *Donelan et al.*, 1985]. The actual wind speed dependence of the short waves is not available from measurements of frequency spectra because the difficulties of transforming the frequency spectra to wave number spectra are exacerbated by the Doppler shifting due to (generally unknown) currents and the orbital velocities of longer waves. Wind speed dependent high-frequency wave spectra were described by *Pierson and Stacy* [1973] for wind-wave flume experiments, including a very sharp increase in spectral density just above a certain u_*. The dependence on viscosity, which could cause the higher frequencies, or wave numbers, to vary over a wider range was not noticed but is suggested by their Figure 5.1.

Our approach here is to propose a spectral balance between wind input and dissipation that allows the high–wave number spectrum to be wind speed dependent. Later we will insert this high–wave number spectrum in a model that includes the effects of tilting of the long waves and compare the predictions of the model with observations.

3.2. *Dissipation by Viscosity and Breaking*

The viscous dissipation of very short capillary waves has been worked out theoretically [*Lamb*, 1932] and verified experimentally by *Mitsuyasu and Honda* [1982] among others. It is a function only of wave number k and the kinematic water viscosity ν. The spectral decay rate through viscosity is $\beta_\nu = 4\nu k^2$. This term is insignificant compared with the wind forcing for gravity waves and moderate winds. However, it increases rapidly with wave number and is believed to be the reason for the sharp spectral cutoff observed by *Cox* [1958].

The spilling of the crests of large gravity waves is clearly a major sink of wave energy. It depends strongly on spectral levels, since no breaking occurs when the waves are not steep. A closer look at a wind-driven sea reveals that the short gravity waves also break in a similar way, but the result is not spectacular and, without the production of foaming whitecaps, may even go unnoticed. The rate of dissipation of this "microbreaking" is certainly dependent on spectral levels. Inasmuch as the dissipative region is locked to the wave crest and persists for a good fraction of a wave period, the energy loss is probably concentrated around the wave number of the breaking wave. Capillary-gravity waves appear to lose energy through the production of even shorter ripples at their crests, although the shortest waves are probably as much affected by the small-scale turbulence created by larger waves' breaking.

Parasitic capillary waves can form in the laboratory at the crests of nearly periodic steep gravity waves in the absence of a wind. The theory is given by *Longuet-Higgins* [1963]. *Kwoh and Lake* [1984] have measured the backscatter from these waves, specular backscatter, and the effect of sharp crests, or wedges, in the laboratory. These effects are not included in our model, although in section 10 we discuss the modifications they would produce in our results.

Although dissipation through wave breaking must depend to some extent on the spectral density elsewhere in the spectrum, in the equilibrium range the spectral levels in the vicinity of k scale with the level at k. This is particularly true for the case of full development being discussed here. (In an interesting treatment of equilibrium ranges, *Phillips* [1985] makes a similar argument.) Thus we define the normalized dissipation rate β_d/ω in terms of the local wave number and spectral density:

$$\frac{\beta_d}{\omega} = f_1[\Phi(k, \bar{\chi}), k, \gamma, g] + \frac{\beta_\nu}{\omega} \tag{6}$$

where $\Phi(k, \bar{\chi})$ is the polar wave number spectrum with $\chi = \bar{\chi}$ in the wind direction, γ is the surface tension/density ratio, and g is the gravitational acceleration. The viscosity ν is a strong function of temperature [*Weast*, 1970] and a weak function of salinity [*Sverdrup et al.*, 1942], whereas the surface tension is only weakly dependent on temperature and salinity.

Thus on dimensional grounds,

$$\frac{\beta_d}{\omega} = f_1\left(k^4\Phi(k, \bar{\chi}); \frac{\gamma k^2}{g}\right) + \frac{\beta_\nu}{\omega} \tag{7}$$

We adopt, for convenience, a power law behavior for the function f_1,

$$\frac{\beta_d}{\omega} = \alpha(k^4\Phi(k, \bar{\chi}))^n + \frac{4\nu k}{C} \qquad (8)$$

where $\alpha = f_2(\gamma k^2/g)$ and $n = f_3(\gamma k^2/g)$.

The values of α and n will depend on the nature of the breaking process. Long gravity waves lose energy largely by sudden breaking (generally "spilling" in deep water). These waves break as their height increases suddenly during their passage through a group of waves [*Donelan et al.*, 1972]. Capillary-gravity waves, on the other hand, appear to lose much of their energy to even shorter ripples formed at their crests when they steepen sufficiently. Waves in the center of the capillary-gravity range ($\gamma k^2/g = 1$) are nearly nondispersive compared with gravity waves, so that phase and group velocities are nearly equal and any increase in the height of a particular wave occurs through dynamic processes and not simply as a consequence of its passage through a group. Thus α and n may be quite different for these waves, which dissipate continuously, than for dispersive waves which grow (and break) suddenly as a kinematic consequence of their passage through a group ($\gamma k^2/g < 1$, gravity waves) or the passage of a group through them ($\gamma k^2/g > 1$, capillary waves). We assume therefore that α and n attain the asymptotic values α_1, n_1 and α_2, n_2 according to whether the waves are strongly dispersive or nearly nondispersive. For a given average energy density, the intensity of energy loss is dependent on the rate at which waves overtake groups or vice versa. We parameterize this in the following manner:

$$n = (n_1 - n_2)\left|2 - \frac{g + 3\gamma k^2}{g + \gamma k^2}\right|^b + n_2 \qquad (9)$$

$$\ln \alpha = (\ln \alpha_1 - \ln \alpha_2)\left|2 - \frac{g + 3\gamma k^2}{g + \gamma k^2}\right|^b + \ln \alpha_2 \qquad (10)$$

where n_1 and α_1 are determined from observations of gravity wave spectra and b, n_2, and α_2 are picked to yield the best fit to the observed backscatter at K_u band.

3.3. *Equilibrium Ranges*

Equating input (equation (5)) and dissipation (equation (8)), we obtain an expression for the downwind spectrum of the short waves in the "equilibrium" range, subject to the constraints that $\bar{U}(\lambda/2) > C(\lambda)$ and that [ ] > 0 (otherwise, the spectrum is 0):

$$\Phi(k, \bar{\chi}) = k^{-4}\left[\frac{0.194}{\alpha}\frac{\rho_a}{\rho_w}\left(\frac{\bar{U}(\lambda/2)}{C(\lambda)} - 1\right)^2 - \frac{4\nu k}{\alpha C(\lambda)}\right]^{1/n} \qquad (11a)$$

Or, in terms of wave number only,

$$\Phi(k, \bar{\chi}) = k^{-4}\left[\frac{0.194}{\alpha}\frac{\rho_a}{\rho_w}\left(\frac{\bar{U}(\pi/k)}{C(k)} - 1\right)^2 - \frac{4\nu k}{\alpha C(k)}\right]^{1/n} \qquad (11b)$$

Here "equilibrium" is used formally to mean where wind input and dissipation are locally (with respect to wave number) balanced.

Equations (11*a*) and (11*b*) represent a one-dimensional slice through the wave number spectrum in polar form for waves traveling downwind in the direction $\bar{\chi}$. The balance of wind input and dissipation in the wind direction gives (11) and describes the downwind spectral values. For waves traveling at off-wind angles to the wind direction $\bar{\chi}$ the wind input term is often given as

$$\Phi(k, \chi) = k^{-4}\left[\frac{0.194}{\alpha}\frac{\rho_a}{\rho_w}\left(\frac{\bar{U}\cos(\chi - \bar{\chi})}{C} - 1\right)^2 - \frac{4\nu k}{\alpha C}\right]^{1/n} \qquad (11c)$$

However, at large angles to the wind the wind input decreases rapidly, and a simple balance between wind input and dissipation according to (11*c*) is not observed in the field. Normal to the wind direction, wind input in terms of a constant mean wind vanishes, but observations reveal significant energy density of the short waves. The natural variability of the wind direction spreads the angular range of wind input beyond that which would occur in a laboratory tank with a well-defined wind direction. Nonlinear interactions among waves may also act to spread the energy beyond $\pm\pi/2$. To account for this, though not to explain it, we have assumed, as was observed by *Donelan et al.* [1985], that the spectrum of the short waves spreads according to (12), which allows the choice of h_1 to fit the cross-wind backscatter measurements.

The value of h_1 was chosen so that (12) and (11*c*) agree at $\Phi(k, \chi) = 0.8\ \Phi(k, \bar{\chi})$. Once h_1 has been chosen, the complete azimuthal and wave number behavior of the spectrum is described by (12), where the downwind value, $\Phi(k, \bar{\chi})$, is given by (11*b*). The decision to base the choice of h_1 on the 80% height of the spectrum was determined by comparison with the cross-wind circle flight data. Unlike the energy-containing part of the spectrum near the peak, the spreading of these short waves is determined by their wave number and by the wind speed to phase speed ratio for that component. Generally speaking, the values of h_1 decrease as the wind speed increases, causing energy at a particular wave number to scatter over larger angles about the wind direction.

$$\Phi(k, \chi) = \Phi(k, \bar{\chi})\ \mathrm{sech}^2\ [h_1(\chi - \bar{\chi})] \qquad (12)$$

The differential element in (12) is $dk\ k\ d\chi$, and integration over $k > k_1$ and χ then yields the variance of the spectrum for $k > k_1$. The wave number spectrum is not zero at $\chi - \bar{\chi}$ equal to $\pm\pi/2$.

3.4. *Threshold Wind Speeds*

As $\bar{U}(\pi/k)$ is gradually increased for a fixed k as, say, the wind at 10 m increases from calm, the quantity in square brackets in (11*b*) will at first be zero because the wind will not be able to overcome the effect of viscosity and generate Bragg waves at that wave number by the mechanisms of the model until a threshold speed is reached. This threshold speed is given by (13), as found by setting the quantity in square brackets to zero and solving for $\bar{U}(\pi/k)$, where $D = 0.194\ \rho_a/\rho_w$:

$$\bar{U}(\pi/k) = C(k) + 2[\nu k C(k)/D]^{1/2} \qquad (13)$$

For a 2-cm spectral wave number component, $\bar{U}(\pi/k)$ is needed at a height of 1 cm. The left-hand side is solely a function of the wind profile. The right-hand side is solely a function of the waves on the water, the surface tension, gravity, and the viscosity of the water. Thus for light winds, (13) couples the waves to the winds.

To define the mean wind above the wavy surface as a function of height in terms of, say, the wind at 10 m, either $z_0 = z_0(u_*)$ or $C_{DN} = C_{DN}(\bar{U}(10))$ must be specified. We specify the mean wind profile for neutral stability in the following terms:

$$C_{DN} = A + B\bar{U}(10)$$
$$= 10^{-3}[0.96 + 0.041\bar{U}(10)] \qquad (14)$$

This form for the drag coefficient is from *Donelan* [1982] and is based on selecting only those data from *Garratt's* [1977] summary based on direct Reynolds stress measurements. The data are from many researchers and cover a range of 4 to 16 m s^{-1}. Equation (14) also fits the data of *Large and Pond* [1981] within experimental scatter for higher winds. It is generally accepted that the drag coefficient increases with wind speed. Equation (14) applies for fully developed seas and those near full development.

From the definition of the wind profile for neutral stability, the wind at π/k is given in terms of $\bar{U}(10)$ as

$$\bar{U}(\pi/k) = \bar{U}(10)\left[1 + \frac{[A + B\bar{U}(10)]^{1/2}}{\kappa}\left(\ln\left(\frac{\pi}{10}\right) - \ln k\right)\right] \qquad (15)$$

Both measurements in wind wave flumes and at sea as in the work of *Mitsuyasu and Honda* [1982] and *Badgley et al.* [1968] demonstrate that the wind profile under neutral stability conditions is logarithmic down to fixed heights near the crest of the largest waves. Both theory [*Benjamin*, 1959] and experiment [*Hsu et al.*, 1981] indicate that the mean wind measured at a constant height relative to the moving surface is nearly logarithmic above the viscous boundary layer. The winds at the reference height of $\lambda/2$, or π/k, are well above the viscous boundary layer.

It is necessary to parameterize the value of $\bar{U}(\pi/k)$ in terms of a more easily measurable quantity such as either $\bar{U}(10)$ or $\bar{U}(19.5)$ in the same sense as the wind stress at the sea surface is parameterized in terms of these quantities. The wind stress at the sea surface is also not a directly measurable quantity. It must be found by measuring the downward flux of turbulent momentum at a convenient height above the waves.

At these heights (a half wavelength of capillary-gravity waves), the effect of atmospheric stability on the wind profile is negligible and the profile above the viscous boundary layer is always nearly logarithmic. The use of the effective neutral wind in attempts to recover winds from the Seasat SASS was consequently a correct procedure. Variations in the mesoscale turbulent fluctuations in the wind as a result of stability might have a higher-order effect.

The right-hand side of (13) is a function of wave number, surface tension, and the viscosity of water. The molecular viscosity of fresh water, free of dissolved gases, in centipoise (1 cP = 1 g cm^{-1} s^{-1}) varies from 1.787 at 0°C to 0.7975 at 30°C according to work of Hardy and Cottington at the National Bureau of Standards in the late 1940s and unpublished work of F. Swindells as shown in some issues of *The Handbook of Chemistry and Physics* [*Weast*, 1970]. The molecular viscosities of seawater at 0°C and salinities of 30‰ and 35‰ are 1.88 and 1.89, respectively, according to *Dorsey* [1940] as given by *Sverdrup et al.* [1942]. At 30°C and 30‰ and 35‰, they are 0.86 and 0.87 cP, respectively. The conversion to kinematic viscosity in centistokes (1 cSt = 1 cm^2 s^{-1}) for fresh water produces a slightly larger numerical value for higher temperatures. The compensating effect of density for seawater converts the above numerical values for 30‰ and 35‰ in centipoise to about 1.836, 1.838, 0.844, and 0.855 cSt.

The use of a kinematic viscosity for fresh water based on a density equal to 1 instead of a kinematic viscosity for seawater would shift some of the calculations to follow by at most 1.4 to 3.5% or 0.06 to 0.15 dB. This corresponds to 2 to 5 cm s^{-1} out of 2 to 6 m s^{-1} at light winds for K_u band as shown in Figure 4. The additional refinement is not necessary for the present analysis.

The left-hand side of (13) can be evaluated as a function of k for fixed values of $\bar{U}(10)$. For light winds and for all values of k, $\bar{U}(\pi/k)$ increases with increasing $\bar{U}(10)$. For fixed $\bar{U}(10)$, $\bar{U}(\pi/k)$ decreases with increasing k. For higher winds, additional effects occur that will be discussed later.

For a nominal value of surface tension, the right-hand side of (13) can be evaluated as a function of k for different kinematic viscosities, which in turn are a function of salinity and water temperature. Unless the left-hand side of (13) is greater than the right-hand side of (13), there will be no Bragg-scattering waves at that wave number according to the mechanisms of the model. Figure 4 shows the graphs of these two functions as a function of both k and λ. The left-hand side of (13) is graphed as a function of k for values of $\bar{U}(10)$ from 1 to 20 m s^{-1}. The right-hand side of (13) is graphed as a function of k for viscosities corresponding to a salinity of 35‰ and 0°C, 10°C, 20°C and 30°C. The four solid curves for the threshold speed are for salinities of 35‰. The entire effect of changes in salinity is shown by two dashed lines just below those for 0°C and 30°C and 35‰. These are for fresh water, and the change is only a decrease of a few centimeters per second at K_a band and even less at K_u band and X band. An average salinity for oceanic conditions will be adequate for future applications.

Also shown in Figure 4 are vertical bars and triangles corresponding to the Bragg-scattering wave numbers at incidence angles of 20°, 30°, 40°, 50°, 60° and 65° calculated according to (16), where k_0 is the radar wave number for X band, K_u band, and K_a band. The abscissa values are labeled according to incidence angle.

$$k = 2k_0 \sin\theta \qquad (16)$$

Bragg scattering is inadequate if the effects of the slopes of the longer waves are omitted. At light winds the effect of the slopes of the longer waves is less important, and so (13) and Figure 4 provide useful estimates of the threshold speeds. For K_a band, Figure 4 has to be interpreted with considerable caution. For X and K_u band, (13) predicts important results for light winds.

At X band for 30°C water and 20° incidence angle, Bragg waves will be maintained by the mechanism under analysis when the wind exceeds 2 m s^{-1}. At 65° it must exceed 3 m s^{-1}. Over 0°C water, for the corresponding angles the values are 2.8 and 4.5 m s^{-1}.

At K_u band for 0°C water, the needed wind speed is 3.1 m s^{-1} at 20° incidence angle and 6.3 m s^{-1} at 65°. For 30°C water, the values are 2.2 and 4.2 m s^{-1}. These results have an important effect on the interpretation of the backscatter values obtained by the Seasat SASS that will be described later.

Considerably higher winds are needed to maintain those wave numbers needed for first-order Bragg theory for K_a band. The situation becomes more complicated because the slopes of the longer waves will cause backscatter from lower wave numbers. Also, the wind at π/k or $\lambda/2$ does not continue to increase at the higher wave numbers, as the wind at 10 m increases as is shown by the values for 20 and 15 m s^{-1}. Figure 4 at least suggests that backscatter at K_a band will be

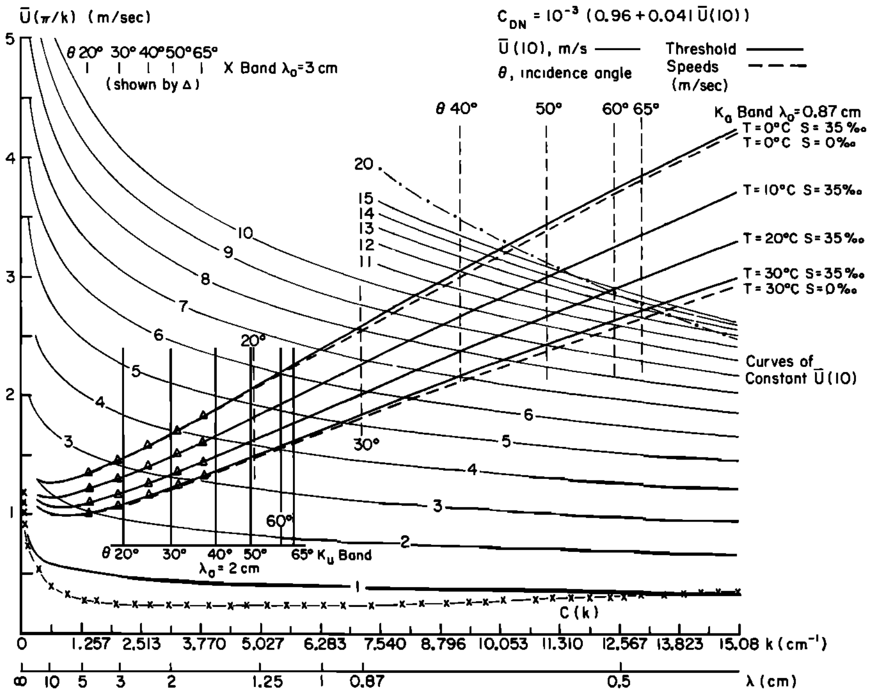

Fig. 4. Threshold wind speeds for significant Bragg backscatter for X, K_u, and K_a band. The abscissa is wave number per centimeter, or wavelength in centimeters. The ordinate is wind speed at π/k, or $\lambda/2$, with lines of constant wind speed at 10 m as a parameter. The threshold speeds are shown for four temperatures for salinities of 0‰ and 35‰. Conditions for incidence angles from 20° to 65° are shown. Unless the curve for constant $\bar{U}(10)$ lies above the threshold speed, Bragg backscatter will probably be too low to detect. The phase speed is shown by the curve labeled $C(k)$.

quite different from backscatter at K_u and X band and that there will be difficulties in interpreting such measurements for both light winds and high winds.

If it were possible to measure the Bragg wave number spectrum, it would be found to grow toward increasing wave number as the wind speed increases. At K_u band, for example, the wind must increase from 2.1 m s^{-1} to 4.2 m s^{-1} for 30°C water before the spectrum will be in equilibrium for waves that produce backscatter at all incidence angles from 20° to 65°.

The effect of the phase speed of the waves, which is the first term on the right-hand side of (13), is shown in Figure 4 as a coded curve. The wind at π/k must first exceed $C(k)$ for the squared term in (11*b*) to be meaningful for wave generation. The effect of viscosity is 3 to 5 times more important than the phase speed in determining the threshold wind that will maintain the spectrum of the model for K_u band, for example.

Figure 5 shows the lower range of wave numbers applicable to L band and C band radars. It predicts that the first waves to be amplified and to reach an equilibrium state by this mechanism by a very light wind are essentially gravity waves with wave numbers centered on L band. The recent work of *Kahma and Donelan* [1987] indicates that the inception wind speed for microscopic capillary-gravity waves is only 0.7 m s^{-1}. The first waves to grow have wavelengths of 5–10 cm. Given enough fetch, these waves can grow to the point where their amplitudes exceed the depth of the viscous sublayer (~0.3 cm). At this point they are still hardly noticeable by eye or radar, and the efficacy of the laminar shear flow instability may be drastically reduced.

Somewhat higher winds and the growth mechanism discussed in section 2 may be necessary to bring the wave heights up to the point where the surface is considered to be ruffled. Figure 5 shows that once excited, the gravity waves at L band can be sustained by this mechanism by lighter winds than either longer gravity waves or shorter capillary-gravity and capillary waves.

Since natural winds may be at times very variable when light, especially when convective activity is present (longitudinal turbulence intensities of about 50%), the growth of small waves on large water bodies might be expected to follow a visual pattern like this. As the mean wind slowly increases from zero, scattered patches of short (~7-cm wavelength) gravity waves appear and disappear. Eventually, either through nonlinear interactions of these short waves or by direct resonance with pressure patterns in the wind [*Phillips*, 1957], longer gravity waves begin to appear and, given enough fetch, grow to dominate the spectrum. If the wind then drops just below about 2 m s^{-1} (at 10°C), the ruffles disappear quickly and the surface is left disturbed by gravity waves of about 25-cm wavelength (L band).

Visual observations and photographic records from Lake Ontario (maximum fetch, 300 km) generally confirm this pattern. Thus as the wind drops, the L band waves may be the last to succumb to the ravages of viscosity. In any case, detection of light winds by scatterometry will fail below about 1.9 ± 0.3 m s^{-1} depending on water temperature. Photographs by *Kinsman* [1965] such as the one on the upper left facing page 491 and the one on the top facing page 543, which also has longer swells, show these longer gravity waves with no apparent capillary-gravity waves superimposed on them.

Turbulence levels for winds over the ocean can vary over a considerable range for light winds. For light winds in subsiding air near the subtropical highs, the boundary layer near the sea surface may have low turbulence levels. Whether or not L band waves would then be the only substantial contribution

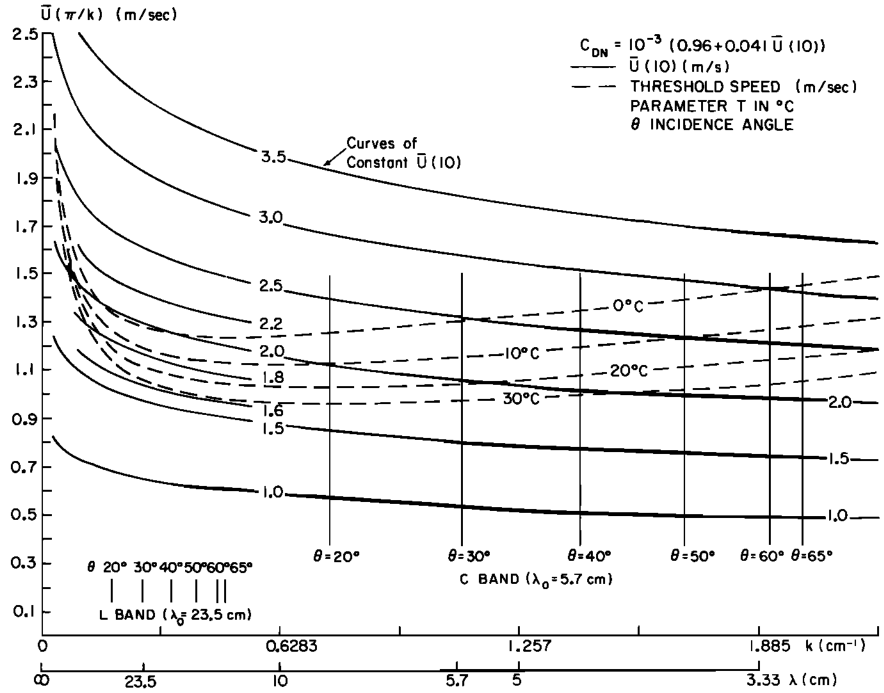

Fig. 5. Threshold wind speeds for significant Bragg backscatter for L and C band. The abscissa is wave number per centimeter, or wavelength in centimeters. The ordinate is wind speed at π/k, or $\lambda/2$, with lines of constant wind speed at 10 m as a parameter. The threshold speeds are shown for four temperatures for salinities of 0‰. Conditions for incidence angles from 20° to 65° are shown. Unless the curve for constant $\bar{U}(10)$ lies above the threshold speed, Bragg backscatter will probably be too low to detect.

to the steady state spectrum of our model would need to be determined for oceanic conditions where the level of turbulence is small.

For a further analysis of the basic equation for the Bragg spectrum at upwind (equation (11*b*)), we consider the amount by which the wind at π/k exceeds the threshold wind defined by (13). Let a speed be defined by

$$C_v = C_v(T, S, k) = (v(T, S)kC(k)/D)^{1/2} \tag{17}$$

Then the wind at π/k must exceed the threshold wind by an amount $\Delta\bar{U}(\pi/k)$ for Bragg waves to be maintained.

$$\Delta\bar{U}(\pi/k) = \bar{U}(\pi/k) - C(k) - 2C_v(T, S, k) \tag{18}$$

The spectrum at upwind can then be given by

$$\Phi(k, \bar{\chi}) = \left(\frac{D}{\alpha}\right)^{1/n} \frac{k^{-4}}{(C(k))^{2/n}} |\Delta\bar{U}(\pi/k)(\Delta\bar{U}(\pi/k) + 4C_v(T, S, k))|^{1/n} \tag{19}$$

For $\Delta\bar{U}(\pi/k)$ small compared with $4C_v$, the spectrum grows as $(\Delta\bar{U}(\pi/k))^{1/n}$. For $\Delta\bar{U}(\pi/k)$ large compared with $4C_v$, it grows as $(\Delta\bar{U}(\pi/k))^{2/n}$. The actual values fall in between. For first-order Bragg scattering, quite clearly backscatter cannot follow a power law as a function of $\bar{U}(\pi/k)$. Moreover, even for higher winds with a two-scale model it would be expected that the effect of viscosity would result in different values for the backscatter for the same wind.

4. EXPERIMENTAL VERIFICATION OF FEATURES OF THE HIGH-WAVE NUMBER SPECTRUM

In a recent study, *Kahma and Donelan* [1987] examined the formation of initial waves for light winds. In particular, their results demonstrate the sensitivity of the inception wind speed (speed at which waves first form) to water temperature and show that the changes in growth rates for various water temperatures are commensurate with the predicted changes due to viscous damping. The initial generation of wavelets appears to be through the mechanism of laminar shear flow instability of the coupled air-water interfaces [*Valenzuela*, 1976; *Kawai*, 1979] or by resonance with intrinsic pressure perturbations in the air [*Phillips*, 1957]. However, it is unlikely that these growth mechanisms will be effective in amplifying the waves to the point where they are observable by scatterometers, for they will then be much higher than the depth of the laminar shear layers, and further exponential growth will be the result of the fully rough flow of our model. It is likely that exponential growth by direct wind input as described by (5) will be required to take the wavelets from their initial stages to the point where they would be observable by scatterometers and are steep enough to be restrained by wave breaking as well as viscous damping as in (8). The wave spectrum undergoes a large increase in spectral density of about 3 decades before the "soft saturation" occasioned by sporadic breaking reduces the dependence of the spectral density on wind speed. This equilibrium range resulting from a balance between (5) and (8) is still clearly wind speed dependent, and for capillary-gravity waves in the absence of long waves, the dependence is as would be predicted by our model for fully rough flow.

5. A COMPOSITE DIVIDED SCALE MODEL

5.1. *Properties of Composite Models*

When a broad spectrum of waves exists, the modulation of the Bragg-scattering waves by the longer waves will alter the observed backscattered power. Thus in order to interpret observed backscatter over a wind-generated sea, the spectrum (equation (12)) by itself is not sufficient. We must construct a model that includes the effects of the rest of the spectrum on the resonant Bragg waves insofar as these longer waves tilt the Bragg scatterers and produce variations in their heights over different phases of the longer waves. Such models have been called composite models.

Valenzuela [1978] has reviewed composite models in which the wave spectrum is divided into short Bragg-scattering waves and longer waves whose principal function is to tilt the surface. In these models, one is interested in the wave number spectrum of the short waves and the probability distribution of slopes of the longer waves. Simple two-scale models like this require a more or less arbitrary decision regarding the separation of scales and generally assume that the waves of one scale are completely uncoupled from those of the other.

In this paper we draw on previous work on the slopes and energy distribution of gravity waves to construct a realistic two-scale model. The parameters of the longer-scale gravity waves (the "tilting waves," for short) can be tied down by observational results. By contrast, the only direct information available in the capillary-gravity range comes from Bragg-scattering measurements, which at steady state are necessarily made in the presence of tilting waves. The effects of the tilting waves are sufficiently large that such observational results can be used to infer the wave number spectrum of the Bragg waves only through a model that includes the effects of the tilting of the Bragg waves. Composite divided scale models provide the simplest approach to account for such effects. The unknown parameters of the shortwave spectrum may therefore be inferred by adjusting them to yield good agreement between the model and observations of radar backscattering cross section. In this model two of the parameters are n and α as discussed previously. These are the Bragg wave parameters. Two other relatively minor parameters ε and Γ are discussed below. These latter parameters pertain to the tilting waves. The angular spread of the Bragg waves, h_1, was determined as was described in section 3.3 for (12) so as to produce the measured aspect angle backscatter dependence.

5.2. *Slopes of the Low–Wave Number Waves*

The observations of *Cox and Munk* [1954], derived from sun glitter, are among the more reliable observations of the slopes of natural wind waves. They found, in the range of wind speeds of 0.5 to 14 m s^{-1} and for a long fetch, that (1) the probability distribution of slopes is nearly Gaussian with, however, some skewness such that larger negative slopes occur than positive, with the X axis aligned with the wave propagation direction; (2) the variance of upwind/downwind slopes exceeds the variance of cross-wind slopes by a factor between 1 and 2; (3) the upwind/downwind skewness increases with wind speed; (4) the kurtosis of the distribution of slopes is larger than Gaussian but only by an amount slightly larger than the estimated observational error; and (5) the addition of an extensive oil slick to the surface reduces the variance of slopes by a factor of 2 or 3, eliminates the skewness, and leaves the kurtosis unchanged. The oil slick appeared to remove virtually all waves shorter than 30 cm. Since the pioneering work of Cox and Munk, several laboratory studies [e.g., *Cox*, 1958; *Keller and Wright*, 1975; *Reece*, 1978] have shown that the energy density of the ripples is related to the phase of the long waves. *Longuet-Higgins* [1983] has given theoretical arguments to show why this occurs and further pointed out that this is sufficient to explain the observed skewness of slopes, whereas harmonic distortion of the long waves is not. The addition of an oil slick attenuates the ripples and with them the skewness. In the context of our model we require a description of the modulation (in both amplitude and phase) of the energy density of the Bragg waves (ripples) by the longer tilting waves.

5.3. *Variation of the High–Wave Number Spectrum on the Long-Wave Surface*

Cox [1958] showed that ripples were concentrated on the forward faces of the large waves but was not able to be more specific about the phase or amplitude of the modulation of the ripples with respect to the long waves. He also showed that the variance of slopes increased with wind speed. The tank photographs of *Mitsuyasu and Honda* [1975, Figure 18] provide excellent documentation of the occurrence of ripples on the forward faces of the longer waves. This is also evident in photographs (Figure 6) of the sea surface. *Reece* [1978] set about to explore the modulation in detail but could only conclude that the distribution of energy density of the ripples is modulated by up to 100% (peak-to-peak) of the mean and the phase is advanced 45° to 180° with respect to the long waves. The modulation increases with wind speed. The results of *Keller and Wright* [1975] are in general agreement with this. The simplest modulation model which has these general features is one in which the modulation is proportional to upwind/downwind slope and is limited in the manner described by Reece as follows:

$$
\begin{aligned}
\Phi(k, z_x) &= (1 - \varepsilon z_x)\Phi(k) & |\varepsilon z_x| &\le \tfrac{1}{2} \\
\Phi(k, z_x) &= (1 - 0.5 \operatorname{sgn}(\varepsilon z_x))\Phi(k) & |\varepsilon z_x| &> \tfrac{1}{2}
\end{aligned}
\tag{20}
$$

where k is the wave number of the Bragg waves, z_x is the downwind slope of the tilting waves, and ε is a constant to be determined empirically. The principal effect of this modulation will be to produce a difference in scattering cross section looking upwind versus downwind. The difference arises because looking upwind, the enhanced waves are seen at an angle tilted toward the radar look direction (i.e., lower wave number

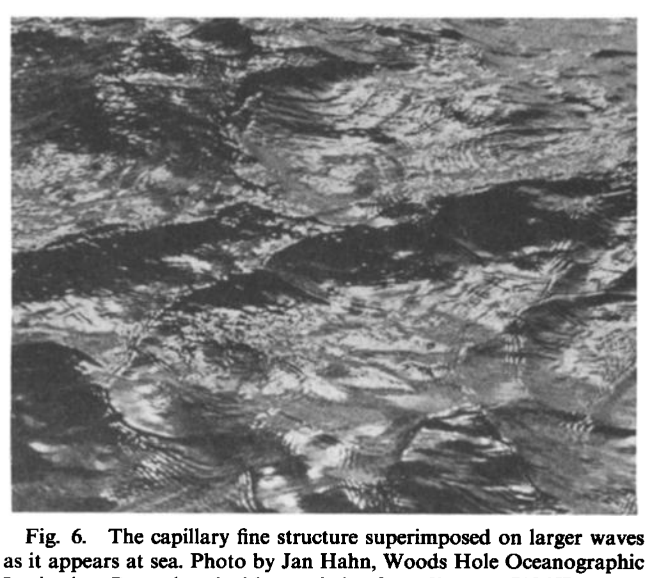

Fig. 6. The capillary fine structure superimposed on larger waves as it appears at sea. Photo by Jan Hahn, Woods Hole Oceanographic Institution. Reproduced with permission from *Kinsman* [1965].

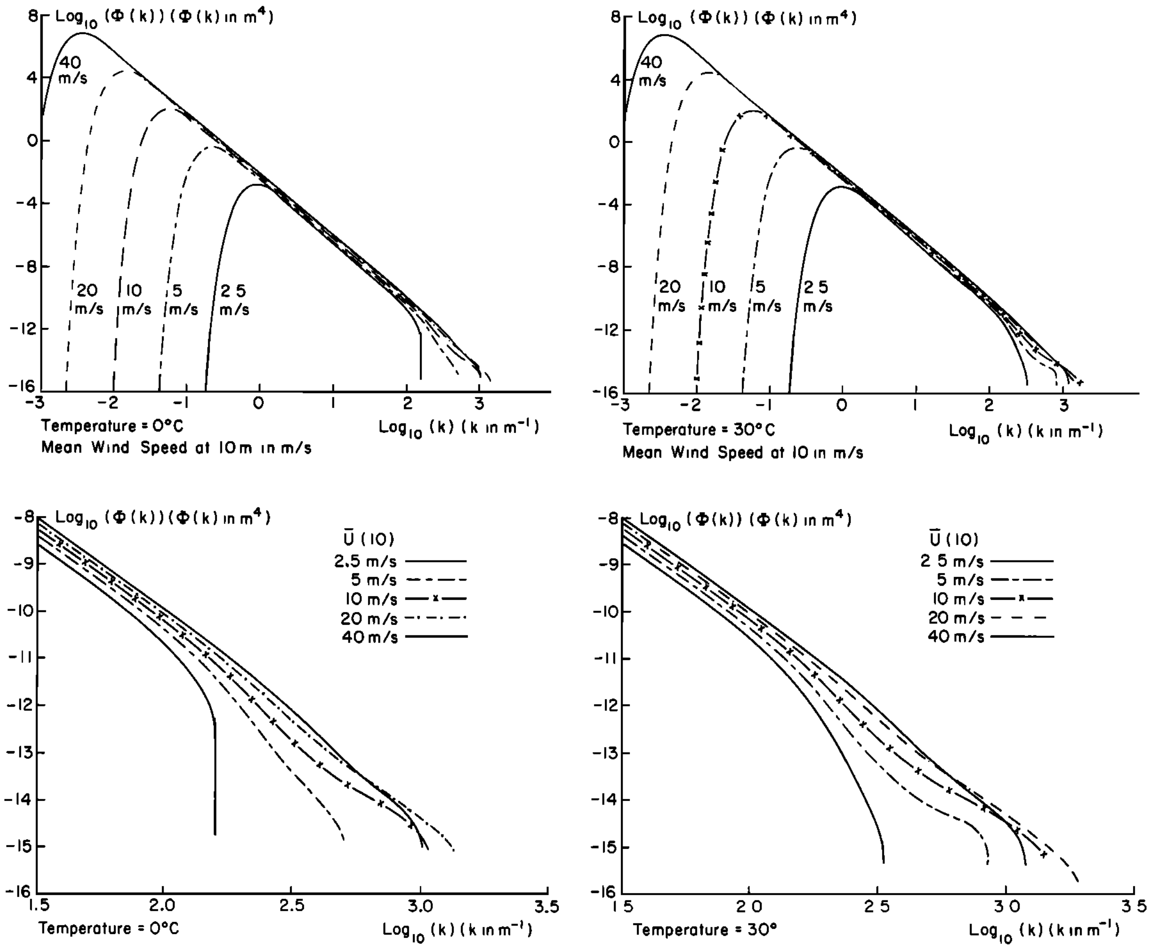

Fig. 7. Sections through the wave number spectrum, $\Phi(k)$ in m^4 versus k per meter at upwind for mean wind speeds at 10 m of 2.5, 5, 10, 20, and 40 m s^{-1}. (top left) Full spectrum for 0°C water temperature. (top right) Full spectrum for 30°C water temperature. (bottom left) Details of spectrum of 0°C for $\log_{10} k$ greater than 1.5. (bottom right) Details of spectrum for 30°C for $\log_{10} k$ greater than 1.5.

and hence higher energy density), while the opposite is true looking downwind. The constant ε was set to 1 by comparing the model output with observed upwind/downwind differences in scattering cross section.

Cox and Munk [1954] have shown that the variance of slopes increases uniformly with wind speed and that much of the variance is due to waves with lengths of less than 30 cm. For our purposes we need a spectral description of slopes over the entire wave number range from the peak of the spectrum out to the wave numbers of the Bragg scatterers. No such observations have yet been published, although a wealth of information exists concerning the energy spectrum (with frequency of encounter) of gravity waves. It is now generally accepted that the equilibrium range of the spectrum, at least near the peak ($1.5\omega_p$ to $3.5\omega_p$), varies as ω^{-4} [*Toba*, 1973; *Forristall*, 1981; *Kahma*, 1981; *Donelan et al.*, 1985]. At higher frequencies (relative to the peak), observations of frequency spectra are not useful indications of the underlying wave number spectra, since frequencies of encounter are a complex mix of intrinsic wave frequencies and Doppler shifts occasioned by wind drift and orbital velocities of longer waves. However, it is clear that a $k^{-3.5}$ (corresponding to ω^{-4}) dependence cannot extend to arbitrarily large k, since the maximum wave steepness is limited. *Kahma* [1981] and *Leykin and Rozenberg* [1984] have provided some evidence for steepening of the spectrum beyond an ω^{-4} range near the spectral peak, and *Kitaigorodskii* [1983] argues theoretically for an eventual transition to ω^{-5} or k^{-4}.

5.4. *The Full Wave Number Spectrum*

To construct the full wave number spectrum, we use the directional spectra observations of *Donelan et al.* [1985] in the wave number range from 0 to $10k_p$ patched to (11) from $10k_p$ to ∞. *Leykin and Rozenberg* [1984] also argue that the spectral slope transition from ω^{-4} to ω^{-5} occurs at about $3.2\omega_p$, which corresponds to $10k_p$. The larger the value of n_1 in (9), the closer the spectrum will be to k^{-4} (or ω^{-5}), but the results are not sensitive to the choice of n_1 for n_1 greater than about 5. Consequently, we take $n_1 = 5$. Matching the observed spectra to (11) at $10k_p$ requires that $\ln \alpha_1 = 22$. Comparison with the circle flight data (see below) yields $n_2 = 1.15$ $\ln \alpha_2 = 4.6$ and $b = 3$.

The low-wave number part of the spectrum is from *Donelan et al.* [1985] for a fully developed wind-generated sea and for $0 < k < 10k_p$. It is defined by (21), where the wind is the effective neutral wind at 10 m,

$$\Phi(k, \chi) = \frac{1.62 \times 10^{-3}\bar{U}(10)}{k^{3.5}g^{0.5}} \exp\left(-\frac{g^2}{k^2(1.2\bar{U}(10))^4}\right) \cdot 1.7^{F(\bar{U}(10),k)} h(k/k_p) \operatorname{sech}^2 [h(k/k_p)(\chi - \bar{\chi})] \qquad (21a)$$

where

$$F(\bar{U}(10), k) = \exp\left[-1.22\left(\frac{1.2\bar{U}(10)k^{0.5}}{g^{0.5}} - 1\right)^2\right] \qquad (21b)$$

The peak of the spectrum is given by

$$k_p = g/(1.2\bar{U}(10))^2 \qquad (22)$$

In (21), h is defined as an essentially continuous function of k/k_p over several ranges of k/k_p as follows:

$$h = 1.24 \qquad 0 < k/k_p < 0.31$$

$$h = 2.61(k/k_p)^{0.65} \qquad 0.31 < k/k_p < 0.90$$

$$h = 2.28(k_p/k)^{0.65} \qquad 0.90 < k/k_p < 10$$

The composite wave number spectra patch (21) for low wave numbers to (12) for high wave numbers. The composite spectra for $\chi = \bar{\chi}$ are shown in Figure 7 for various wind speeds and extreme values of water temperature of 0°C and 30°C. For the upper full spectra, there are five spectra as the wind speed, starting at 2.5 m s^{-1}, is doubled for each successive spectrum. The areas under the gravity wave part of the spectra essentially vary as $(\bar{U}(10))^4$, and the spectral slopes at high wave numbers vary with a power of between -3.5 and -4.

For the high wave numbers, those parts of the spectra above 31.62 m^{-1} ($\log_{10} k = 1.5$) are graphed below the full spectra for the same wind speeds and temperatures. Each curve stops abruptly at a wave number which is that wave number for which the spectra defined by (11*b*) cease to exist according to the model and in accordance with Figures 4 and 5. Bragg-scattering wave numbers exist for some radar wavelengths and incidence angles over warm water, whereas they are not present over cold water. The spectra expand toward higher wave numbers with increasing wind speed for winds up to 20 m s^{-1}.

The two spectra for a wind of 40 m s^{-1} lie below portions of the spectra for 10 m s^{-1} and 20 m s^{-1}. From (15), as the wind at 10 m increases, the wind at π/k at first also increases, but eventually the increasing wind gradient (equation 14)) causes $\bar{U}(\pi/k)$ to decrease with increasing wind speed at 10 m. Increasing slopes for the gravity wave part of the spectrum overcome this effect for some high winds, but eventually, for high enough winds the Bragg backscatter will decrease. The wind shear just above the viscous boundary layer increases so that although the wind at 10 m increases, the wind at π/k decreases.

It is, fortunately, not to be expected that fully developed spectra such as those for a 40 m s^{-1} wind will ever be estimated from wave data where the winds are 40 m s^{-1} at 10 m. The significant wave height would be about 45 to 50 m, whereas the highest single waves ever measured have not exceeded these heights. The required fetch and duration would never be large enough.

5.5. *Slopes of the Tilting Waves*

These spectra may be used to compute the overall upwind and cross-wind slopes for comparison with the observations of *Cox and Munk* [1954]. This yields an approximately linear wind speed dependence over the full wave number range of the composite spectra, as observed by Cox and Munk, and values of mean square slope that are 70% higher than theirs. The method of Cox and Munk does lose extreme slope values, thereby tending to underestimate the total variance of slope, but it is unlikely that a factor of 1.7 can be accounted for in this way. At present, we are unable to resolve this difference, and for internal consistency, we will use the values derived from our composite spectra. It is noted that Cox and Munk's table that provides wave heights versus wind speed does not show a uniform increase of wave height with wind speed and does not correspond to values for fully developed wind waves. Consequently, their slope versus wind speed values may be underestimates of those for full development. The mean square slopes of waves in the gravity region, which are the tilting waves, are given by (23) and (24) where k_p is the wave number of the spectral peak. The slope variance increases as k_Γ increases for a given wind speed, since more of the wave number spectrum is involved ($k_\Gamma(=k/\Gamma)$ is the high–wave number cutoff of the tilting waves).

$$S_u^2 = 8.7 \times 10^{-3}\Omega^{1/2} \qquad 0 \le \Omega < 1 \qquad (23a)$$

$$S_u^2 = [3.0(\log_{10} \bar{U}(10))^{1/2} + 1.37] \times 10^{-3}(\Omega - 1) + 8.7 \times 10^{-3} \qquad 1 \le \Omega < 10 \qquad (23b)$$

$$S_c^2 = 4.6 \times 10^{-3}\Omega \qquad 0 \le \Omega < 1 \qquad (24a)$$

$$S_c^2 = [3.3(\log_{10} \bar{U}(10))^{1/2} + 0.82] \times 10^{-3}(\Omega - 1) + 4.6 \times 10^{-3} \qquad 1 \le \Omega < 10 \qquad (24b)$$

In (23) and (24), S_u^2 and S_c^2 are the slope variances, $\Omega = [\log_{10}(k_\Gamma/k_p)]^2$, $\bar{U}(10)$ is in meters per second and is greater than or equal to 1.0.

If k_T is less than or equal to k_p, S_u^2 and S_c^2 are set to 10^{-7}, i.e., essentially zero. These slope variances have been computed by integrating the slope spectra for values of k up to $k = 2\pi/30$ (cm^{-1}).

5.6. *Two-Scale Backscatter Model Structure*

In the preceding sections, we have defined wave number spectra over two ranges of wave number space. The spectral balance, equation (11), is such that for each wave number there is a particular (water viscosity dependent) wind speed at which the spectrum vanishes. Of course, in any natural wind if the average wind is such that (11) vanishes, it may not during gusts. This is commonly observed at light winds in the appearance of patches of "cat's paws." To account for this in the model, we allow the wind speed to have a Gaussian distribution about its mean with a standard deviation proportional to the mean as observed by *Smith* [1974]. The average value of Smith's observations over water of the standard deviation/mean ratio is 0.084, and this value is incorporated in our model so as to suggest the possible effect of gustiness in the wind in the absence of convective activity. In fact, the streamwise component of boundary layer wind velocity fluctuations is somewhat skewed, but in the context of the model this is a minor correction and does not merit the extra computational effort. The principal effect of including wind gustiness in the model is to soften the low–wind speed cutoff brought about by viscous dissipation. Otherwise for a given water temperature T, and salinity S, there would be an even sharper drop to zero, as in the work of *Pierson and Stacy* [1973], at that wind speed where (11) becomes zero. The measurements of Pierson and Stacy were made in a laboratory tank with steady winds. The gustiness was therefore much lower than that typical of the marine atmospheric boundary layer.

There remains the step of applying the two scale backscatter theory given by *Valenzuela* [1978] to the wave number spectra derived above. The equations to be used are equations (5.1), (5.2), and (5.4) from Valenzuela, with some differences, which are reproduced here by (25), (26), and (27):

$$\sigma_{HH}^0(\theta_i) = 16\pi k_0^4 \cos^4 \theta_i \left| \left(\frac{\alpha \cos \delta}{\alpha_i}\right)^2 g_{HH}(\theta_i) + \left(\frac{\sin \delta}{\alpha_i}\right)^2 g_{VV}(\theta_i) \right|^2 \Phi_1(2k_0\alpha, 2k_0\gamma \sin \delta) \tag{25}$$

$$\sigma_{VV}^0(\theta_i) = 16\pi k_0^4 \cos^4 \theta_i \left| \left(\frac{\alpha \cos \delta}{\alpha_i}\right)^2 g_{VV}(\theta_i) + \left(\frac{\sin \delta}{\alpha_i}\right)^2 g_{HH}(\theta_i) \right|^2 \Phi_1(2k_0\alpha, 2k_0\gamma \sin \delta) \tag{26}$$

$$\sigma^{0\text{sea}}(\theta) = \int_{-\infty}^{\infty} d(\tan \psi) \int_{-\infty}^{\infty} d(\tan \delta)\sigma^0(\theta_i)P(\tan \psi, \tan \delta) \tag{27}$$

In (25) and (26), θ is the radar incidence angle and ψ and δ are the angular deviations of the normal to the surface caused by the tilting waves in and perpendicular to the plane of incidence, respectively. The resultant instantaneous angle of incidence is $\theta_i = \cos^{-1}$ [$\cos (\theta + \psi) \cos \delta$]. Also, $\alpha_i = \sin \theta_i$, $\alpha = \sin (\theta + \psi)$, $\gamma = \cos (\theta + \psi)$, and g_{HH} and g_{VV} are the first-order scattering coefficients for horizontal and vertical polarization, respectively. They are given by *Valenzuela* [1978, equations (4.6) and (4.7)] and are reproduced here for completeness:

$$g_{HH}(\theta) = \frac{(\varepsilon_r - 1)}{[\cos \theta + (\varepsilon_r - \sin^2 \theta)^{1/2}]^2} \tag{28}$$

$$g_{VV}(\theta) = \frac{(\varepsilon_r - 1)[\varepsilon_r(1 + \sin^2 \theta) - \sin^2 \theta]}{[\varepsilon_r \cos \theta + (\varepsilon_r - \sin^2 \theta)^{1/2}]^2} \tag{29}$$

In (28) and (29), ε_r is the relative (complex) dielectric constant of the water. The values used in this paper for various radar frequencies are summarized in Table 19.

The two-dimensional wave number spectrum $\Phi_1(k_x, k_y)$ and the polar wave number spectrum $\Phi(k, \chi)$ are normalized as in (30), where $\overline{\zeta^2}$ is the variance of the surface elevation:

$$\overline{\zeta^2} = \int_{-\infty}^{\infty} \int_{-\infty}^{\infty} \Phi_1(k_x, k_y)\, dk_x\, dk_y = \int_{-\pi}^{\pi} \int_{-\infty}^{\infty} \Phi(k, \chi)\, dk\, k\, d\chi \tag{30}$$

Equation (26) is used in (27) to account for the effects of the tilting of the longer waves on the backscatter for vertical polarization, and (25) is used in (27) for horizontal polarization. The joint probability density function for the slopes of the tilting waves is represented by $P(\tan \psi, \tan \delta)$ in (27).

As in all two-scale theories, the full wave number spectrum must be divided in some logical way into the part that is only needed to determine the variances of the two components of the slope from the low wave numbers and the part that is kept to compute Bragg scattering from the shorter waves.

The description by *Valenzuela* [1978] of the rationale behind such models is helpful in this context. The patch of tilted sea surface covered by the Bragg waves must contain a sufficient number of these waves to produce some resonant backscatter. It also must be small enough so that the overall effect of variations in the slopes is not too greatly reduced by the application of what is effectively a low-pass wave number filter to the full wave number spectrum. This is accomplished by an appropriate choice of $k_\Gamma(=k/\Gamma)$ in (23) and (24). This separation of scales factor Γ is the final parameter to be chosen for the Bragg-scattering part of the model. The results are weakly dependent on the choice of Γ. By fitting the model to the circle flight data [*Schroeder et al.*, 1984], we have selected $\Gamma = 40$.

The evaluation of (27) requires a triple integration. The normal distribution of the mean wind speed is broken up into ranges uniformly spaced about the mean so that the Bragg part of the model contains the effect of gustiness as just described. For each of these values of the wind, the double integration over slopes is carried out. The weighted sum of the results obtained by this procedure is then the required computed value of the backscatter.

At a given angle of incidence of the radar, θ, the Bragg wave number ($k = 2k_0 \sin \theta$) and thus the variances of slopes of the tilting waves from (23) and (24) are computed. Then the double probability integral is evaluated in the ranges $\pm 4S_x$ and $\pm 4S_y$. Here our method diverges from the conventional methods described by *Valenzuela* [1978]. The nearly Gaussian probability of slopes found by *Cox and Munk* [1954], with slicks present, was obtained from bistatic measurements of sun glitter points on the sea surface with the sun as the radiation source and a special camera as the receiver. Geometrical corrections were made such that the slopes were effectively referred to the local vertical. This is not, of course, what the radar "sees," except at nadir. Thus to account for the fact that a surface tilted toward the radar occupies a larger fraction of the field of view than a surface tilted away, we adjust the probabilities accordingly.

The correction can be shown to be given by (31) if $|\theta + \psi| < \pi/2$, where $z_x = \tan \psi$, $z_y = \tan \delta$.

$$P(z_x, z_y)_{\text{radar}} = IP(z_x, z_y)_{\text{Gaussian}} \frac{\cos (\theta + \psi)}{\cos \psi} \tag{31}$$

If $|\theta + \psi| \geq \pi/2$, the probability is zero. The condition on $\theta + \psi$ rejects from consideration all slopes turned normal, or greater, to the plane of the radar wave front.

The value of I is chosen such that the sum of all probabilities of slopes seen by the radar is unity. A similar approach to adjusting the probability of seeing a particular slope has been taken by *Chan and Fung* [1977], except that they did not account for the invisibility (to the radar) of slopes such that $|\theta + \psi| \geq \pi/2$.

In establishing the limits of integration, the values of $[S_x]_\theta$ and $[S_y]_\theta$ are set using (23) and (24) and the angle of incidence of the radar. However, as the surface tilts, the resonant Bragg wave continually changes and with it the range of wave numbers that can contribute to any particular slope. Consequently, the appropriate probability is not that associated with $S(x, y)_\theta$ but rather that associated with $S(x, y)_{\theta_i}$.

$$P(z_x, z_y)_{\text{Gaussian}} = \frac{\exp\{-\frac{1}{2}[(z_x^2/(S_x^2)_{\theta_i}) + (z_y^2/(S_y^2)_{\theta_i})]\}}{2\pi(S_x)_{\theta_i}(S_y)_{\theta_i}} \tag{32}$$

This has a pronounced effect at small values of θ, for as values of tilt on the edges of the distribution drive θ_i and the Bragg wave number to very small values, the corresponding energy density rises sharply and would artificially augment the modeled backscatter. Of course, the probability of large tilts affecting these longer waves is correspondingly smaller, and (32) weights the contribution from these waves accordingly.

Near normal incidence the wavelength of the Bragg wave rises sharply. However, Bragg scattering is not effective near nadir [*Yaplee et al.*, 1971]. The Bragg-scattering part of a two-scale model with specular backscatter included usually lies well above the specular values for high incidence angles, falls below the specular value at some ill-defined incidence angle between perhaps 15° and 25° usually, and then rapidly increases to values greater than specular for low incidence angles. We therefore impose a cutoff condition on the Bragg backscatter when $\theta_i < 18°$. The choice of 18° is made on the basis of the low-incidence angle circle flight data in the primary data set.

It is noted that the theoretical equations for two-scale models are obtained from a limiting process for which the contribution from the vector wave number spectrum becomes infintesimal as the area sampled becomes infinite. In this sense, the requirement that $ak_0 \ll 1$ for the amplitude of a wave a at the wave number k_0 is always satisfied. This completes the Bragg resonance part of the model.

6. SPECULAR BACKSCATTER

6.1. *Specular Backscatter for Fully Developed Spectra*

Finally, as pointed out by *Barrick and Peake* [1968], we add the specular component for fully developed seas which, following *Valenzuela* [1978], is

$$\sigma_{\text{spec}}{}^0 = \frac{|R(0)|^2 \sec^4 \theta}{2|S_x|_{k_0}|S_y|_{k_0}} \exp\left(-\frac{\tan^2 \theta}{2(S_L{}^2)_{k_0}}\right) \tag{33}$$

where $S_L{}^2$ is the slope variance in the plane of incidence due to waves of wave number k_0/Γ and smaller. $[S_x]_{k_0}$ and $[S_y]_{k_0}$ are the downwind and cross-wind standard deviations of these slopes. The total slope variance $S_L{}^2$ is assumed to have an elliptical variation in χ so that

$$S_L{}^2 = \frac{S_x{}^2 S_y{}^2}{S_y{}^2 \cos^2(\chi - \bar{\chi}) + S_x{}^2 \sin^2(\chi - \bar{\chi})} \tag{34a}$$

Recent laboratory measurements [*Haimback and Wu*, 1986] support this variation in azimuth. $|R(0)|^2$ is the reflection coefficient at normal incidence for the radar frequency of interest, adjusted as was suggested by *Valenzuela* [1978] according to

$$|R(0)| = |0.65(\varepsilon_r - 1)/(\varepsilon_r{}^{1/2} + 1)^2| \tag{34b}$$

where $\varepsilon_r = \varepsilon_r(k_0)$ is the relative (complex) dielectric constant.

6.2. *Departures From the Fully Developed Spectrum of the Model*

Waves are not always in equilibrium with the wind. There is no unique relationship between the full wave spectrum and the local wind speed and direction. For light winds, the gravity waves are usually higher than would be predicted for a fully developed sea, and for high winds, they are usually lower [*Moskowitz*, 1964]. Gravity waves generally lag the wind as the wind increases and lead the wind as it decreases [*Bretschneider et al.*, 1962]. The behavior of the slope spectrum has not been routinely measured. Our model contains most of the slope variance for the specular part at high wave numbers relative to the peak of the elevation spectrum. The upwind and cross-wind slopes differ by less than 30% in general (see Figure 12), so that specular backscatter is more nearly isotropic. For a given wind, slope variances that are 10% to 20% less or 10% to 20% higher than those of the model for the intermediate range of wind speeds would not be unusual.

The slope variances given by (23) and (24) may be too low for light winds over many parts of the ocean. After the wind dies down, the previously generated spectrum for the gravity waves will continue to be present until the waves have propagated out of the area. They continue to contribute to the slopes of the surface even though they are no longer associated with the local wind speed. Conversely, as was discussed in section 5.5, nonfully developed seas could have slope variances smaller than those found for our model.

6.3. *Swell Plus a Low-Wind Sea*

The integrals of the slope spectrum that are needed for a two-scale model most of the time over most of the ocean are probably more nearly in equilibrium with the wind than those are for the elevation spectrum, but conditions for which they are not must be identified and analyzed properly. A frequent wave condition of importance to scatterometry is one where a low-wind sea generated by a light wind is accompanied by a swell traveling at a considerable angle to the wind.

For various combinations of light wind seas and swells at an angle to the wind sea, the maxima and minima for the specular backscatter need not be in the local wind direction. Some of the results of the circle flight data may be explainable, especially for low incidence angles, by these effects. As the incidence angle is increased, specular backscatter becomes less important, and more of the high-wave number part of the composite spectrum enters into the computation of the slopes to be used in the Bragg part of the model. These spectral components are more likely to be in equilibrium with the local wind, and the slopes computed for a fully developed sea may then be the appropriate slopes to use.

6.4. *Measurements of Slope Spectra*

The probability density function for the slopes given by (32) for the actual seas present is needed to compute the Bragg backscatter especially for incidence angles from about 15° to 25°. If these slopes could be measured by another instrument on a spacecraft, the determination of the wind that caused the Bragg waves would become more accurate. Alternatively, the gravity wave part of the spectrum might be predictable from a wave model. Equations (32) and (33) can be generalized to account for any slope spectrum for the tilting waves and the specular backscatter.

An instrument has been developed and proven to perform satisfactorily from aircraft altitudes that would measure exactly the quantities needed in the above equations, plus those for even more complex wave conditions. The main purpose of this instrument is to estimate directional wave spectra, but the quantity actually measured is $\partial\zeta/\partial r$ in a polar coordinate system for varying χ from which the slope spectrum can be found as in $k^2\,\Phi(k, \chi)$ $[dk\ k\ d\chi]$. This method for measuring the gravity wave elevation spectrum thus essentially depends on the uniqueness of the polar wave number slope spectrum for each sea condition. Appropriate integrals then define any possible combination of slopes for the above analysis. This instrument is described by *Jackson et al.* [1985*a*, *b*].

7. THE AAFE RADSCAT DATA

7.1. *Data Properties*

The Advanced Applications Flight Experiment (AAFE) radiometer scatterometer (RADSCAT) was used to measure the normalized radar backscattering cross section from the sea surface for varying wave, wind, and other environmental conditions. The data from this extensive program are given by *Schroeder et al.* [1984] and have been archived as was described by *Schroeder and Mitchell* [1983]. *Schroeder et al.* [1985] have described these results in abbreviated form, but the primary source for the data that are used in this paper is *Schroeder et al.* [1984].

Eight missions were flown starting in April 1973 and ending in March 1977 with the instrument installed on a NASA C130 aircraft. At first, upwind, downwind, and cross-wind level flights were made. The development of the circle flight maneuver in which both horizontally polarized and vertically polarized backscatter values were measured concurrently as a function of aspect angle for a nearly constant incidence angle provides the data used to tune and test the model described in the preceding material. The level flight data, the functional check flight data, data that are anomalous, and data for which the required oceanographic and meteorological measurements are incomplete have been discarded.

The remaining data are treated as primary data and supplementary data. The primary data, used to tune the model, were chosen by the criteria that the wind is reported to be accurate to within ± 1 m s^{-1} and that the correlation coefficient between the azimuthal analytical fit used by *Schroeder et al.* [1984] and the data is greater than 0.5 as summarized in Table 1. There were 24 circle flights selected in this way for the primary data set. Data for horizontal polarization for one flight were missing because the in-flight calibration procedures did not produce reliable values for a 7.5 m s^{-1} reported wind. The data have been grouped first in incidence angle ranges near 20°, 30°, 40°, 58°, and 67° and then by increasing wind speed.

Table 2 provides additional data for these same 24 flights with backscatter data only for vertical polarization. The water temperature, air temperature, wind direction, location, aspect angle shape parameters (i.e., A_2/A_0 and A_1/A_0; see (42)), the normalized standard deviation (i.e., the standard deviation divided by the mean), and a subjective judgment on the symmetry of the basic data and the quality of the overall fit are tabulated. Roughly, A_1/A_0 reflects the downwind/upwind difference while A_2/A_0 reflects the cross-wind/upwind difference.

For this primary subset, the reported winds varied from 5.5 to 20.0 m s^{-1}, and the incidence angles varied from 18.9° to 68.1°. The reported water temperatures varied from 8.5°C to 17.7°C. Salinity was not reported, but the effect of salinity is relatively minor. Since our results predict backscatter values that depart substantially from a power law for both low and high winds and depend on water temperature, data of comparable quality and completeness for winds below 5 m s^{-1} and above 20 m s^{-1} for water temperatures ranging from 0°C to 30°C will be needed for full verification.

The site, or sites, at which the wind was measured was not at the same location as the measurement of the backscatter. As the aircraft circled and measured the backscatter while trying to maintain a nearly constant bank angle, to be added to the antenna level flight depression angle, it would be advected by the wind at flight altitude a considerable distance so that the sea surface area sampled during the entire flight would be roughly enclosed by a rectangle bounded by two half circles.

A given data point consisted of the measured backscatter from a small surface area of the ocean compared with the areas sampled by the SASS on Seasat. Each "spot" measurement was highly variable because backscatter is a noiselike signal subject to Rayleigh fading. Moreover, one single circle flight required an hour or so for completion. The winds measured at a site nearby were not averaged over the full duration over the line and run. The actual averaging time for the reported 19.5-m wind varied from one mission to another. Mesoscale turbulent fluctuations in the wind from one radar sample to the next, gradients in the wind field as the aircraft moved with the wind at flight altitude, and the variability of the wind at the site of the conventional measurements all combine to make the meteorologically measured wind and the value of the wind speed to be associated with a given set of circle flight data somewhat uncertain. The estimated accuracies of the winds given by *Schroeder et al.* [1984] are qualitative judgements based on the nature of the conventional measurements. The actual uncertainty in the meteorological wind may be even greater than 1 m s^{-1} for the best data and 1.5 m s^{-1} for the supplementary data to be described below.

Although, Schroeder et al. give more precise locations for the circle flights, the separation between the sea surface areas that were sampled and the meteorological instruments for measuring the winds does not merit more than a general location for each circle flight. This is indicated in Tables 2 and 3 by identifying data from the North Sea by PISA, which is a scientifically instrumented tower, and *Hotel*, which was a weather ship off the east coast of the United States, now replaced by a national data buoy. We have carried the reported meteorological wind speed to a tenth of a meter per second. The actual wind is not known at all that well.

The 19.5-m winds reported by Schroeder et al. have had the effects of stability removed by means of the Monin-Obukhov theory [*Monin and Obukhov*, 1954] and refer to neutral stability winds. The equations were closed by a relationship between u_* and z_0 given by *Cardone* [1969], with possible modifications. Such corrections have little effect on $\bar{U}(19.5)$ when different closures are used (i.e., *Garratt* [1977] and *Cardone* [1969] versus (14)) but can result in substantial differences in the wind stress and in the variation of wind with height close to the sea surface.

7.2. *Supplementary Data*

The subset of 24 vertically polarized circle flight values has been augmented by most of the rest of the circle flight data with the exceptions of the functional check flights for mission 306, all of the data for mission 288, and the data for mission 238, flight 27, line 4, run 2. The values for these flights disagree substantially with all of the rest of the data so that they were omitted as apparent "outliers." Table 3 provides a summary of the environmental data and the properties of the supplementary data that were not used to tune the model. The sup-

TABLE 1. Summary of the Best Circle

			$\sigma_{VV}{}^0$				$\sigma_{VV}{}^0$(dB)				
M/F/L/R	$\bar{\theta}$	$\bar{u}$	$A_0 \times 10^3$	$A_1 \times 10^3$	$A_2 \times 10^3$	R^2	UP	DN	CR	$\bar{U}_{(19.5)}$, (dB)	$\left(\frac{\sigma_{VV}{}^0(\mathrm{UP})}{\sigma_{VV}{}^0(\mathrm{CR})}\right)_{\mathrm{dB}}$
318/17/4/1	19.8	13.5	516.6	−51.61	148.5	0.811	−2.12	−1.45	−4.34	11.30	2.22
335/5/4/1	19.9	15.5	632.9	−8.40	235.5	0.655	−0.66	−0.571	−4.01	11.90	3.35
335/4B/4/1	19.0	19.1	802.7	−94.86	247.6	0.539	−0.20	+0.59	−2.56	12.81	2.36
335/4A/4/1	18.9	19.8	833.6	−29.74	321.0	0.807	+0.511	+0.74	−2.902	12.97	3.41
318/24/4/1	30.3	9.5	59.14	10.21	25.29	0.815	−10.24	−11.29	−14.70	9.78	4.46
318/14/4/7	39.9	5.5	3.97	0.81	1.80	0.762	−21.82	−23.05	−26.64	7.40	4.82
318/19/4/13	40.9	7.5	10.47	0.93	6.394	0.879	−17.50	−17.98	−23.90	8.75	6.40
318/16/4/9	39.4	8.2	9.153	1.50	5.65	0.732	−17.88	−18.76	−24.55	9.14	6.67
318/18/4/6	40.4	11.3	17.51	4.634	12.67	0.877	−14.58	−15.93	−23.15	10.53	8.57
318/17/4/8	40.8	12.8	25.7	3.98	15.42	0.911	−13.46	−14.30	−19.88	11.07	6.42
335/6/4/9	39.1	15.0	37.74	6.541	17.45	0.748	−12.09	−13.13	−16.93	11.76	4.84
335/5/4/9	39.4	15.2	39.52	5.693	18.55	0.706	−11.95	−12.81	−16.78	11.82	4.83
353/11/4/11	39.7	15.7	41.95	7.26	19.10	0.792	−11.66	−12.69	−16.41	11.96	4.75
335/4B/4/10	38.7	19.4	69.39	14.97	27.17	0.710	−9.53	−10.88	−13.74	12.88	4.21
335/4A/4/9	39.1	20.0	55.18	0.113	26.67	0.760	−10.86	−10.88	−15.45	13.01	4.59
335/6/4/13	57.8	15.0	12.53	3.17	5.31	0.857	−16.78	−18.34	−21.41	11.76	4.63
335/5/4/17	58.5	15.1	12.58	3.103	5.132	0.789	−16.82	−18.35	−21.28	11.79	4.46
335/4A/4/17	58.2	19.8	15.09	4.643	5.18	0.753	−16.04	−18.06	−20.04	12.97	4.00
318/14/4/12	67.2	5.5	0.783	0.081	0.42	0.874	−28.93	−29.52	−34.35	7.40	5.42
318/19/4/17	67.1	7.5	2.573	0.39	2.034	0.893	−23.01	−23.75	−32.68	8.75	9.67
318/16/4/14	66.2	8.9	2.87	0.161	2.23	0.851	−22.79	−23.07	−31.93	9.49	9.14
318/18/4/11	65.5	10.5	6.67	0.46	4.84	0.935	−19.22	−19.57	−27.37	10.21	8.15
318/17/4/12	68.1	12.3	6.311	1.512	3.752	0.913	−19.36	−20.68	−25.92	10.90	6.56
353/11/4/1	67.3	16.0	8.62	2.834	4.34	0.825	−18.02	−19.95	−23.69	12.04	5.67

$\bar{U}$ is effective neutral wind at 19.5 m. M/F/L/R is mission/flight/line/run. An ellipsis denotes missing data.

plementary data are used only for the vertically polarized measurements. The data that have been added are for circle flights with estimated wind speed accuracies poorer than ± 1 m s^{-1} and with R^2 less than 0.5. Only four circle flights were accepted for tuning at an incidence angle near 20°. The new set consists of a grand total of 18 circle flights for 20°. Of the ones for 20° that have been added, only one has an R^2 greater than 0.5. Others have R^2 values of 0.05, 0.15, and 0.17, which are quite low and need to be explained.

There are a number of circle flights from mission 353 in the supplementary data. The winds for this mission were obtained in three different ways. National data buoy EB16 at 42.5°N, 130°W was one source. Other winds were obtained through a combination of measurements from the Naval Ocean Systems research tower near San Diego and from inertial navigation winds measured by the NASA C130 at altitudes varying from 85 to 212 m. Especially for light winds, the winds at the San Diego tower are influenced by a sea breeze effect and are not very representative of the winds farther offshore. The calculation of the effective neutral wind at 19.5 m from winds measured at these higher elevations is usually not reliable enough to yield a wind within an estimated accuracy of 1 m s^{-1}. Those entries in Table 3 for R^2 values greater than 0.5 were excluded from the primary data set for three reasons. They are that (1) the winds were categorized as fair, (2) the winds were based on tower data too close to shore, and (3) the winds were based on winds measured by the C130 and calculated from boundary layer theory.

7.3. *RADSCAT Calibration Procedures*

The aircraft radar used by *Schroeder et al.* [1984] had four parallel receiver signal detectors that were fed received power split four ways by a divider. The signal was conditioned by attenuators and amplifiers such that the 15-dB range of each detector was staggered so that a dynamic range of approximately 60 dB was achieved. For high incidence angles and low values of the received power, the highest gain channel was used. Even then, at times, no signal was measured for some aspect angles of the circle flights as shown in plots similar to Figure 8 to follow, especially for horizontal polarization. See, for example, pages 34, 37, 38, and 50 of *Schroeder et al.* [1984].

Amplifying circuits always amplify both the desired backscattered power and the communication noise (or internal noise) of the amplifier. After sufficient amplification, the signal (the backscattered power) plus the noise power is converted to an integrated voltage for a number of radar pulse transmissions so as to be able to calculate the normalized backscattering cross section. As in the Seasat SASS, the effect of this communication noise was accounted for in the evaluation of the data by laboratory, aircraft premission, and in-flight calibration procedures as detailed by *Schroeder et al.* [1984 and references therein]. Data on these calibration procedures have been provided to us (L. C. Schroeder, personal communication, 1985). The exhaustive efforts to account for communication noise, and the quantitative determination of its effect on the data make the RADSCAT data of great value in understanding the differences between models of radar backscatter and measured values of radar backscatter.

As the comparisons between the model and the AAFE RADSCAT data were calculated, it appeared that not only were the effects of the unknown position of the minimum near cross wind important because of the data analysis method but also the differences between the model and the data were

Flight Data From *Schroeder et al.* [1984]

$\left(\frac{\sigma_{VV}{}^0(\mathrm{UP})}{\sigma_{VV}{}^0(\mathrm{DN})}\right)_{\mathrm{dB}}$	$\sigma_{HH}{}^0$				$\sigma_{HH}{}^0$(dB)			$\sigma_{VV}{}^0/\sigma_{HH}{}^0$(dB)		
	$A_0 \times 10^3$	$A_1 \times 10^3$	$A_2 \times 10^3$	R^2	UP	DN	CR	UP	DN	CR
−0.67	555.5	−30.38	143.4	0.688	−1.75	−1.37	−3.85	−0.37	−0.08	−0.49
−0.08	640.6	10.74	235.4	0.642	−0.522	−0.63	−3.92	−0.133	+0.06	−0.09
−0.79	815.8	−40.67	259.0	0.571	+0.15	+0.48	−2.54	−0.344	+0.114	−0.02
−0.22	844.4	−0.613	319.7	0.797	+0.66	+0.662	−2.80	−0.15	+0.073	−0.102
1.05	38.63	8.093	12.84	0.745	−12.25	−13.63	−15.89	2.01	2.34	1.19
1.23	2.024	1.00	0.82	0.865	−24.16	−27.34	−29.19	2.34	4.29	2.55
0.48	5.182	1.86	2.56	0.834	−20.18	−22.31	−25.81	2.68	4.33	1.91
0.88	5.04	2.23	2.60	0.739	−20.06	−22.67	−26.12	2.18	3.91	1.57
1.35	9.41	3.87	4.44	0.822	−17.52	−20.01	−23.04	2.94	4.08	−0.11
0.84	14.10	5.26	7.611	0.898	−15.69	−17.84	−21.88	2.23	3.54	2.0
1.04	20.48	6.94	8.62	0.728	−14.43	−16.54	−19.26	2.34	3.41	2.33
0.86	22.82	7.03	10.29	0.699	−13.96	−15.84	−19.02	2.01	3.03	2.24
1.03	22.82	7.872	9.771	0.700	−13.93	−16.07	−18.84	2.27	3.38	2.43
1.35	44.81	.64	16.63	0.703	−11.19	−13.30	−15.50	1.66	2.42	1.76
0.02	31.70	2.33	15.93	0.737	−13.01	−13.44	−18.02	2.15	2.56	2.57
1.56	3.002	1.50	1.25	0.800	−22.41	−25.60	−27.55	5.63	7.26	6.14
1.53	3.013	1.68	1.410	0.684	−22.15	−25.61	−27.95	5.33	7.26	6.67
2.02	4.43	2.301	1.41	0.706	−20.89	−24.51	−25.20	4.85	6.45	5.16
0.59	0.15	0.061	0.03	0.473	−36.35	−39.59	−39.24	7.42	10.07	4.89
0.74	...	...	...	...	...	...	...	...	...	...
0.28	0.27	0.154	0.163	0.762	−32.34	−35.59	−39.83	9.55	12.52	7.90
0.35	1.07	0.38	0.66	0.917	−26.77	−28.69	−33.84	7.55	9.12	6.47
1.32	0.98	0.681	0.462	0.914	−26.74	−31.20	−32.88	7.38	10.52	6.96
1.93	1.443	1.10	0.81	0.779	−24.76	−29.38	−31.96	6.74	9.43	8.27

larger for the higher incidence angles and lighter winds. The laboratory and in-flight calibration procedures provide data on this source of variability.

The equation for σ^0 for a pencil beam radar as in the above reference is (35), where the notation is defined by *Schroeder et al.* [1984], and only V_{sea}, V_{cal}, τ_{cal}, τ_{sea}, and $\cos\theta$ need to be considered for our purposes. When expressed in decibels, σ^0 is the sum of 11 terms, and each term can be considered separately:

$$\sigma^0 = (16\pi)^2 \frac{A^2}{\lambda^2 V_{\mathrm{cal}}\tau_{\mathrm{sea}}} \frac{V_{\mathrm{sea}}\tau_{\mathrm{cal}}\chi(GXR)}{G^2\beta^2 \cos\theta} \tag{35}$$

Seven different sources of bias for the calculated values of the backscatter were identified. Some were constants that could be found to a certain level of accuracy and used to eliminate most of their effects.

The quantity V_{cal} was determined in the laboratory and accounts for the nonlinear response of each of the four gain channels, with the effect of receiver noise removed, for calibrated input signals. It represents the transmitted power, when divided by τ_{cal}, and at most a correction of 1 db or so to the calculated value of σ^0. The four gain channels all together covered a dynamic range from −98 dBm to −40 dBm where the quantity dBm refers to the input signal in watts relative to 1 mW. The received power varied from 10^{-7} W to 1.58×10^{-13} W. The four channels overlapped so that the middle range for each channel departed from linearity by only about ±0.2 dB. However, the lowest-gain channel, used for the strongest return signals, was less linear and exceeded ±1 dB over its dynamic range. The highest-gain channel introduced difficulties in the measurement of very low signals at high incidence angles for low winds because of receiver noise. In the laboratory the integration time τ_{cal} could be much longer, so that the quantities V_{cal} and τ_{cal} were well measured especially with reference to the self-noise, or communication noise, of each channel.

During a particular circle flight, τ_{sea} had to be selected so as not to cover too large a variation in aspect angle. For flights for the earlier missions, an integration time of from 0.1 to 0.925 s was used. For later flights, 0.5 s was the minimum used. Also, an appropriate gain channel was selected so as to be as close as possible to the nearly linear part of the calibration for that channel. Important sources of possible bias were found to be in the determination of V_{sea}, which represents the time integrated received power as a voltage, and in θ and in the interaction of these two quantities. The incidence angle θ varied from one measurement to the next because of variations in the bank angle of the circling aircraft.

A range gate was set so as to activate the radar receivers for any backscattered power within the range of variability of the aircraft altitude and incidence angle. The backscattered power was also passed through Doppler band pass filters to reduce further unwanted receiver noise. Variations in the bank angle caused the signal to shift back and forth from one band pass filter to another, and this effect contributed to the possible bias of measurement.

Finally, the receiver noise, or self-noise, or communication noise, was not constant for a particular gain channel but varied both as a function of time and from one circle flight to another. The "zero" levels of each channel were measured for each circle flight so that their effect could be subtracted from the voltage representing the backscattered power so as to compute V_{sea}. The communication noise was quite small and could be measured only to one significant figure, although it

TABLE 2. Additional Data for the Best 24 Circle Flights

M/F/L/R	$\bar{\theta}$, deg	$\bar{U}$, m s^{-1}	$\bar{\chi}$, deg	Sea, m	Swell, m	TW, °C	TA, °C	Location	A_2/A_0	A_1/A_0	R^2	NSD	Symmetry	Quality
318/17/4/1	19.8	13.5	220	1.5	···	17.7	18	PISA	0.29	−0.01	0.81	0.11	E	E
335/5/4/1	19.9	15.5	300	3	3.4	12.0	−2	*Hotel*	0.37	−0.01	0.65	0.19	F	G
335/4B/4/1	19.0	19.1	295	5/5.5	···	13.4	3	*Hotel*	0.31	0.12	0.54	0.21	G	G
335/4A/4/1	18.9	19.8	280	3	···	8.5	−1	EB41	0.35	−0.04	0.81	0.13	E	E
318/24/4/1	30.3	9.5	230	2.7	···	16.0	17	PISA	0.43	0.17	0.81	0.16	E	E
318/14/4/7	39.9	5.5	60	1.1	···	12.2	···	PISA	0.45	0.20	0.76	0.21	G	G
318/19/4/13	40.9	7.5	260	2.4	···	17.4	17	PISA	0.61	0.089	0.88	0.16	G	G
318/16/4/9	39.4	8.2	210	···	···	17.2	16	PISA	0.62	0.16	0.73	0.27	F	F
318/18/4/6	40.4	11.3	205	1.8	···	17.2	19	PISA	0.72	0.27	0.88	0.20	G	G
318/17/4/8	40.8	12.8	220	1.5	···	17.2	18	PISA	0.60	0.16	0.91	0.13	E	E
335/6/4/9	39.1	15.0	285	2.5	4.3	13.7	8	*Hotel*	0.46	0.17	0.75	0.21	G	G
335/5/4/9	39.4	15.2	300	3.8	1.8	11.5	−2	*Hotel*	0.47	0.14	0.71	0.72	G	G
353/11/4/11	39.7	15.7	260	5.5/6.0	···	10.6	9	EB16	0.46	0.17	0.79	0.17	G	G
335/4B/4/10	38.7	19.4	295	5/5.5	···	13.4	3	*Hotel*	0.39	0.22	0.71	0.20	G	G
335/4A/4/9	39.1	20.0	280	3	···	8.5		EB41	0.48	0.002	0.76	0.19	E	E
335/6/4/13	57.8	15.0	275	2.5	4	13.7	8	*Hotel*	0.42	0.25	0.86	0.14	G	G
335/5/4/17	58.5	15.1	300	3	3.4	11.5	3	*Hotel*	0.41	0.25	0.79	0.17	F	G
335/4A/4/17	58.2	19.8	285	3	···	8.5	−1	EB41	0.34	0.31	0.75	0.18	G	E
318/14/4/12	67.2	5.5	60	1.1	···	12.2	···	PISA	0.53	0.10	0.87	0.15	G	G
318/19/4/17	67.1	7.5	260	2.4	···	17.4	17	PISA	0.79	0.16	0.89	0.20	G	G
318/16/4/14	66.2	8.9	220	1.1	···	17.7	16	PISA	0.78	0.56	0.85	0.24	E	E
318/18/4/11	65.5	10.5	205	1.8	···	17.7	19	PISA	0.73	0.069	0.93	0.14	F	F
318/17/4/12	68.1	12.3	220	1.5	···	17.7	18	PISA	0.60	0.24	0.91	0.30	E	E
353/11/4/1	67.3	16.0	260	6.0	5.5	10.6	9	EB16	0.50	0.33	0.83	0.20	F	G

Headings are as follows: M/F/L/R, mission/flight/line/run; $\bar{\theta}$, incidence angle; $\bar{U}$, 19.5-m wind; χ, direction; sea, significant wave height; swell, significant swell height, if any; TW, water temperature; TA, air temperature; R^2, correlation coefficient; NSD, normalized standard deviation. Symmetry is about $\chi = 180°$, and quality refers to goodness of overall fit. Notation for symmetry and quality is as follows: E, excellent; G, good; F, fair (subjective judgment). An ellipsis denotes missing data. Ratios A_2/A_0 and A_1/A_0 are for vertical polarization.

could vary by a factor of about 5 over the range of circle flight measurements. Its value could make quite a difference in the calculated value of σ^0. Under some conditions, when the receiver noise voltage was subtracted, the result was a negative number. For conditions such as these, a low cutoff voltage level was established for each channel for use in calculating the backscatter. A dynamic range of 60 dBm was thus not quite able to encompass all measurement from nadir to incidence angles of 67°.

These laboratory and in-flight calibration procedures gave an estimate of the bias for the backscatter measurement which was removed during the calculation of each value of σ^0. This bias varied as a function of the fluctuation in θ as χ varied and as a function of the in-flight receiver noise as well as from other sources not described above. However, this estimate of the bias is itself somewhat uncertain, and the true bias could have been either lower or higher than the value actually used.

As far as testing the model for backscatter derived in the preceding material is concerned, various sources of error could be combined and described by the quantity ${\sigma_{error}}^0$, given in decibels, to be added to, or subtracted from, the measured backscatter values in decibels so as to bound the measurements in the rms sense by about 1 standard deviation. This quantity is given in Table IV of *Schroeder et al.* [1984] along with other pertinent data for upwind, downwind, and cross wind for each circle flight.

Table IV of *Schroeder et al.* [1984] shows values of ${\sigma_{error}}^0$ that vary from a low of ± 0.24 dB to a high of ± 2.49 dB. This residual unknown effect of bias does not uniformly increase with increasing incidence angle. It can be high when the measurements are made at the low end of a particular receiver gain channel. The values of ${\sigma_{error}}^0$ will be used in the section to follow in the comparison of the model results with the measured backscatter values. The additional effect of the integration over τ_{sea} of a return signal subject to Rayleigh fading on the received power as it randomly affects each individual measurement is also given in Table IV in terms of $\Delta\sigma^0/\sigma^0$ in percent. This additional variability is difficult to interpret in terms of the model that was used to fit the data by *Schroeder et al.* [1984].

7.4. *Data Analysis Methods*

The regression fits to the circle flight data were obtained in antilog form with a model given by

$$\sigma^0 = A_0 + A_1 \cos \chi + A_2 \cos 2\chi \tag{36}$$

Equation (36) is in terms of three parameters (A_0, A_1, A_2) as given in Tables 1, 2, and 3. The location of the minimum near 90° is a function of A_1 and A_2 and depends solely on whether upwind backscatter is stronger than downwind, or vice versa, since setting the first derivative of (36) equal to zero yields

$$\cos \chi_{min} = -A_1/4A_2 \tag{37}$$

The function, $\sigma^0(\bar{U}, \chi, \theta)$ is relatively flat as a function of χ near its maxima and minima, and the scatter of the original data makes it virtually impossible to locate the minima within $\pm 20°$, or so, of 90° for vertical polarization.

For horizontal polarization, the upwind-downwind difference in backscatter is large with downwind consistently less than upwind. The use of only three terms in a Fourier series then forces the minimum at crosswind to shift past 90° by a considerable amount. With χ equal to 90°, (36) becomes

$$\sigma^0(90°) = A_0 - A_2 \tag{38}$$

but with χ equal to (37), (36) becomes

$$\sigma^0(\chi_{min}) = A_0 - A_2 - (A_1{}^2/8A_2) \tag{39}$$

The difference between (38) and (39) amounts to only a few tenths of a decibel for most circle flights for vertical polarization, but it can be more than 1 dB for horizontal polarization. Equation (36) cannot produce both a minimum close to 90° for horizontal polarization and a pronounced upwind/downwind difference. Table 4 shows the values obtained from (37), (38), and (39). Both ways will be used to interpret the results for horizontal polarization.

Since backscatter is proportional to the spectral components propagating in a direction parallel to the radar look direction either toward or away from it, then if there were no upwind/downwind asymmetry, the minima would occur at exactly $\pm 90°$. The fact that upwind is generally larger than downwind, especially for horizontal polarization, moves the minima closer to downwind, but only by a small amount in our model.

The values of A_0, A_1, and A_2 as tabulated also yield backscatter at upwind and downwind:

$$\sigma_{UP}{}^0 = A_0 + A_1 + A_2 \tag{40}$$

$$\sigma_{DN}{}^0 = A_0 - A_1 + A_2 \tag{41}$$

Cross wind could equally well be interpreted to be given at 90° by either (38) or (39) because of the scatter in the data near cross wind. The question of the exact location of the minimum cannot be decided on the basis of the analysis of either *Wentz et al.* [1984] or *Schroeder et al.* [1984] because of the choice of the analytical form that was used. Displacements of 10°, if they are incorrect, propagate into wind recovery algorithms as incorrect 20° changes in wind direction and produce complicated effects in the algorithms. More refined experiments and data analysis procedures are needed to settle the question experimentally.

A useful form from (36) is (42), and in decibels the result is (43). There must be certain constraints on A_0, A_1, and A_2; otherwise the term in brackets following A_0 in (42) could become negative and could not be calculated.

$$\sigma^0 = A_0[1 + (A_1/A_0) \cos \chi + (A_2/A_0) \cos 2\chi] \tag{42}$$

$$\sigma_{dB}{}^0 = 10 \log_{10} A_0 + 10 \log_{10} [1 + (A_1/A_0) \cos \chi + (A_2/A_0) \cos 2\chi] \tag{43}$$

The difficulties in obtaining a model that will predict upwind, downwind, and cross-wind backscatter values from a wave number spectrum as defined previously are illustrated by the values of A_1A_0 and A_2/A_0 as given in Tables 2 and 3 for vertical polarization. For incidence angles near 20° for both kinds of data, the average value of A_2/A_0 is 0.24, with a standard deviation of 0.08. The average value of A_1/A_0 is -0.008, with a standard deviation of 0.086. The minima are somewhere within 5° of 90° and 270°, but the upwind/cross-wind ratio can vary between 3 and 1.5 dB. The preference for upwind to exceed downwind, or conversely, is not marked.

For incidence angles near 40°, the average value of A_2/A_0 is 0.51, with a standard deviation of 0.12. The average value of A_1/A_0 is 0.20, with a standard deviation of 0.13. Two of the values of A_1/A_0 are essentially zero. The upwind/cross-wind ratio can vary between 7 and 3.5 dB for data with similar conditions at 1 standard deviation. For 67° the corresponding values are 0.64, with a standard deviation of 0.12, and 0.21, with a standard deviation of 0.13. Since these values vary even for nearly the same wind speed and incidence angle, a model of backscatter might only be able to recover correct values for some combination of the three values at upwind, cross wind, and downwind but not necessarily either at all three or, consistently, for just one aspect angle.

These features of the data are also emphasized in figures given by *Schroeder et al.* [1984]. Their Figures 11, 12, 13, 14, 15, and 16 graph the fitted curves as in (36) for nominal groupings at 20°, 30°, 40°, 50°, 60°, and 70° incidence angle. At 20° for nominal winds from 2.5 to 19.1 m s^{-1} some of the curves have virtually no contribution from A_1 and A_2 and are nearly constant versus azimuth angle. Others have substantial differences between upwind or downwind and cross wind. The curve for 2.5 m s^{-1} falls about 3 dB above the one for 4.6 m s^{-1}.

At a nominal 30° incidence angle, four curves differ by about 3 dB in an irregular way for winds of 15, 23.6, 21.5, and 14.2 m s^{-1}. At 40° there are numerous examples of differences in range for nearly equal wind speeds. For 50°, 60°, and 70° incidence angle groupings, the same general comments apply.

The methods used to determine the coefficients in (42) would be very powerful if the data points were uniformly scattered over 360°. Random fluctuations from one part of the circle flight to another are suppressed, but gaps in the data could cause the three Fourier coefficients to be calculated incorrectly. The model is not quite sophisticated enough to locate the actual minima near cross wind and to decide whether or not they are at, or close to, 90° and 270°.

The SASS 1 model function used for the Seasat SASS [*Schroeder et al.*, 1982*b*] forced the minima to be at 90° and 270°, but the method used gave unrealistic results for high winds. Better ways to decide this question need to be found because the difference between horizontal and vertical polarization is important for the success of future remote sensing systems, and mislocated minima can cause errors in the recovery of the wind direction.

Results of the analysis of the data for mission 318 by a different method were provided (L. C. Schroeder, personal communication, 1985). The recovered backscatter values were aligned to make $\chi = 0$ the upwind direction and corrected to nominal incidence angles as tabulated below. The values were averaged over 10° intervals, and the standard deviations for those averages near upwind, downwind, and cross wind wind were found. At times, the ranges that were averaged were, 0° to 10°, 10° to 20° and so on; at other times the values were from 355° to 5°, 5° to 15°, and so on; and at other times they were centered on 2°, 12°, and so on. The individual points did not always follow a smooth curve over 360°.

The aspect angles for the maxima and minima for some of the circle flights for mission 318 are given in Table 5 along with an indication of whether or not the data are symmetric about 180°. If the variability of the averages is such that the maxima and minima could fall at 0° and 180° and at 90° and 270°, respectively, the value is shown with an asterisk. The data processed in this way give no indication either that the minima are affected by the upwind/downwind difference for

TABLE 3. Supplementary AAFE Circle

M/F/L/R	$\bar{\theta}$, deg	$\bar{U}$, m s^{-1}	$\bar{\chi}$, deg	Sea, m	Swell, m	TW, °C	TA, °C	Location	$A_0 \times 10^3$
353/20/4/1	20.0	2.5	245	...	...	15	13	33°N, 117.5°W	213.8
353/15/4/11	20.0	4.2	255	...	...	15	...	33°N, 117°W	252.4
318/13/4/3	20.3	4.6	200	smooth	smooth	15	...	PISA	91.11
353/21/4/7	19.6	4.7	290	...	...	15	10	33°N, 117.5°W	214.6
353/10/4/1	19.9	5.4	210	...	...	14	13	33°N, 117.5°W	190.04
318/14/4/1	18.9	5.5	60	1.1	...	15	...	PISA	304.4
318/19/4/10	19.7	7.5	260	2.4	...	17	17	PISA	383.4
318/16/4/4	18.5	8.6	210	1.1	...	18	16	PISA	410.6
353/13/4/1	20.3	10.4	315	...	...	15	14	33°N, 117.5°W	450.1
353/9/4/11	19.7	10.8	305	...	...	14	12	33°N, 117.5°W	405.66
318/18/4/2	19.6	12.0	205	1.8	...	18	19	PISA	455.7
353/14/4/6	19.3	14.3	285	2.5	4	14	9	EB16	632.9
335/6/4/1	19.2	15.0	285	2.5	4	14	9	*Hotel*	676.6
353/11/4/6	19.3	15.9	260	5.5/6	...	11	19	EB16	769.9
230/20/4/2	31.0	6.5	...	...	...	15			27.32
335/3/4/1	29.4	14.2	280	2	...	19	18	37°N, 73°W	116.26
353/20/4/26	38.9	2.5	245	...	...	16	13	33°N, 117°W	1.589
353/15/4/16	40.1	4.2	...	...	...	15	...	33°N, 117°W	2.60
318/13/4/9	40.6	4.6	150	smooth	smooth	15	...	PISA	2.786
353/21/4/12	39.4	4.7	290	...	...	15	11	33°N, 118°W	1.22
353/9/4/16	39.7	10.3	315	...	...	14	11	*Hotel*	12.8
353/13/4/20	40.5	12.0	...	...	...	15	14	33°N, 117°W	22.0
353/14/4/11	39.4	14.3	285	3.0/3.5	...	10	5	EB16	31.64
318/13/4/11	50.3	4.6	150	smooth	smooth	17	...	PISA	1.122
335/3/4/6	48.3	14.2	280	2	...	19	18	39°N, 73°W	21.00
335/4B/4/17	58.0	19.6	295	5	5.5	13	3	*Hotel*	17.193
353/9/4/6	67.3	11.3	305	2.5	4	14	12	33°N, 117.5°W	3.45
353/13/4/16	67.7	11.7	305	...	...	15	14	33°N, 117.5°W	4.70
353/14/4/1	67.1	14.3	280	3.0	3.5	10	5	EB16	7.301

Headings are as follows: M/F/L/R, mission/flight/line/run; $\bar{\theta}$, incidence angle; $\bar{U}$, 19.5-m wind; $\bar{\chi}$, direction; sea, significant wave height; swell, significant swell height, if any, TW, water temperature; TA, air temperature; NSD, normalized standard deviation; symmetry is about $\chi = 180°$, and quality refers to goodness of overall fit. Notation for symmetry and quality is as follows: E, excellent; G, good; F, fair; P, poor; VP, very poor; VVP, very, very poor (subjective judgment). An ellipsis denotes missing data.

*Upwind.

horizontal polarization or that they are at any aspect angles other than 90° and 270°.

The effect of an additional constant bias on the evaluation of σ^0 can be investigated in a simple way by replacing V_{sea} in (35) by

$$V_{sea} = V_{sea(true)} + V_{error} \quad (44)$$

where both V_{error} and $(\sigma^0 E)^*$ are constants so that

$$\sigma^0 = \sigma_T{}^0 + (\sigma^0 E)^* \quad (45)$$

To relate $(\sigma^0 E)^*$ to the $\sigma_{error}{}^0$ in decibels of *Schroeder et al.* [1984], the steps shown in (46) can be used:

$$\begin{aligned}\sigma_{dB}{}^0 &= 10 \log_{10} (\sigma_T{}^0 + (\sigma^0 E)^*) \\ &= 10 \log_{10} \sigma_T{}^0 + 10 \log_{10} [1 + ((\sigma^0 E)^*/\sigma_T{}^0)]\end{aligned} \quad (46)$$

so that

$$\sigma_{error(dB)}{}^0 = 10 \log_{10} [1 + ((\sigma^0 E)^*/\sigma_T{}^0)] \quad (47)$$

For upwind UP, downwind DN, and cross wind CR from the waves, the previously given equations then become (48), (49), and (50) (not decibels!):

$$\sigma_{UP}{}^0 + (\sigma^0 E)^* = A_0 + A_1 + A_2 \quad (48)$$

$$\sigma_{DN}{}^0 + (\sigma^0 E)^* = A_0 - A_1 + A_2 \quad (49)$$

$$\sigma_{CR}{}^0 + (\sigma^0 E)^* = A_0 - A_2 \quad (50)$$

These equations can be solved for A_0, A_1, and A_2 as follows:

$$A_0 = [(\sigma_{UP}{}^0 + \sigma_{DN}{}^0)/4] + (\sigma_{CR}{}^0/2) + (\sigma^0 E)^* \quad (51)$$

$$A_1 = (\sigma_{UP}{}^0 - \sigma_{DN}{}^0)/2 \quad (52)$$

$$A_2 = [(\sigma_{UP}{}^0 + \sigma_{DN}{}^0)/4] - (\sigma_{CR}{}^0/2) \quad (53)$$

Consequently, the backscatter from the waves can be represented in terms of the parameters of *Schroeder et al.* [1984] by

$$A_{0(new)} = A_0 - (\sigma^0 E)^* \quad (54)$$

$$A_{1(new)} = A_1 \quad (55)$$

$$A_{2(new)} = A_2 \quad (56)$$

The average value of the backscatter from the waves is reduced, but the calculated coefficients of the sinusoidally varying terms do not change to the level of approximation of the postulated fit to the data when the effect of a possible error in the measurement of communication noise is introduced. The shape of the curve in decibels changes as shown by (43), since A_0 is decreased in the second term.

Actually, $(\sigma^0 E)^*$ needs only to be moved to the right-hand side of (48), (49), and (50) to correct for noise. The values for $\sigma_{UP}{}^0$, $\sigma_{DN}{}^0$, and $\sigma_{CR}{}^0$ are all reduced, but the effect near cross wind is the largest. The effect of a correction for communication noise is most pronounced for cross wind when these

Flight Data for Vertical Polarization

$A_1 \times 10^3$	$A_2 \times 10^3$	$\sigma_{VV}{}^0 \times 10^3$*	$\sigma_{VV(dB)}{}^0$*	A_2/A_0	A_1/A_0	R^2	NSD	Symmetry	Quality
−20.2	54.7	248.3	−6.05	0.27	−0.095	0.40	0.23	F	F
20.5	61.12	339.0	−4.76	0.24	0.081	0.39	0.23	F	F
−8.14	26.4	109.4	−9.61	0.29	−0.089	0.36	0.29	F	F
−8.53	14.64	220.7	−6.56	0.107	−0.040	0.05	0.26	F	F
15.3	34.1	239.4	−6.21	0.18	0.081	0.15	0.34	VVP	VVP
−16.74	33.25	320.9	−4.94	0.11	−0.055	0.38	0.11	F	F
−64.2	70.7	389.9	−4.09	0.18	−0.17	0.44	0.20	P	P
−63.3	64.6	412.0	−3.85	0.16	0.15	0.19	0.32	P	P
−30.0	146.9	567.0	−2.46	0.33	−0.067	0.56	0.21	G	G
30.9	104.04	540.6	−2.67	0.26	0.076	0.35	0.26	VP	VP
−30.0	56.4	482.1	−3.17	0.12	0.066	0.17	0.22	G	P
−8.4	235.5	860.0	−0.655	0.17	0.04	0.30	0.19	F	F
−43.8	183.9	816.7	−0.879	0.27	0.065	0.44	0.23	P	F
−56.5	236.4	940.8	−0.224	0.31	0.074	0.43	0.26	G	G
−2.87	8.84	33.29	−14.78	0.32	−0.11	0.38	0.31	F	G
−5.83	80.57	171.0	−7.67	0.52	0.050	0.84	0.16	E	E
0.433	0.46	2.486	−26.04	0.29	0.27	0.26	0.46	VP	VP
0.92	1.44	4.95	−23.05	0.55	0.35	0.55	0.41	P	P
0	1.65	4.44	−23.53	0.59	0	0.92	0.12	G	G
0.34	0.36	1.91	−27.19	0.29	0.28	0.37	0.37	VVP	VVP
7.57	8.44	28.8	−15.40	0.66	0.59	0.64	0.47	VVP	VVP
4.1	12.45	38.55	−14.14	0.57	0.19	0.81	0.20	F	F
5.74	15.44	52.82	−12.77	0.49	0.18	0.79	0.19	P	P
0.33	0.77	2.22	−26.54	0.69	0.29	0.89	0.19	F	F
−0.32	9.78	30.46	−15.16	0.47	0.02	0.87	0.12	E	E
2.86	1.85	21.9	−16.60	0.11	0.17	0.36	0.19	VP	VP
1.09	2.05	6.59	−21.81	0.60	0.32	0.62	0.33	VVP	VVP
1.92	3.51	10.12	−19.95	0.75	0.41	0.90	0.20	F	F
2.13	3.53	12.96	−18.87	0.48	0.29	0.80	0.21	P	P

values are finally converted to decibels, since (50) is the smallest of the three expressions, and even subtracting a small constant from this quantity can have a large effect.

7.5. *Examples of the Circle Flight Data*

Thirteen examples of the circle flight data, with details given in Tables 1, 2, and 3, are shown in Figure 8. Five are for an incidence angle near 20°, three for an angle near 40°, one is for 50°, and two are for 67°. The last panel combines 40° and 67°.

Each dot represents an individual measurement of backscatter. The size of the sample and the data processing methods varied because the program lasted for several years and the data processing methods were changed. For a 20° incidence angle, with increasing wind, the amplitude of the A_2 term decreases as the nominal wind increases from 4.6 to 5.5 m s^{-1}. For the data for 353/10/4/1, the data scatter in a different way between 180° and 360° than from zero to 180°. The A_2 oscillation for 318/14/4/1 is barely perceptible in the actual data. For the two highest winds, the fit according to (36) is reasonable, but the last of the examples is not symmetrical about 180°.

For 40°, the cos 2χ oscillation is well defined for the first two examples. The cos χ effect is very small. For the 12.0 m s^{-1} example, one might argue that the cross-wind minima computed by averaging the actual data near 90° and 270° would be lower than the curve-fitting method would compute.

For 4.6 m s^{-1} at 50.3° and 11.7 m s^{-1} at 67.7°, the data do not scatter in the same way to each side of 180°. Depending on whether one picked 90° or 270° to be the minimum, cross wind would be different by several decibels. The reasons for these departures from an even function about 0° (or 180°) are not clear. Sampling variability might be one explanation. Systematic departures from the nominal incidence angle as a function of the position of the aircraft during the circle flight might be another.

The bottom right panel of Figure 8 shows the data for 353/9/4, runs 16 and 6. It would not be possible to model these raw data, and the fit to the data by (36) is catagorized as very very poor in the tables.

These last two circle flights represent the poorest fit between the modeling equation (equation (36)) and the actual data. The data are considered to be correct and not the result of some instrument failure. There are times and places over the ocean where backscatter does not fit the presently available methods to analyze it and predict it.

7.6. *The Use of the AAFE Data to Test the Model*

The AAFE circle flight data set is the only presently available one that allows some of the parameters of the model to be fitted at K_u band. Other parameters were fixed independently of these data. In the next section, the model is fitted to

TABLE 4. Properties of the Primary Data Near Cross Wind

		Vertical Polarization				Horizontal Polarization			
$\bar{\theta}$, deg	$\bar{U}$, m s^{-1}	$\sigma_{VV}{}^0(\chi_{\min})$	$\sigma_{VV}{}^0(90°)$	Difference	$\chi_{\min}$, deg	$\sigma_{HH}{}^0(\chi_{\min})$	$\sigma_{HH}{}^0(90°)$	Difference	$\chi_{\min}$, deg
19.8	13.5	−4.37	−4.34	−0.03	85.0	−3.86	−3.85	−0.01	87.0
19.9	15.5	−4.01	−4.01	0.00	89.5	−3.92	−3.92	0.00	89.3
19.0	19.1	−2.59	−2.56	−0.03	84.5	−2.55	−2.54	−0.01	87.8
18.9	19.8	−2.905	−2.902	−0.003	88.7	−2.80	−2.80	0.00	90.0
30.3	9.5	−14.77	−14.70	−0.07	95.8	−15.99	−15.89	−0.10	99.1
39.9	5.5	−26.73	−26.64	−0.09	96.5	−29.78	−29.19	−0.59	107.8
40.9	7.5	−23.92	−23.90	−0.82	92.1	−26.10	−25.81	−0.19	100.5
39.4	8.2	−24.62	−24.55	−0.07	93.8	−26.57	−26.12	−0.45	102.4
40.4	11.3	−23.35	−23.15	−0.20	95.2	−23.42	−23.04	−0.38	102.6
40.8	12.8	−20.24	−19.88	−0.32	93.7	−22.19	−21.88	−0.31	99.9
39.1	15.0	−16.99	−16.93	−0.06	95.4	−19.52	−19.26	−0.26	101.6
39.4	15.2	−16.83	−16.78	−0.05	99.4	−19.23	−19.02	−0.21	99.8
39.7	15.7	−16.48	−16.41	−0.07	95.6	−19.12	−18.84	−0.28	101.6
38.7	19.4	−13.85	−13.74	−0.11	97.9	−15.76	−15.50	−0.26	102.7
39.1	20.0	−15.45	−15.45	0.00	90.1	−18.03	−18.02	−0.01	92.1
57.8	15.0	−21.56	−21.41	−0.15	98.6	−28.16	−27.55	−0.11	107.5
58.5	15.1	−21.42	−21.28	−0.14	98.7	−28.69	−27.95	−0.74	107.3
58.2	19.8	−20.27	−20.04	−0.23	102.9	−25.93	−24.20	−1.73	114.1
67.2	5.5	−34.42	−34.35	−0.07	92.8	−39.81	−39.24	−0.57	120.6
67.1	7.5	−32.76	−32.68	−0.08	92.7	...	...	...	...
66.2	8.9	−31.95	−31.93	−0.02	91.0	−40.52	−39.83	−0.69	103.7
65.5	10.5	−27.39	−27.37	−0.02	91.4	−34.17	−33.84	−0.33	98.3
68.1	12.3	−26.05	−25.92	−0.13	95.8	−34.06	−32.88	−1.18	111.6
67.3	16.0	−23.93	−23.69	−0.24	99.4	−33.50	−31.96	−1.54	109.8

Backscatter values are in decibels.

vertically polarized data. Our best efforts to tune the model for vertical polarization still yielded differences at the higher incidence angles.

A model and the data used to try to validate it can disagree in a number of ways. The reported wind could differ from the wind for a more representative average. The correction for the effect of receiver noise might not have been the right one. The waves, as described in section 10, may not correspond to full development. Each of these potential sources of disagreement is considered in comparing the model and the data in what follows.

8. Results for Vertical Polarization at K_u Band

8.1. *General Features of the Backscatter Predicted by the Model*

Figure 9 shows the dependence of backscatter in decibels for the wave number of the SASS on the log of the effective neutral wind at 19.5 m as predicted by the model for vertical polarization at upwind for incidence angles from 20° to 70° and for sea surface temperatures of 0°C and 30°C. The relative dielectric constant [*Saxton and Lane*, 1952] used in the model was $\varepsilon_r = 39 - i38.5$, corresponding to seawater at 10°C. The lines are not straight lines, and there is no power law. Over limited ranges for each incidence angle, the curves could be fitted by a straight line within 1 dB, but there would be difficulties for winds under 6 m s^{-1} and over 16 m s^{-1}.

The curves are extended to below −45 dB. For a slightly lighter wind for each curve according to the model, they would go to minus infinity, and the backscatter as a number before conversion to decibels would be identically zero for winds lower than the speed shown on the graph. The model predicts that there is no backscatter at all for winds below certain threshold speeds and that this threshold speed is a function of incidence angle and water temperature. (See also Figure 4). Winds near 5 m s^{-1} over cold water return no backscatter for a fully developed sea at incidence angles of 60° or more according to the model. Over the range of wind speeds from 2 to 5 m s^{-1}, depending on incidence angle and water temperature, the backscatter can vary by 15 dB for changes of wind speed of a meter per second or less.

The material following (16) and section 4 requires a revision of the interpretation of this feature of the model. The Bragg waves that are involved at K_u band can be maintained by physical mechanisms other than the ones modeled by (5) and (7) [*Kahma and Donelan*, 1987]. For light winds, these waves lie within the atmospheric laminar boundary layer and are maintained by laminar shear flow balanced by viscous dissipation. They must therefore be extremely low. The variance spectrum given in (25) and (26) which is needed to compute σ^0 would be 2 orders of magnitude, or more, lower than the spectrum computed from (12) if the threshold wind is not exceeded. The transition from wave generation in the laminar boundary layer by laminar shear flow to wave generation by fully turbulent flow may occur at the wind speeds and water temperatures diagrammed in Figure 4. Thus the curves in Figure 9 may not go to minus infinity but may level off to describe the laminar regime so as to give backscatter values of perhaps −40 to −50 dB. It appears at present to be difficult to design and manufacture radars with the needed signal to noise properties. These low values may be indistinguishable from a backscatter measurement of zero in antilog form.

For speeds of 6 to 12 m s^{-1} the backscatter is predicted to be several decibels higher over warm water than over cold

TABLE 5. Results of Alternative Analysis of Data From Mission 318

F/L/R	θ_c	Maximum Near 0°	Minimum Near 90°	Minimum Near 270°	Maximum Near 180°	Even
			Vertical Polarization			
17/4/1	20°	5°*	85°*	265°*	165°†	E
24/4/1‡	30°	5°*	95°*	265°*	185°*	E
14/4/7	40°	355°*	85°*	255°*	195°†	E
19/4/13	40°	2°*	82°*	262°*§	192°†	E
16/4/9‡	40°	360°	90°	270°	180°	
18/4/6	40°	355°*	95°*	275°*	185°*	E
17/4/8	40°	0°‖	85°*	265°*	185°*	E
14/4/12	65°	5°*	95°*	275°*	185°¶	E
19/4/17	65°	2°*	92°*	272°*	190°*	
16/4/14	65°	350°*	60°*	250°*	185°*	
18/4/11††	65°	5°*	95°*	255°*	185°*	
17/4/12	65°	15°†	85°*	265°*	185°*	E
Total		11	11	10	9	
			Horizontal Polarization			
17/4/1	20°	355°*	85°*	265°*	175°*	E
24/4/1‡	30°	355°*	90°	270°	200°**	E
14/4/7	40°	355°*	105°*	255°*	195°*	E
19/4/13	40°	0°	90°	260°*	200°†	E
16/4/9‡	40°	360°	90°	270°	180°	
18/4/6	40°	355°*	95°*	265°*	185°*	E
17/4/8	40°	345°†	85°*	275°*	175°†	
14/4/12	65°	345°†		anywhere		
19/4/17	65°		no data except near upwind			
16/4/14	65°	342°*	72°*	242°*	162°*	
18/4/11††	65°	0°‡‡	105°*	275°*	175°*	
17/4/12	65°	345°*	95°*	235°*¶	205°*	
Total		8	10	9	7	

Total is essentially at 0°, 90°, 270°, and 180°. The column headed "even" is a quantitative judgment of symmetry about 180°.

*Could easily be 0°, 90°, 180° or 270° based on scatter of points nearby.

†Nearby points not in confidence interval.

‡Not zeroed, appropriate shift made.

§Second minimum at 282°.

‖Backscatter at 90° and 270° differs by 9.2 dB.

¶No points for 245° to 285°, data very irregular.

**Erratic near 180° ± 20°.

††Backscatter at 90° and 270° differs by 3 dB.

‡‡Flat within confidence interval −25° to +25°.

water for the same wind speed and incidence angle. A power law model such as the SASS 1 for Seasat would thus recover higher winds over warm water than over cold water compared with the actual wind.

For still higher winds, the predicted value of the backscatter saturates for wind speeds ranging from 30 to 50 m s^{-1}. These winds are hurricane force, or higher, and there are little or no data to support this predicted saturation. There are data, to be described in another paper, to support a decreasing sensitivity of backscatter to wind speed for winds in this range [*Black et al.*, 1985; *Jones et al.*, 1982; *Delnore et al.*, 1985; *Woiceshyn et al.*, 1986].

The curves in Figure 9 may extend past the region of validity of the model. Even if winds of 50 m s^{-1} were to occur over the ocean, they would be found over very small areas, such as near the eye wall of a hurricane or a typhoon. The wave number spectrum for a fully developed sea would not exist, fortunately, for these areas of high wind simply because the fetches and durations required to generate such waves are far too large.

The rise at low wind speeds of 20 dB, or so, over a fraction of a meter per second is not as steep as it would be if a constant mean wind had been used in the model. The normal distribution of locally mean winds for the high–wave number part of the spectrum represents the effect of mesoscale variability over an area of a size sampled from spacecraft altitudes. Some percentage of the total area has Bragg scatterers present, whereas for the remaining area there are none of importance.

The effect can be even more dramatic for backscatter measured for light wind conditions from aircraft flying at lower altitudes, as was illustrated by *Valenzuela et al.* [1985]. Results from aircraft level flights at an altitude of 150 m with an X band radar at various headings over a portion of Nantucket shoals near 40° 48′N and 69° 12′W are shown in Figures 4 and 15 of their paper for times when the wind measured nearby fluctuated between 3.4 and 4.7 m s^{-1} and for times when the wind varied between 10.4 and 12.2 m s^{-1} for an incidence angle of 45°. Sea surface temperature varied from 11°C to 16°C, but the temperature field probably changed rapidly during the observations because of substantial tidal currents and sharp gradients between different water types. In Figure 4 of the cited paper, for the lighter winds the relative backscattered power could not be separated from the noise by the radar that was used along a portion of a flight leg. Then it would increase by 10 dB with fluctuations for a while and then drop to undetectable values again. Figure 15 of Valenzuela et al. also shows the same effect for measurements at light winds, but for a high wind the backscattered power was present all of the time and fluctuated in the vicinity of 12 or 13 dB. The dynamic range of the radar for the received power in watts would be about a factor of 20 above some unspecified noise level equal to 1.

The full situation was quite complex, and *Valenzuela et al.* [1985] attribute these measurements to the effect of submarine topography and currents. An alternate possibility is that the Bragg waves simply dissappeared according to (13) whenever the fluctuating effective wind relative to the currents was below the threshold value of our model for whatever water temperature was present.

It would be useful to repeat similar experiments for light winds over deep water in the absence of strong currents and temperature gradients so as to determine whether or not this on-off property of the backscattered power is the result of the temperature dependent threshold wind speeds required by (13).

The reason for the predicted saturation for high winds is found in (15). The terms in square brackets are 1 followed by a negative term involving the wind dependent drag coefficient. If k is in the Bragg K_u band, the values of $\bar{U}(\pi/k)$ first increase with increasing $\bar{U}(10)$ and then decrease. Although $\bar{U}(10)$ gets higher and higher, the wind shear near the wavy surface becomes so large that $\bar{U}(\pi/k)$ begins to decrease and the Bragg waves become lower. The spectral behavior in Figure 7 also shows this effect, as was discussed previously.

It is recognized that there are many other physical effects at high winds that are not contained in this model. They are reviewed by *Atlas et al.* [1986]. Others have been described by *Banner and Fooks* [1985]. Some could cause the backscatter to continue to increase. Others could cause an even sharper decrease. Nevertheless, the sea surface elevations in even the highest wind seas are quasi-Gaussian, and there are large areas of nonbreaking waves where Bragg scattering should be dominant.

At 35 m s^{-1} the $\pm 10\%$ requirement on scatterometry pro-

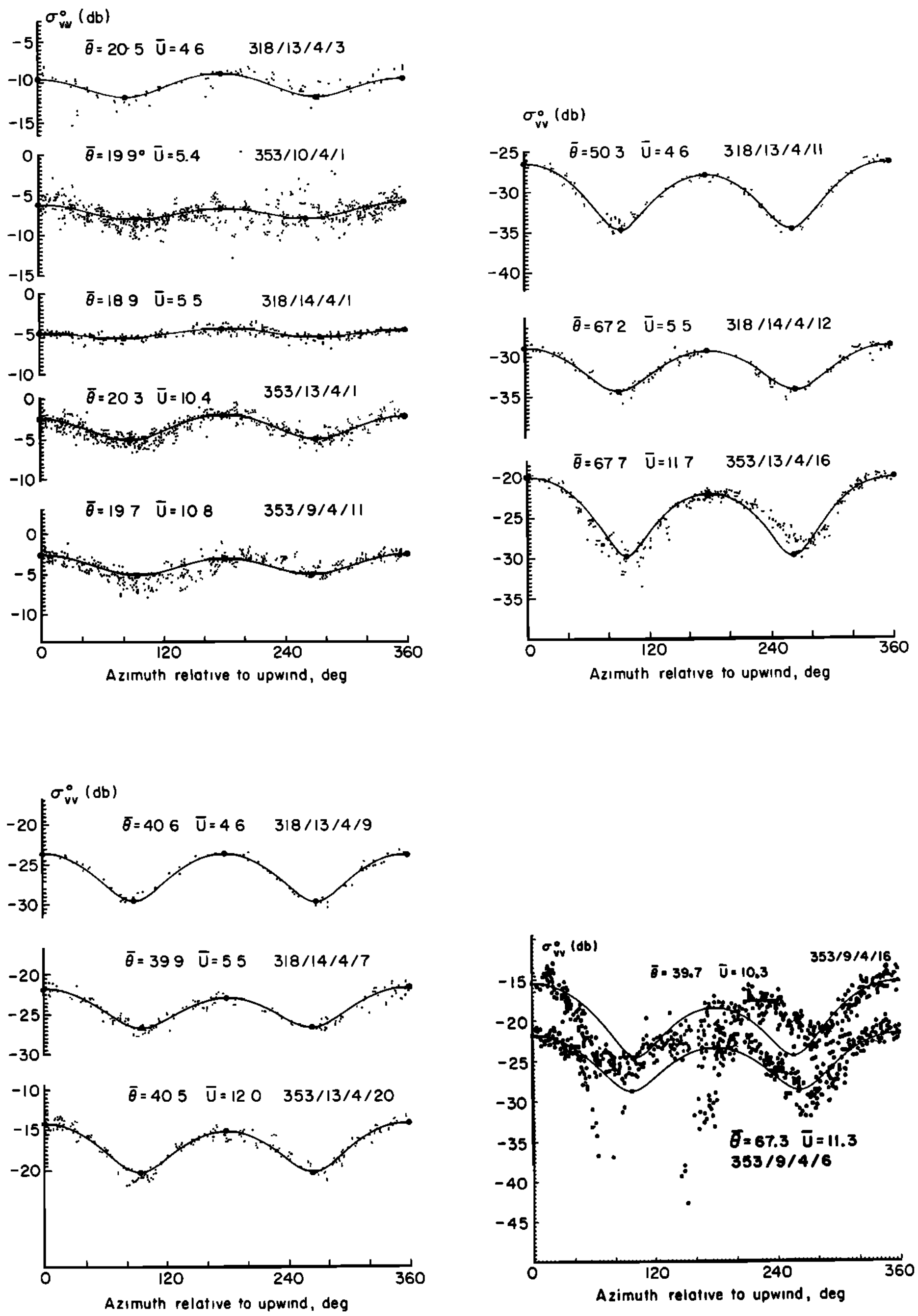

Fig. 8. Examples of AAFE circle flight data. Each dot represents a measurement. Redrafted from *Schroeder et al.* [1984].

vides a range from 31.5 to 38.5 m s^{-1} for which the recovered wind would be considered acceptable. If the decrease in backscatter above a certain speed for vertically polarized measurements can be verified, limited areas of such high winds can be accounted for by more sophisticated wind recovery algorithms.

Figures 10 and 11 show the effect of water temperature more clearly for 40° and 50° incidence angles, respectively, over the range of wind speeds from 7 to 19 m s^{-1}. The curves for 30°C and 0°C are separate even for a wind of 19 m s^{-1}. For 40° incidence angle (Figure 10) at 10 m s^{-1} the predicted backscatter values differ by 0.54 dB, and at 15.85 m s^{-1} ($\log_{10}$ 15.85 = 1.2), they differ by 0.24 dB. Were the curve for 0°C water used over the entire ocean, for 30°C water a wind of 10.72 m s^{-1} would be recovered when in fact it was 10 m s^{-1}, and a wind of 16.59 m s^{-1} would be recovered when in fact it was 15.85 m s^{-1}. The actual backscatter values (not decibels) are shown on the figure. They differ by 0.00378 and 0.00360 from one wind to another.

The same effect is shown in Figure 11 for a 50° incidence angle. The curves appear to converge with increasing wind speed on a log-log plot, whereas they remain nearly the same distance apart in antilog form. Water temperature affects the recovery of wind speeds from backscatter whenever Bragg scattering is important.

The contribution from specular reflection is important for our model for low incidence angles. This is shown by Figure 12 for a temperature of 30°C and by Figure 13 for a temper-

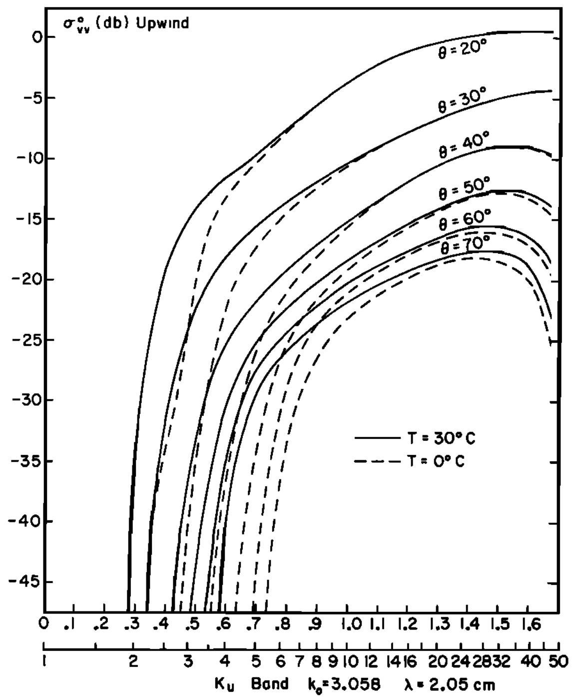

Fig. 9. Vertically polarized backscatter for the two-scale model for K_u band at upwind with $\log_{10} \bar{U}(19.5)$ in meters per second on the abscissa and $\sigma_{VV}{}^{0}$ in decibels on the ordinate. The solid curves are for a water temperature of 30°C and the dashed curves are for a water temperature of 0°C. θ is the incidence angle. The auxiliary scale is the wind speed at 19.5 m in meters per second.

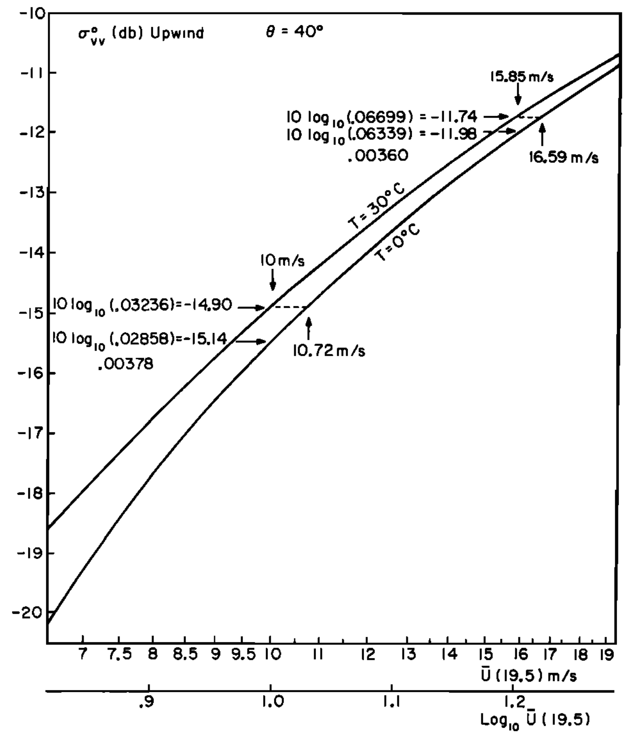

Fig. 10. Detail of the effect of water temperature on backscatter at an incidence angle of 40° for winds from 7 to 19 m s^{-1}.

ature of 0°C. For 30°C and 20° incidence angle in Figure 12, the specular contribution to the total backscatter is more important than the Bragg contribution for winds above the point where the curves for Bragg and specular cross, which occurs at about 6 m s^{-1}. For 30° incidence angle, specular is down by 20 dB at 10 m s^{-1} and is not important compared with Bragg scattering for lighter winds. Specular exceeds Bragg only for very high winds.

The upwind and crosswind slopes that are used to tilt the Bragg scatterers are also graphed by means of an auxiliary scale on the right of Figure 12. The low–wave number spectrum is truncated at $k/40$ so that the slopes are less at 20° than at 30°. The specular slopes are computed for $k_0/40$ and thus correspond to the lines for 30°.

The corresponding curves in Figure 13 for 0°C water differ from the curves for 30°C water only in the behavior of the Bragg contribution. Specular backscatter has not changed because the wave numbers involved are not affected strongly by viscosity. The Bragg contribution decreases for all wind speeds. At 20° incidence angle, the Bragg contribution for winds near 2 m s^{-1} for 30°C water has disappeared, and the backscatter for the lightest winds is due to specular reflection. Bragg exceeds specular only over a small range of light winds.

For a 20° incidence angle, specular reflection combines with Bragg scattering in an important way for all water temperatures and cannot be ignored in calculating the total backscatter for any wind speed. For a 30° incidence angle, the effect of specular reflection becomes detectable for winds over 8 m s^{-1} for both temperatures and dominates for very high winds. For higher incidence angles, the effect of specular reflection as computed in this model can be usually neglected for K_u band.

8.2. *Comparison With the Primary Data Set in Terms of Wind Speed Errors*

Table 6 compares the backscatter values predicted by the model for the frequency of the RADSCAT with the backscatter values of the primary data set. The comparisons are in

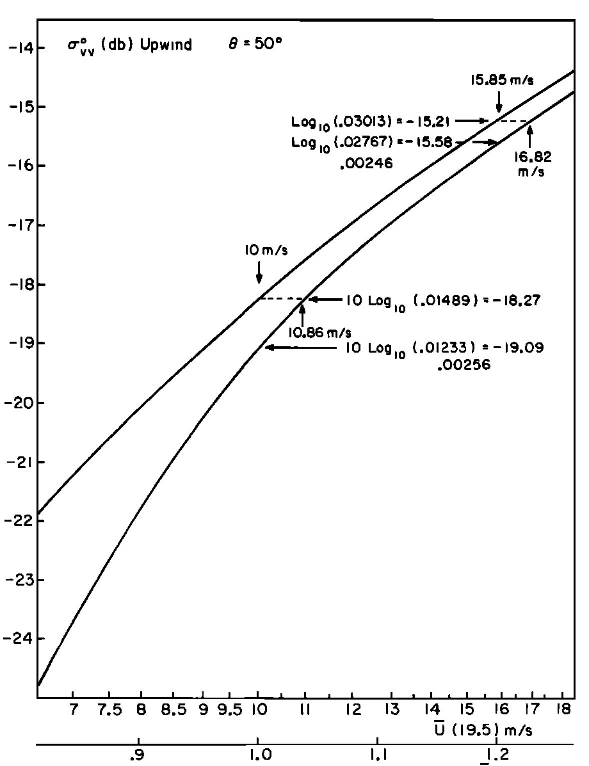

Fig. 11. Detail of the effect of water temperature on backscatter at an incidence angle of 50° for winds from 7 to 18 m s^{-1}.

the same order as the data given in Tables 1 and 2. The same dielectric constant was used for both the SASS and the RADSCAT along with the appropriate slightly different radar wave numbers. The incidence angle, wind speed, and viscosity, from the reported water temperature, are shown at the start of each row of data followed by three groups of results for upwind, cross wind, and downwind. For each group of nearly constant incidence angle, the reported wind increases as tabulated. The backscatter would be expected to increase also. Values that are out of order in this sense are shown by an asterisk in the table.

The measured backscatter value is given first, followed by values calculated from the model for the reported wind and for winds 1 m s^{-1} less and 1 m s^{-1} greater than the reported wind. At times, the range of backscatter values from the model is quite large. For the 67.2° incidence angle 5.5 m s^{-1} wind, the computed backscatter for 4.5 m s^{-1} at cross wind is -97.43 dB, and for 6.5 m s^{-1} it is -39.15 dB. Other ranges are in excess of 10 dB.

The columns headed UP, CR, and DN for upwind, cross wind, and downwind show whether or not the computed backscatter for $\bar{U} - 1$ to $\bar{U} + 1$ from the theory encloses the measured value and, if not, whether the computed values were higher or lower than the measured values. For upwind, for example, nine of the backscatter ranges enclose the measured value, five are high, and ten are low, and so on, for cross wind and downwind. Of the 72 possible comparisons, 42% of the computed backscatter values could be made to agree with the measured value by changing the wind speed by less than 1 m s^{-1}. Thirty-nine percent of the ± 1 m s^{-1} ranges of backscatter are too low, and 19% are too high. The last three

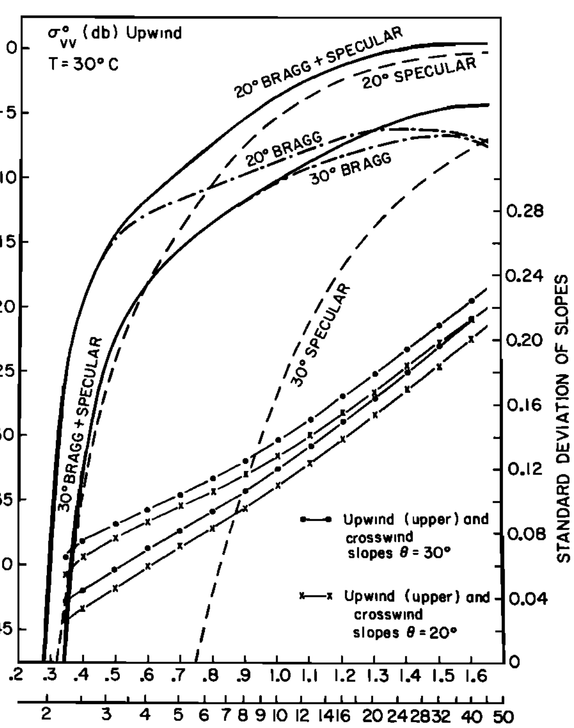

Fig. 12. Combined effects of specular reflection and Bragg scattering at incidence angles of 20° and 30° for a water temperature of 30°C with vertically polarized backscatter at upwind on the ordinate. Log wind speed at 19.5 m in meters per second and wind speed are on the abscissa. The standard deviations of the upwind and cross-wind slopes for 30° and 20° are shown on the auxiliary scale on the right.

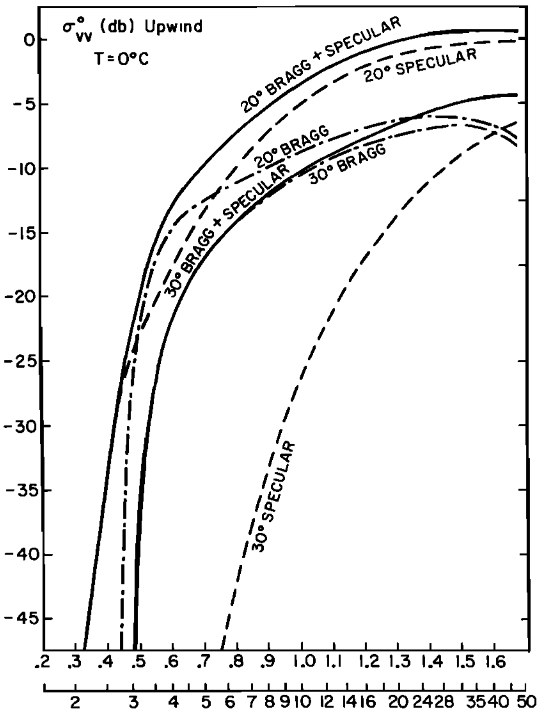

Fig. 13. Combined effects of specular reflection and Bragg scattering at incidence angles of 20° and 30° for a water temperature of 0°C with upwind vertically polarized backscatter on the ordinate. Log wind speed at 19.5 m in meters per second and wind speed are on the abscissa.

columns show how well each circle flight is predicted by the model.

Figures 14, 15, and 16 show how well the calculated and measured backscatter values agree for upwind, cross wind, and downwind. The measured values are the abscissa, and the computed values are the ordinate. The vertical bars bounded by horizontal lines show the effect of a range of ± 1 m s^{-1} on the computed backscatter. Bars are not shown if the range of the backscatter values is about the same as the size of the coded symbol.

The upwind and downwind values cluster closely about the best agreement 45° line. The cross-wind values scatter by much larger amounts above and below the 45° line.

Table 7 shows how well the theoretical values of backscatter for the reported water temperature and wind at 19.5 m agree with the fitted values of backscatter from (26) and (27). The table is stratified according to incidence angle and wind direction and then pooled both for all directions, all incidence angles, and the total sample. The calculated values for cross wind for an incidence angle of 67.2° and a reported wind of 5.5 m s^{-1} introduces a large error in all of the statistics that use these values. The table shows how the results differ when this one outrider at cross wind is discarded. For the entire sample of 72 pairs, eight differ by more than 2 dB. These are two values at crosswind for θ near 39.8°, three values at crosswind for θ near 58.2°, and one value each at upwind, downwind, and cross wind for θ near 66.9°. With only the one outrider removed, the bias for the entire sample is -0.28 dB, and the rms variability is ± 1.22 dB. This table assumes that the reported wind, temperature, and measured backscatter are correct.

TABLE 6. Comparison of Measured and Calculated Values for Vertically Polarized Backscatter if Errors for Winds are ± 1 m s^{-1}

			$\sigma_{VV(\mathrm{dB})}^0$												Measured Versus Calculated			Count		
$\bar{\theta}$, deg	$\bar{U}$, m s^{-1}	Viscosity	Upwind Measured	Upwind Calculated $\bar{U}-1$	$\bar{U}$	$\bar{U}+1$	Crosswind Measured	Cross Wind Calculated $\bar{U}-1$	$\bar{U}$	$\bar{U}+1$	Downwind Measured	Downwind Calculated $\bar{U}-1$	$\bar{U}$	$\bar{U}+1$	UP	CR	DN	I	L	H
19.8	13.5	0.0106	−2.12	−1.95	−1.57	−1.25	−4.34	−5.05	−4.39	−3.80	−1.45	−1.90	−1.52	−1.20	H	I	I	2		1
19.9	15.5	0.0124	−0.66	−1.30	−1.02	−0.78	−4.01	−3.94	−3.47	−3.05	−0.57	−1.26	−0.98	−0.74	L	H	L		2	1
19.0	19.1	0.0119	−0.20	0.04	0.17	0.29	−2.56*	−1.78	−1.52	−1.30	0.59	0.10	0.23	0.35	H	H	L		1	2
18.9	19.8	0.0137	0.51	0.22	0.34	0.44	−2.90*	−1.50	−1.27	−1.07	0.74	0.28	0.40	0.50	L	H	H		1	2
30.3	9.5	0.0110	−10.24	−11.26	−10.41	−9.94	−14.70	−16.47	−15.51	−14.60	−11.29	−12.06	−11.24	−10.75	I	I	I	3		
39.9	5.5	0.0123	−21.82	−24.57	−21.08	−19.01	−26.64	−40.2	−31.62	−27.65	−23.05	−25.31	−21.75	−19.73	I	L	I	2	1	
40.9	7.5	0.0107	−17.50*	−19.27	−17.81	−16.65	−23.90*	−27.52	−25.25	−23.59	−17.98*	−19.94	−18.55	−17.46	I	I	I	3		
39.4	8.2	0.0106	−17.88*	−17.50	−16.28	−15.26	−24.55*	−25.03	−23.26	−21.88	−18.76*	−18.26	−17.11	−16.17	H	I	H	1		2
40.4	11.3	0.0106	−14.58	−14.80	−14.08	−13.44	−23.15*	−21.17	−20.25	−19.46	−15.93	−15.75	−15.09	−14.52	I	H	H	1		2
40.8	12.8	0.0106	−13.46	−13.93	−13.33	−12.82	−19.88	−20.04	−19.30	−18.65	−14.30	−14.97	−14.43	−13.97	I	I	I	3		
39.1	15.0	0.0118	−12.09	−12.03	−11.55	−11.17	−16.93	−17.72	−17.17	−16.66	−13.13	−13.20	−12.81	−12.44	H	I	I	2		1
39.4	15.2	0.0125	−11.95	−12.06	−11.65	−11.26	−16.78	−17.82	−17.27	−16.78	−12.81	−13.26	−12.88	−12.53	I	I	I	3		
39.7	15.7	0.0128	−11.66	−11.95	−11.58	−11.22	−16.41	−17.71	−17.20	−16.73	−12.69	−13.18	−12.84	−12.57	I	L	I	2	1	
38.7	19.4	0.0119	−9.53*	−10.26	−9.99	−9.69	−13.74*	−15.47	−15.2	−14.75	−10.88*	−11.60	−11.36	−11.12	L	L	L		3	
39.1	20.0	0.0137	−10.86*	−10.30	−10.05	−9.78	−15.45*	−15.56	−15.18	−14.88	−10.88*	−11.67	−11.45	−11.22	H	I	L	1	1	1
57.8	15.0	0.0118	−16.78	−17.97	−17.55	−17.18	−21.41	−24.12	−23.62	−23.19	−18.34*	−18.93	−18.57	−18.26	L	L	I	1	2	
58.5	15.1	0.0125	−16.82	−18.11	−17.69	−17.33	−21.28	−24.32	−23.82	−23.39	−18.35*	−19.08	−18.72	−18.42	L	L	L		3	
58.2	19.8	0.0137	−16.04	−16.51	−16.27	−16.06	−20.04	−22.54	−22.27	−22.05	−18.06	−17.74	−17.55	−17.40	L	L	H		2	1
67.2	5.5	0.0123	−28.93	−41.66	−30.27	−26.65	−34.35	−97.43	−51.81	−39.15	−29.52	−42.89	−30.98	−27.33	I	L	I	2	1	
67.1	7.5	0.0107	−23.01	−26.05	−24.40	−23.21	−32.68	−36.77	−33.05	−30.84	−23.75	−26.70	−25.11	−23.99	L	I	L	1	2	
66.2	8.9	0.0106	−22.79	−23.71	−22.65	−21.80	−31.93	−31.81	−29.96	−28.63	−23.07	−24.43	−23.44	−22.66	I	H	I	2		1
65.5	10.5	0.0106	−19.22*	−22.01	−21.25	−20.61	−27.37	−28.99	−27.85	−26.98	−19.57*	−22.81	−22.12	−21.55	L	I	L	1	2	
68.1	12.3	0.0106	−19.36*	−21.17	−20.61	−20.12	−25.92	−27.61	−26.85	−26.24	−20.68*	−22.17	−21.67	−21.25	L	L	L		3	
67.3	16.0	0.0128	−18.02	−19.41	−19.05	−18.74	−23.69	−25.68	−25.17	−24.80	−19.95*	−20.61	−20.31	−20.05	L	L	L		3	
Total I															9	10	11			
Total H															5	5	4			
Total L															10	9	9			
Total count																		30	28	14

$\bar{U}$ is the effective neutral wind at 19.5 m; viscosity is in stokes for fresh water, H, L, and I indicate calculated value too high, calculated value too low, and measured value included in calculated inequality range, respectively.

*Backscatter decreases with increasing wind.

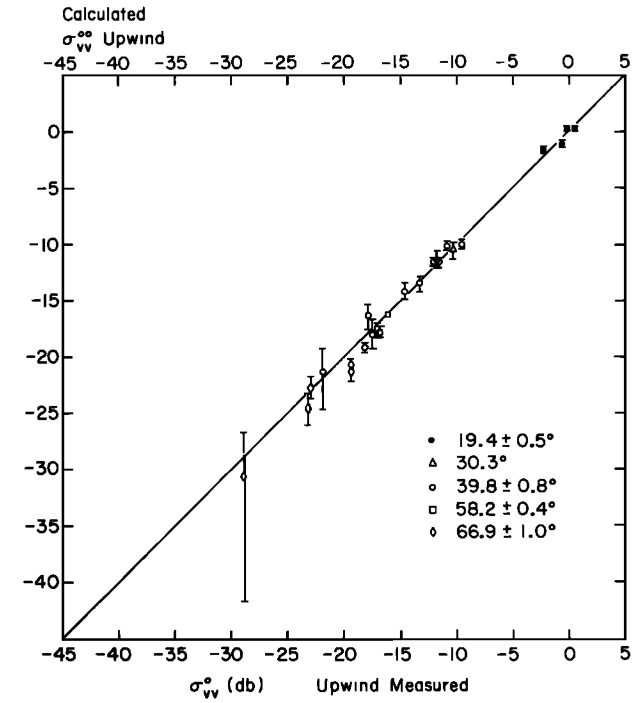

Fig. 14. Measured vertically polarized backscatter values in decibels for upwind (abscissa) versus values calculated from the model (ordinate) for the primary data set for five incidence angles as coded. The line of perfect agreement is shown. The error bars are for ± 1 m s^{-1} for the wind speed.

8.3. *The Effects of the Estimates of the Errors in the Calculation of σ^0 for the Primary Data Set*

Table IV of *Schroeder et al.* [1984] contains entries for upwind, cross wind, and downwind for the values of $\sigma_{error}{}^0$. To simplify notation, the symbol $\sigma^0 E$ will be used instead. These values were determined by the methods described in section 7. The approximately 1 standard deviation uncertainty in the measured backscatter is shown in Table 8, which closely parallels the format of Table 6. The calculated value is the backscatter from the model for the tabulated incidence angle and wind speed and for the appropriate water temperature. The value of $\sigma^0 E$ is from Table IV of Schroeder et al. The entries for $\sigma - \sigma^0 E$ and $\sigma + \sigma^0 E$ show the range of possible measured values for the backscatter computed from (36). The uncertainties in the measurement of the backscatter can be as much as ± 1.32 dB and as little as ± 0.24 dB.

As shown in the "measured versus calculated" columns, this range of uncertainty includes the value of the backscatter at upwind UP, cross wind CR, or downwind DN from the model for the values shown by an "I." If the value from the model is higher than the value from the fit to the measurement, an "H" is shown; if it is lower, an "L" is shown. Of the total, 29, or 40%, are within this range, 38% are too low, and 22% are too high.

For incidence angles of 30° or more, Table 8 confirms that upwind backscatter is higher than backscatter at downwind for vertical polarization by a slight amount. The range of values of $\pm \sigma^0 E$ for upwind and downwind overlap for only six circle flights in the full sample. Above 30°, backscatter at upwind is greater than backscatter at downwind for all 20 circle flights. The data near 20°, if anything, show the opposite, and the model calculations reflect this.

Figure 17 shows a portion of a graph of the measured backscatter values on the abscissa and the computed backscatter values on the ordinate for a few values from Tables 6 and 8. The data are plotted as rectangles with a point in the middle for the values computed from the measurements and from the model for the appropriate wind. The vertical extent shows the effect of a possible wind speed error of ± 1 m s^{-1}. The horizontal extent shows the range of $\pm \sigma^0 E$. Seven examples are shown.

In the first category, there is some wind speed within 1 m s^{-1} of the reported value that would produce the measured backscatter with the model. Or conversely, the backscatter computed from the reported wind differs by a relatively small amount, usually, from the measured value.

In the second category, the possible errors in the measured backscatter have a range that encloses the backscatter computed for the reported wind. If the values of $\sigma^0 E$ at upwind, downwind, and cross wind were completely independent of each other and an arbitrary adjustment could be made for each measured value, then the backscatter computed for the measured wind from the model would agree exactly with the corrected measured value. The same adjustment in $\sigma^0 E$ for an entire circle flight would probably be a more realistic way to proceed.

For the third category, both $\bar{U} \pm 1$ and $\sigma^0 \pm \sigma^0 E$ intersect the 45° line. For two more categories, neither $\bar{U} \pm 1$ nor $\sigma^0 \pm \sigma^0 E$ intersects the 45° line, but a corner of the rectangle lies within the 45° line. These are designated by A for above the 45° line and B for below the 45° line. For the last two, no part of the rectangle reaches the 45° line as shown by H and L.

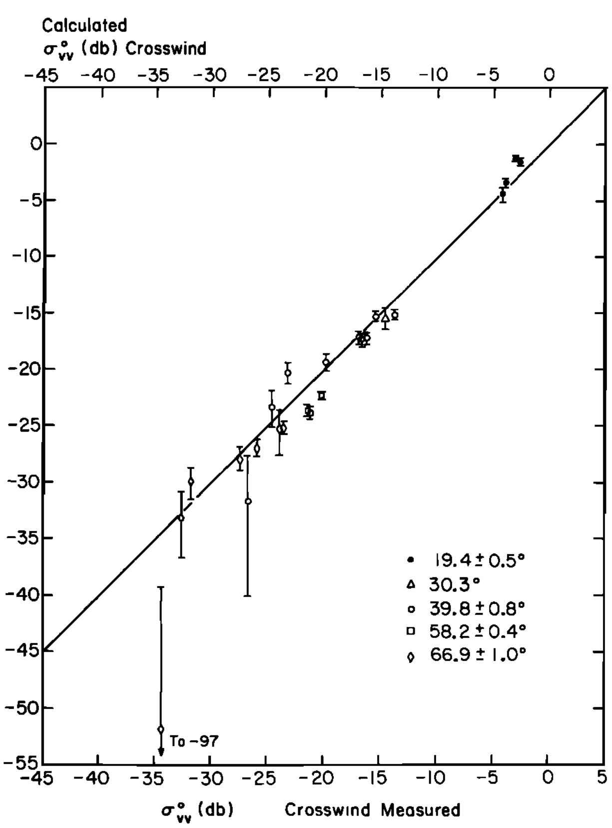

Fig. 15. Same as Figure 14 except for cross wind.

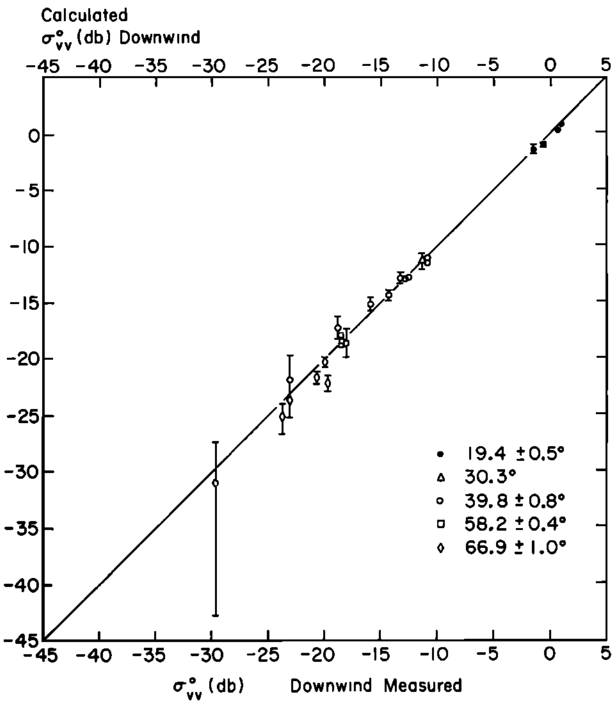

Fig. 16. Same as Figure 14 except for downwind.

Combined results from Tables 6 and 8 are summarized in Table 9. The hits from Table 6 are shown in the first grouping. Those from Table 8 are in the second grouping. Those that satisfy both criteria are in the third grouping. Those in either are in the fourth. The inequalities in the two tables can enclose a common range of backscatter values and yet not fall in either of the first two categories. A corner of the appropriate rectangle is then categorized by A or B for above or below the 45° line as shown in Figure 17.

If the 14 corners (Table 9) are counted, improvements are made for incidence angles near 20° even for quite small values of $\sigma^0 E$. Ten out of 12 are close enough to qualify even for that part of the model where backscatter increases less rapidly with wind speed. For incidence angles near 67°, 6 out of 18 new data points qualify because of the large values of $\sigma^0 E$. A total of 12 out of 18 qualify for the 67° incidence angle. As totals, 73% of the measured values agree well with the model for these criteria; the model is low for 17% of the comparison and high for 10%.

There are data points in the out category of 19 points that lie fairly close to the theoretical curves compared with others that are quite far away. This can be shown by looking for those points that fall within $\sigma^0 \pm 2\sigma^0 E$ and $\bar{U} \pm 1$, where $\sigma^0 - 2\sigma^0 E$ to $\sigma^0 - \sigma^0 E$ would enclose the value for $\bar{U} + 1$ and $\sigma^0 + \sigma^0 E$ to $\sigma^0 + 2\sigma^0 E$ would enclose the value for $\bar{U} - 1$. These fairly close points are shown by asterisks and daggers with the appropriate footnote. Nine points qualify, so that only 10 points out of 72 are far out of line.

For vertical polarization, the actual minimum near 90° is given in Table 8 under the column "minimum cross." This change would have no effect on the scoring.

There are additional ways to interpret these results by means of plotting the data in a different form to be described in the next subsection. Conclusions on the fit between the model and the data will be given after results for horizontal polarization are described.

8.4. *Backscatter Versus Wind Speed, Predicted and Measured*

Figures 18*a* through 18*f* are in sets of two for upwind, cross wind, and downwind. The first of each set is for incidence angles of 30.2° and 39.7°, and the second is for incidence angles of 49.3°, 58.2°, and 66.9°. The curves for 58.2° and 66.9° crowd together for low winds because of the difference in water temperature. Except for 49.3°, these are the average incidence angles for the groups in the primary data set. The heavy solid curves show the theoretical curves for backscatter in decibels versus the logarithm of the wind speed for the average sea surface temperatures for each group, which are 10.7°, 14.1°, 18°, 11.2°, and 15.6°C, respectively.

The coded symbols show measured values of the vertically polarized backscatter versus reported wind speeds for the primary and supplementary data sets. The symbols are solid for the primary data and open for the supplementary data. Since both the incidence angle and the temperature for each data point were different from the appropriate average, the correction for the primary data set needs to be shown. These consist of arcs of curves shown only for the primary data set parallel

TABLE 7. Bias (Computed-Observed), rms Difference, and Standard Deviation in Decibels, Stratified by Upwind, Cross Wind, Downwind, and Incidence Angle for Vertical Polarization

		Upwind			Cross Wind			Downwind			All Directions			
$\bar{\theta}$, deg	N	Bias	rms	s.d.	Bias	rms	s.d.	Bias	rms	s.d.	N	Bias	rms	s.d.
19.4	4	+0.10	0.39	0.49	+0.79	1.00	0.71	−0.23	0.32	0.26	12	+0.20	0.65	0.65
30.4	1	−0.17	···	···	−0.81	···	···	+0.05	···	···	3	−0.29	0.48	0.47
39.8	10	+0.39	0.69	0.60	−0.43	2.00	2.06	+0.21	0.78	0.79	30	+0.06	1.30	1.32
58.2	3	−0.62	0.68	0.34	−2.327	2.332	0.19	+0.51	1.42	1.62	9	−0.94	1.46	1.18
66.9	6	−1.15	1.32	0.71	−3.13	7.21	7.12	−1.18	1.40	0.83	18	−1.82	4.31	4.02
Less outrider	5				−0.29	1.29	1.40				17	−0.91	1.34	1.01
All angles	24	−0.19	0.85	0.85	−1.15	3.94	3.85	−0.24	0.91	0.90				
Less outrider	23				−0.44	1.72	1.70							
All angles, all directions											72	−0.52	2.18	2.13
Less outrider											71	−0.28	1.22	1.20

TABLE 8. Comparison of Estimated Measurement Error

			Upwind					Cross Wind				
					Measured					Measured		
M/F/L/R	$\bar{\theta}$, deg	$\bar{U}$, m s^{-1}	Calculated σ^0	$\sigma^0 E$	$\sigma^0 - \sigma^0 E$	σ^0	$\sigma^0 + \sigma^0 E$	Calculated σ^0	$\sigma^0 E$	$\sigma^0 - \sigma^0 E$	σ^0	$\sigma^0 + \sigma^0 E$
318/17/4/1	19.8	13.5	−1.57	0.24	−2.36	−2.12	−1.88	−4.39	0.26	−4.60	−4.34	−4.08
335/5/4/1	19.9	15.5	−1.02	0.27	−0.93	−0.66	−0.39	−3.47	0.27	−4.28	−4.01	−3.74
335/4B/4/1	19.0	19.1	−0.17	0.27	−0.47	−0.20	+0.07	−1.52	0.26	−2.82	−2.56	−2.30
335/4A/4/1	18.9	19.8	0.34	0.48	0.03	0.51	0.99	−1.27	0.26	−3.16	−2.90	−2.64
318/24/4/1	30.3	9.5	−10.41	0.34	−10.58	−10.24	−9.90	−15.51	0.35	−15.05	−14.70	−14.35
318/14/4/7	39.9	5.5	−21.08	0.40	−22.22	−21.82	−21.42	−31.62	0.85	−27.49	−26.64	−25.79
318/19/4/13	40.9	7.5	−17.81	0.34	−17.84	−17.50	−17.16	−25.25	0.45	−24.35	−23.90	−23.45
318/16/4/9	39.4	8.2	−16.28	0.34	−18.22	−17.88	−17.54	−23.26	0.52	−25.07	−24.55	−24.03
318/18/4/6	40.4	11.3	−14.08	0.52	−15.10	−14.58	−14.06	−20.25	0.41	−23.56	−23.15	−22.74
318/17/4/8	40.8	12.8	−13.23	0.36	−13.82	−13.46	−13.10	−19.30	0.36	−20.24	−19.88	−19.52
335/6/4/9	39.1	15.0	−11.55	0.37	−12.46	−12.09	−11.72	−17.17	0.34	−17.27	−16.93	−16.57
335/5/4/9	39.4	15.2	−11.65	0.36	−12.31	−11.95	−11.59	−17.27	0.36	−17.14	−16.78	−16.42
353/11/4/11	39.7	15.7	−11.58	0.35	−12.01	−11.66	−11.31	−17.20	0.49	−16.90	−16.41	−15.92
335/4B/4/10	38.7	19.4	−9.99	0.38	−9.91	−9.53	−9.15	−15.20	0.38	−14.12	−13.74	−13.36
335/4A/4/9	39.1	20.0	−10.05	0.34	−11.20	−10.86	−10.52	−15.18	0.36	−15.81	−15.45	−15.09
335/6/4/13	57.8	15.0	−17.55	0.36	−17.14	−16.78	−16.42	−23.62	0.42	−21.83	−21.41	−20.99
335/5/4/17	58.5	15.1	−17.69	0.66	−17.48	−16.82	−16.16	−23.82	0.46	−21.74	−21.28	−20.82
335/4A/4/17	58.2	19.8	−16.27	0.36	−16.4	−16.04	−15.68	−22.27	0.41	−20.45	−20.04	−19.63
318/14/4/12	67.2	5.5	−30.27	1.11	−30.04	−28.93	−27.82	−51.81	1.22	−35.57	−34.35	−33.13
318/19/4/17	67.1	7.5	−24.40	0.50	−23.51	−23.01	−22.51	−33.05	1.32	−34.00	−32.68	−31.36
318/16/4/14	66.2	8.9	−22.65	0.44	−23.23	−22.79	−22.35	−29.96	1.14	−33.07	−31.93	−30.79
318/18/4/11	65.5	10.5	−21.25	0.41	−19.63	−19.22	−18.81	−27.85	1.13	−28.50	−27.37	−26.24
318/17/4/12	68.1	12.3	−20.61	0.41	−19.77	−19.36	−18.95	−26.85	1.13	−26.95	−25.82	−24.69
353/11/4/1	67.3	16.0	−19.05	1.16	−19.18	−18.02	−16.86	−25.17	1.09	−24.78	−23.69	−22.60
Total I												
Total H												
Total L												
Total count												

H, L, and I indicate calculated value too high, calculated value too low, and measured value included in calculated inequality range, respectively. Backscatter values are in decibels.

to the average curve that show that portion of the curve for the reported incidence angle and water temperature that would go with the data point. If not shown, this correction curve essentially coincides with the average curve. For some primary points, the range for ± 1 m s^{-1} is also shown by bars.

The vertical bounds for each point show the ± 1 $\sigma^0 E$ values and describe the uncertainty in the measurement of the backscatter. The range of uncertainty can be as much as 2 dB.

For example, the corrected curve for the 39.7° theoretical curve in Figure 18*a* for a wind of 7.5 m s^{-1} is computed for an incidence angle of 40.9° and a temperature of 17.4°C. It lies several tenths of a decibel below the curve for the average, and it extends from 6.5 to 8.5 m s^{-1} as found from Table 6. The effect of the error bars on the measured value of $\sigma^0 E$ is small compared to the possible wind speed error. Each primary data point should be shifted vertically so that the arc coincides with the average curve. This step for some points provides improved agreement. For others such as the three points near 15 m s^{-1} in Figure 18*a*, the points are moved away from the average curve by a slight amount. The correction for 19.4 and 20.0 m s^{-1} would reinforce the decrease in sensitivity for higher winds. For high winds, the error bars for $\sigma^0 E$ are comparable to those for a 1 m s^{-1} speed error. If a primary data point can be shifted left or right or up or down so as to intersect the arc associated with it, then that point would fall within either the ± 1 m s^{-1} criterion of Table 6 or the $\pm \sigma^0 E$ criterion of Table 8. Others are the corner points in Table 9. Several points barely miss when this is done. Other points are still too far away for these shifts to help. The solid diamonds for Figure 18*d* belong to the middle theoretical curve.

Supplementary data points are shown by open symbols. The error bars are shown for each point. The four lowest wind speed points in Figure 18*a* differ by over 4 dB. Yet slight changes in the wind speed and the fact that the water temperature was a degree or so higher would result in their fitting the theory. The same is true for Figure 18*e* at downwind but not for Figure 18*c* at cross wind.

Table 10 contains the values of $\sigma^0 E$ for the supplementary data set for incidence angles of 29.4° and higher. The generally larger values of $\sigma^0 E$ reflect the smaller values of R^2 and the difficulty of making measurements for light winds for an incidence angle near 40°. The use of the minimum near cross wind would have little effect. Table 11 is similar to Table 9 except that the criteria have been determined from Figures 18*a* to 18*f* along with a judgment of the effect of temperature and variations in incidence angle. More than half are sufficiently close to the curves of the model.

Schroeder et al. [1984] also give the power law fits for

With Calculated Backscatter for $\bar{U}$ for Vertical Polarization

Downwind						Measured Versus Calculated			Count		
		Measured									
Calculated σ^0	σ^0E	$\sigma^0 - \sigma^0E$	σ^0	$\sigma^0 + \sigma^0E$	Minimum Cross	UP	CR	DN	I	L	H
−1.52	0.28	−1.73	−1.45	−1.17		H	I	I	2		1
−0.98	0.24	−0.81	−0.57	−0.33		L	H	L		2	1
−0.23	0.46	0.13	0.59	+1.05		I	H	I	2		1
−0.40	0.46	0.28	0.74	+1.20		I	H	I	2		1
−11.24	0.34	−11.63	−11.29	−10.95		I	L	I	2	1	
−21.75	0.41	−23.46	−23.05	−22.64		H	L	H		1	2
−18.55	0.38	−18.36	−17.98	−17.60		I	L	L	1	2	
−17.11	0.38	−19.14	−18.76	−18.38		H	H	H			3
−15.09	0.35	−16.28	−15.93	−15.58		I	H	H	1		2
−14.43	0.36	−14.66	−14.30	−13.94		I	H	I	2		1
−12.81	0.37	−13.50	−13.13	−12.76		H	I	I	2		1
−12.88	0.39	−13.20	−12.81	−12.42		I	L	I	2	1	
−12.84	0.38	−13.07	−12.69	−12.31		I	L	I	2	1	
−11.36	0.31	−11.19	−10.88	−10.57		L	L	L		3	
−11.45	0.36	−11.24	−10.88	−10.52		H	I	L	1	1	1
−18.57	0.37	−18.61	−18.24	−17.87	−21.56	L	L	I	1	2	
−18.72	0.52	−18.87	−18.35	−17.83	−21.42	L	L	I	1	2	
−17.55	0.39	−18.45	−18.06	−17.67	−20.22	I	L	H	1	1	1
−30.98	1.14	−30.16	−29.52	−28.38	−34.42	L	L	L		3	
−25.11	0.94	−24.69	−23.75	−22.81	−32.76	L	I	L	1	2	
−23.44	0.90	−23.97	−23.07	−22.17	−31.95	I	H	I	2		1
−22.12	0.45	−20.02	−19.57	−19.12	−27.39	L	I	L	1	2	
−21.67	0.45	−21.13	−20.68	−20.23	−26.05	L	I	L	1	2	
−20.31	1.21	−21.16	−19.95	−18.74	−23.93	I	L	I	2	1	
						11	6	12			
						5	7	4			
						8	11	8			
									29	27	16

upwind, downwind, and cross wind for both vertical and horizontal polarization in their Figure 4. All data are used, including those circle flights not contained in our Tables 1, 2, and 3 along with all level flights at upwind, downwind, and cross wind from earlier missions. Though not strictly comparable, the power law fits for 30°, 40°, 50°, and 60° are shown on the appropriate figures.

For upwind, the curve for the model for 39.7° in Fig. 18*a* is a better fit to the data that were used than the power law. For cross wind (Figure 18*c*) the fit is better at high winds. The behavior of the model for light winds is more reasonable. Downwind (Figure 18*e*) is perhaps the best example where the model crosses the power law curve at about 5.5 m s^{-1} and lies above it until a wind of about 16 m s^{-1}. The power law misses the light winds, and the correction for the two highest winds puts the data points as close to the theoretical curve as to the power law.

The upwind, downwind, and cross-wind results have been treated as independent. Although changes in the measured backscatter and the reported wind within their error bounds could be made that would in many instances provide perfect agreement between the model and the data, the changes need not necessarily be in the same direction for all three data points for the same circle flight. It is possible that a small change in the wind speed and a small adjustment in the possible bias for the backscatter as in (54) could minimize the differences that have been found. If the three data points all lie on the same side of the theoretical curves in Figures 18*a* to 18*f* and consequently on the same side of the 45° line in Figure 17, such an adjustment could be made. From Figure 17 the shorter the distance of the three points that would be involved from the 45° line the smaller the change would need to be in wind speed and measured backscatter.

A comparison of the rows of the six values for H, I, and L for a given circle flight in Tables 6 and 8 show when a single change in the bias and a single change in the wind speed would improve the fit between the model and the data as adjusted according to these rules for the best 24 circle flights. For incidence angles near 67°, lowering the value of the measured backscatter, and increasing the wind speed, except for the 8.9 m s^{-1} wind would improve the fit.

For incidence angles near 58°, the backscatter measurements could be biased high and the fit improved for winds of 15.0 and 15.1 m s^{-1}. For these six, for example, the combinations of Ls and Is make improvements possible. Mixtures of Hs, Ls and Is would require, at least, using different signs for the bias. The additional effect of $\Delta\sigma^0/\sigma^0$, which is an estimate of the normalized standard deviation of the data relative to

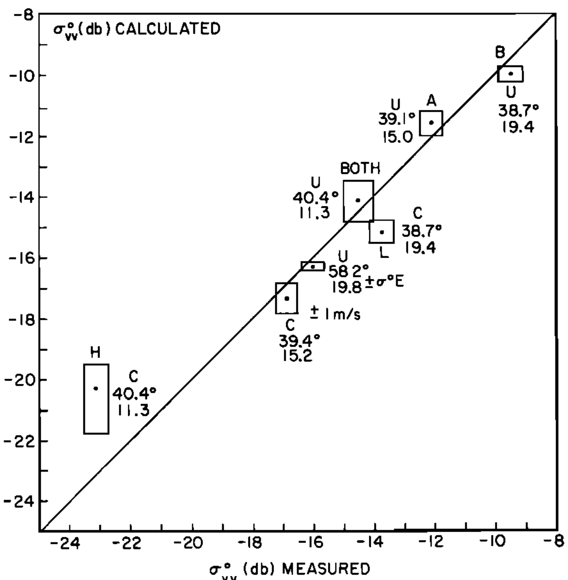

Fig. 17. Examples of the seven categories of goodness of fit described in the text. The point is identified by upwind (U) and cross wind (C) and by an incidence angle and wind speed. The top and bottom of each rectangle represent backscatter calculated for $\bar{U}+1$ and $\bar{U}-1$, the vertical sides represent $\sigma^0 + \sigma^0 E$ and $\sigma^0 - \sigma^0 E$ from the data, and the dot is the measured value from the data (abscissa) plotted against the calculated value (ordinate). (See text for details.)

the computed average of the backscatter values, might have produced this kind of result for some of the data.

8.5. *Upwind/Cross-Wind and Upwind/Downwind Ratios*

Although the absolute level of the model as a function of χ might differ from the measured values as a function of χ, the overall shapes may be similar. How well the model agrees with the data with reference to the differences between upwind and cross wind and between upwind and downwind is thus of interest, particularly with regard to the determination of wind direction. In antilog form the needed ratios for the data can be written as

$$\frac{\sigma_{VV}{}^0(\mathrm{UP})}{\sigma_{VV}{}^0(\mathrm{CR})} = \frac{A_0 + A_1 + A_2}{A_0 - A_2} \tag{57}$$

$$\frac{\sigma_{VV}{}^0(\mathrm{UP})}{\sigma_{VV}{}^0(\mathrm{DN})} = \frac{A_0 + A_1 + A_2}{A_0 - A_1 + A_2} \tag{58}$$

When expressed in decibels, (57) becomes, for example,

$$\left(\frac{\sigma_{VV}{}^0(\mathrm{UP})}{\sigma_{VV}{}^0(\mathrm{CR})}\right)_{\mathrm{dB}} = \sigma_{VV}{}^0(\mathrm{UP})_{\mathrm{dB}} - \sigma_{VV}{}^0(\mathrm{CR})_{\mathrm{dB}} \tag{59}$$

A notation such as the left-hand side of (59) is used in the figures to follow to emphasize that should the right-hand side of (59) equal 10, the upwind backscatter would be 10 times stronger than the cross-wind backscatter.

Ratios computed in this way have a large range of uncertainty because of the effect of two values of $\sigma^0 E$ from Table 8 associated with each computation. For example, the following equation can be obtained:

$$\begin{aligned}\left(\frac{\sigma_{VV}{}^0(\mathrm{UP})}{\sigma_{VV}{}^0(\mathrm{CR})}\right)_{\mathrm{dB}} &= (\sigma_{VV}{}^0(\mathrm{UP})_{\mathrm{dB}} \pm \sigma_1{}^0E) - (\sigma_{VV}{}^0(\mathrm{CR})_{\mathrm{dB}} \pm \sigma_2{}^0E)\\ &= \sigma_{VV}{}^0(\mathrm{UP})_{\mathrm{dB}} - \sigma_{VV}{}^0(\mathrm{CR})_{\mathrm{dB}} \pm (\sigma_1{}^0E + \sigma_2{}^0E)\end{aligned} \tag{60}$$

Equation (60) is a worst case error analysis, since it assumes that the numerator of the left-hand side (60) is increased by one error estimate and the denominator is decreased by the other error estimate, or conversely. Strictly done, it would be necessary to compute the standard deviations of the antilog and use the square root of the sum of the squares of these values to find the error bars.

The error bars for the measured upwind/cross-wind ratios were computed according to (60) with a similar equation for upwind/downwind. For the model values, the corresponding ratios were found from the computed values for $\bar{U}$, $\bar{U}+1$, and $\bar{U}-1$.

For upwind/cross-wind the result is Figure 19, where only some of the error bars are shown so as not to unduly complicate the figure. Figure 20 shows the corresponding results for upwind/downwind. The scoring method used in Table 9 was then applied to the data.

For upwind/crosswind, four measured values were within the range of calculated values for $\bar{U} \pm 1$. These same four plus three others were within the horizontal scatter as a result of the values of $\sigma^0 E$ for the calculated value at $\bar{U}$. Seven more were in the corners as defined previously. Three out of four miss for incidence angles near 20°. For 40°, those with winds of 5.5, 11.3 and 19.4 m s^{-1} miss. For 57°, all miss, and for 67°, the data for 5.5 m s^{-1} miss.

For upwind/downwind, the uncertainty in wind speed produces only a small effect, but the uncertainty due to the values of $\sigma^0 E$ is large. The values for an incidence angle of 67.1° and a wind speed of 7.5 m s^{-1} meet the $\bar{U} \pm 1$ criterion. Only two miss both the $\sigma^0 E$ and the corner criteria. These are the value for an incidence angle of 19.8° and a wind of 13.5 m s^{-1}, as shown by an M, and an incidence angle of 39.1° and a wind of 20 m s^{-1}. Only the full range of scatter at 20° is shown.

8.6. *Effects at Light Winds*

One of the difficulties with power law models is the large scatter of the backscatter values for a given surface wind speed for light winds as illustrated by *Schroeder et al.* [1982*b*] in their Figures 5, 6, and 7, which combine the Gulf of Alaska Seasat Experiment (GOASEX) and JASIN data. The scatter is substantial for all wind speeds, but for winds below 5 m s^{-1} at a 40° incidence angle, the data scatter by 10 to 20 dB. A partial explanation is given by *Schroeder et al.* [1982*b*] based on the hypothesis that the comparison data wind speeds can be in error by ± 2 to 3 m s^{-1}. Our model for a 40° incidence angle shows that light winds under 2.4 to 3.6 m s^{-1} ought not to have had any measurable backscatter at all and that the observed backscatter may well have been simply noise. Very small changes in either the incidence angle or the wind speed and 5° or 10° changes in water temperature can produce changes in backscatter of 20 dB. The scatter in the backscatter values for light winds is thus also the result of these small changes that result in large changes in the backscatter. The scatter for the SASS data may actually be larger than was reported because data for which an estimate of the ratio of the

TABLE 9. Combined Effect of Wind Speed and Backscatter Bias Errors for Vertical Polarization

			In $\bar{U} \pm 1$			In $\sigma^0 \pm \sigma^0 E$			In Both			In Either			In Corner or Either			Out			Count		
M/F/L/R	$\bar{\theta}$, deg	$\bar{U}$, m s^{-1}	UP	CR	DN	UP	CR	DN	UP	CR	DN	UP	CR	DN	UP	CR	DN	UP	CR	DN	I	L	H
318/17/4/1	19.8	13.5		I	I		I	I		I	I		I	I	A	I	I				3		
335/5/4/1	19.9	15.5													B	A	B				3		
335/4B/4/1	19.0	19.1				I		I				I		I	I		I		H		2		1
335/4A/4/1	18.9	19.8				I		I				I		I	I		I		H		2		1
318/24/4/1	30.3	9.5	I	I	I	I		I	I		I	I	I	I	I	I	I				3		
318/14/4/7	39.9	5.5	I		I							I		I	I		I		L*		2	1	
318/19/4/13	40.9	7.5	I	I	I	I			I			I	I	I	I	I	I				3		
318/16/4/9	39.4	8.2		I									I			I		H†		H†	1		2
318/18/4/6	40.4	11.3	I			I			I			I			I		A		H		2		1
318/17/4/8	40.8	12.8	I	I	I	I		I	I		I	I	I	I	I	I	I				3		
335/6/4/9	39.1	15.0		I	I		I	I		I	I		I	I	A	I	I				3		
335/5/4/9	39.4	15.2	I	I	I	I		I	I		I	I	I	I	I	I	I				3		
353/11/4/11	39.7	15.7	I		I	I		I	I		I	I		I	I	B	I				3		
335/4B/4/10	38.7	19.4													B		B		L		2	1	
335/4A/4/9	39.1	20.0		I			I			I			I			I	B	H†			2		1
335/6/4/13	57.8	15.0			I			I			I			I			I	L*	L*		1	2	
335/5/4/17	58.5	15.1						I						I	B		I		L		2	1	
335/4A/4/17	58.2	19.8				I						I			I				L	H†	1	1	1
318/14/4/12	67.2	5.5	I		I							I		I	I		I		L		2	1	
318/19/4/17	67.1	7.5		I			I			I			I		B	I	B				3		
318/16/4/14	66.2	8.9	I		I	I		I	I		I	I		I	I	A	I				3		
318/18/4/11	65.5	10.5		I			I			I			I			I		L		L	1	2	
318/17/4/12	68.1	12.3					I						I			I		L		L*	1	2	
353/11/4/1	67.3	16.0				I		I				I		I	I		I		L*		2	1	
Count			9	10	11	11	6	12	7	5	8	13	11	15	19	14	20	2H 3L	3H 7L	2H 2L	53	12	7
Sum				30			29			20			39			53			19‡				

A denotes high σ^0 and low $\bar{U}$; B denotes low σ^0 and high $\bar{U}$.

*In $\sigma^0 - 2\sigma^0 E$, $\bar{U} + 1$.

†In $\sigma^0 + 2\sigma^0 E$, $\bar{U} - 1$.

‡The 10 data points not marked with an asterisk or dagger are far from the theoretical curve. There are 62 points close to agreement if A's and B's are counted; seven points are too low, and three are too high.

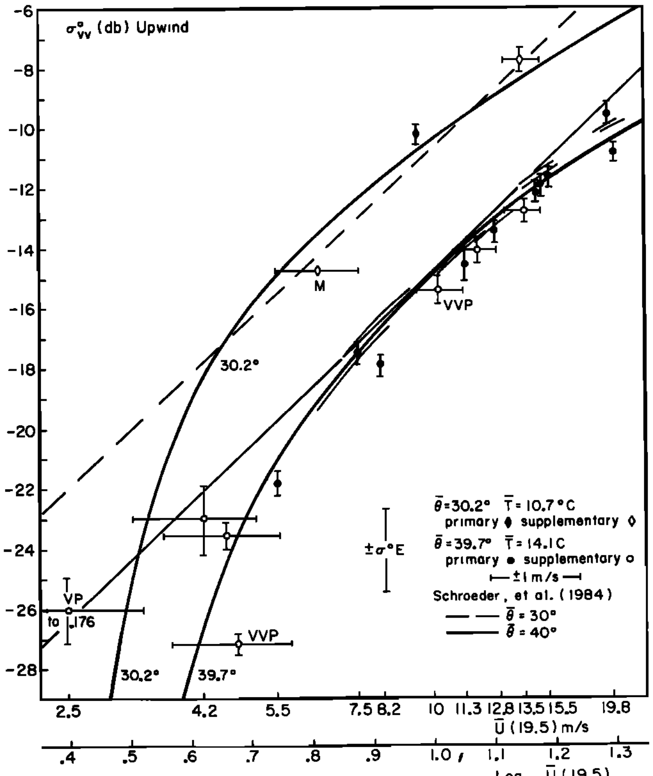

Fig. 18a

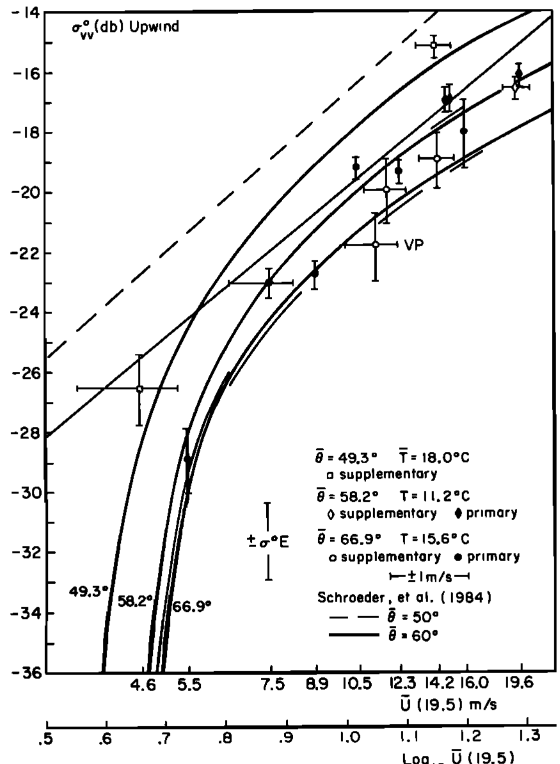

Fig. 18b

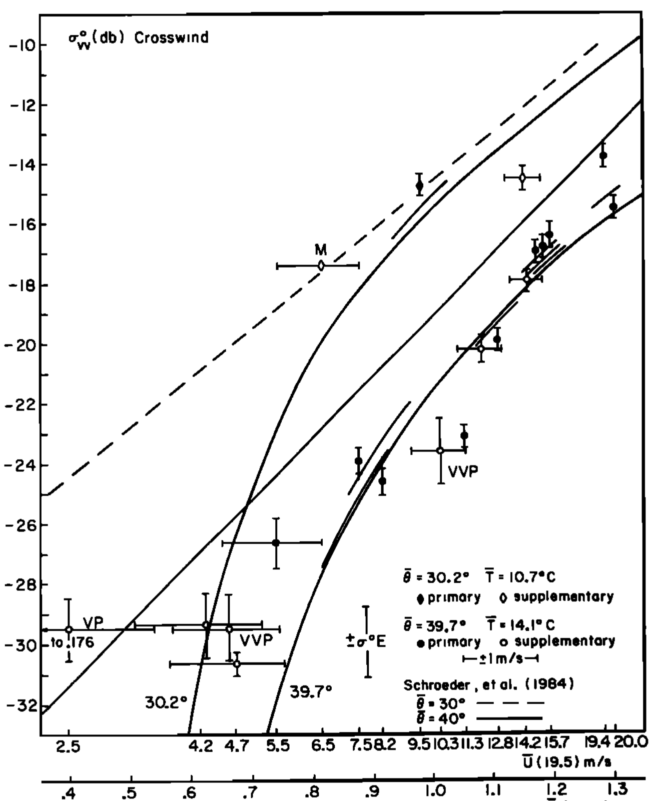

Fig. 18c

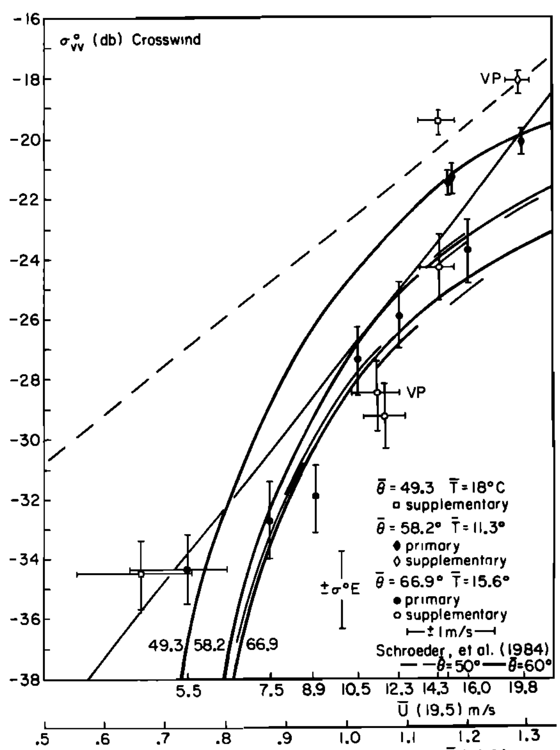

Fig. 18d

Fig. 18. (*a*) Model values for vertically polarized backscatter at upwind for an incidence angle of 30.2° and a water temperature of 10.7°C and for an incidence angle of 39.7° and a water temperature of 14.1°C. The plotted points are from the primary and supplementary data sets as coded. The vertical bars are error bounds on the backscatter, and the horizontal bars are error bounds on the wind speed. The power laws from *Schroeder et al.* [1984] are also shown. (See text.) (*b*) Model values for vertically polarized backscatter at upwind for an incidence angle of 49.3° and a water temperature of 18°C, an incidence angle of 58.2° and a water temperature of 11.2°C, and an incidence angle of 66.9° and a water temperature of 15.6°C. The plotted points are from the primary and supplementary data sets as coded. The vertical bars are error bounds on the backscatter, and the horizontal bars are error bounds on the wind speed. The power laws from *Schroeder et al.* [1984] are also shown. (See text) (*c*) Same as Figure 18*a* except at cross wind. (*d*) Same as Figure 18*b* except at cross wind. (*e*) Same as Figure 18*a* except at downwind. (*f*) Same as Figure 18*b* except at downwind

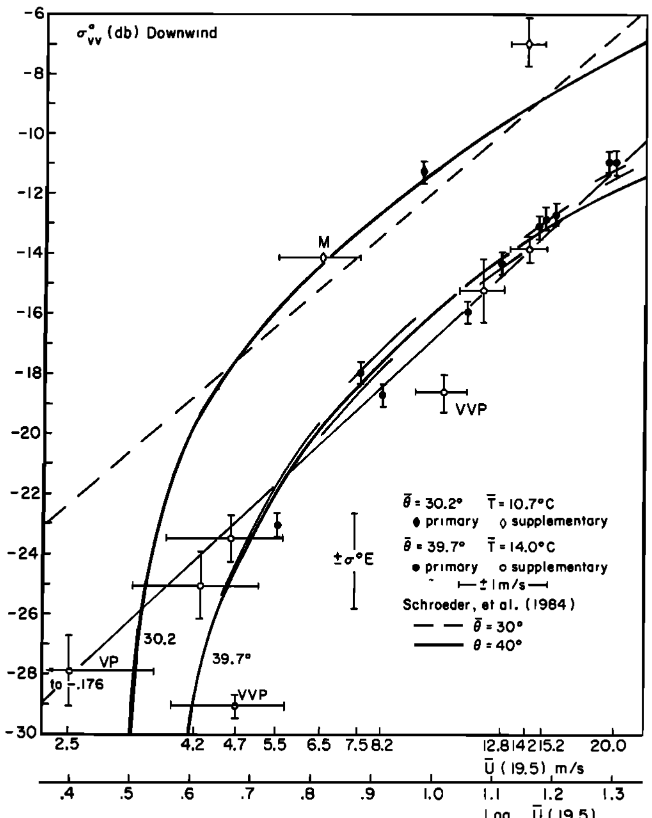

Fig. 18*e*

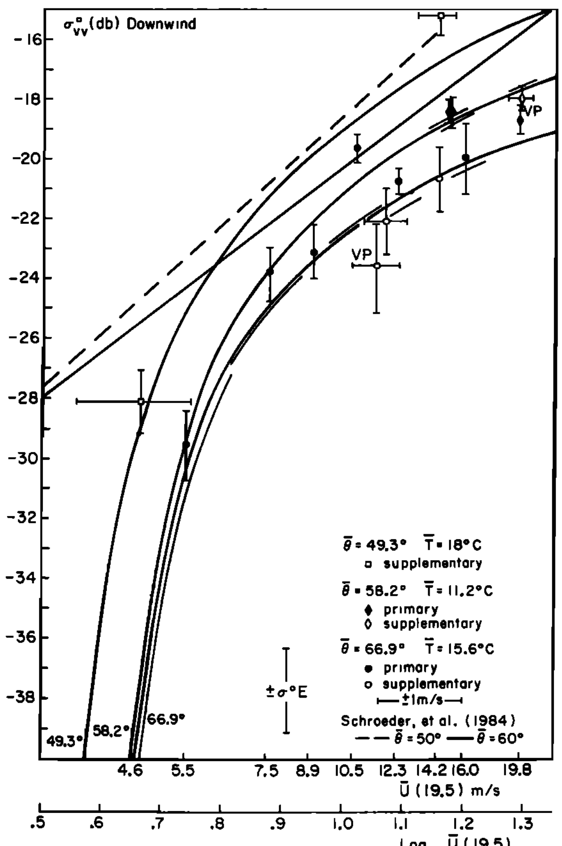

Fig. 18*f*

Fig. 18. (continued)

standard deviation to the mean exceeded 1 and negative estimates of the received power were probably discarded when these figures were prepared [*Pierson et al.*, 1986].

8.7. *Low Incidence Angles*

For a 19.4° incidence angle and vertical polarization, Figure 21 shows the theoretical curves for upwind, downwind, and cross wind. The upwind and downwind curves are virtually identical. The upwind, downwind, and cross-wind measured backscatter values are shown by solid coded symbols for the four primary data set measurements. They come fairly close to the theoretical curves. The supplementary values computed from Table 3 are shown by the open symbols. They fit, more or less, for winds above 7 m s^{-1}, but for lighter winds the disagreement between theory and measurement is very large. For winds under 7 m s^{-1}, upwind is sometimes larger and at other times smaller than downwind. The range from the largest value to the cross-wind value can be under 1 dB and as

TABLE 10. Backscatter Values and Bias Errors for the Supplementary Data Set

$\bar\theta$, deg	$\bar{U}$, m s^{-1}	Upwind $\sigma_{VV}{}^0$	Upwind σ^0E	Cross Wind $\sigma_{VV}{}^0$	Cross Wind σ^0E	Minimum $\sigma_{VV}{}^0$	Minimum Difference	Downwind $\sigma_{VV}{}^0$	Downwind σ^0E
31.0	6.5	−14.78	···	−17.33	···	−17.36	−0.03	−14.09	···
29.4	14.2	−7.67	0.47	−14.47	0.37	−14.48	−0.01	−6.93	0.77
38.9	2.5	−26.04	1.13	−29.47	1.07	−29.67	−0.20	−27.92	1.13
40.1	4.2	−23.05	1.13	−29.36	1.08	−29.64	−0.28	−25.06	1.13
40.6	4.6	−23.53	0.46	−29.45	1.10	−29.45	0	−23.53	0.76
39.4	4.7	−27.19	0.36	−30.66	0.39	−30.86	−0.20	−29.07	0.38
39.7	10.3	−15.40	0.43	−23.60	1.07	−24.54	−0.94	−18.64	0.59
40.5	12.0	−14.14	0.37	−20.20	0.46	−20.28	−0.08	−15.18	1.09
39.4	14.3	−12.77	0.38	−17.90	0.38	−17.98	−0.08	−13.84	0.54
50.3	4.6	−26.54	1.19	−34.53	1.19	−34.78	−0.25	−28.06	1.06
48.3	14.2	−15.16	0.37	−19.50	0.37	−19.50	0	−19.38	0.37
58.0	19.6	−16.60	0.36	−18.14	0.36	−18.30	−0.16	−17.90	0.36
67.3	11.3	−21.81	1.14	−28.54	1.14	−28.76	−0.22	−23.56	1.14
67.7	11.7	−19.95	1.08	−29.24	1.08	−29.75	−0.51	−22.01	1.11
67.1	14.3	−18.87	1.09	−24.23	1.09	−24.41	−0.18	−20.60	1.14

Backscatter values are in decibels.

TABLE 11. Combined Effect of Wind Speed and Backscatter Bias Errors for the Supplementary Data for Vertical Polarization

			In $\bar{U} \pm 1$			In $\sigma^0 \pm \sigma^0 E$			In Both			In Either			In Corner or Either			Out			Count		
M/F/L/R	$\bar{\theta}$, deg	$\bar{U}$, m s^{-1}	UP	CR	DN	UP	CR	DN	UP	CR	DN	UP	CR	DN	UP	CR	DN	UP	CR	DN	I	L	H
230/20/4/2	31.0	6.5	I		I	...	...	...				I		I	I		I		H		2		1
335/3/4/1	29.4	14.2																L	L	L		3	
353/20/4/26	38.9	2.5																L	L	L		3	
353/15/4/16	40.1	4.2	I		I							I		I	I		I		L		2	1	
318/13/4/9	40.6	4.6	I		I							I		I	I		I		L		2	1	
353/21/4/12	39.4	4.7	I		I							I		I	I		I		L		2	1	
353/9/4/16	39.7	10.3				I						I			I				L	L	1	2	
353/13/4/20	40.5	12.0		I	I	I	I	I		I	I	I	I	I	I	I	I				3		
353/14/4/11	39.4	14.3	I	I	I	I	I	I	I	I	I	I	I	I	I	I	I				3		
318/13/4/11	50.3	4.6	I		I			I			I	I		I	I		I		L		2	1	
335/3/4/6	48.3	14.2																L	L	L		3	
335/4B/4/17	58.0	19.6	I			I		I	I			I		I	I		I		L		2	1	
353/9/4/6	67.3	11.3				I						I			I		B		H		2		1
353/13/4/16	67.7	11.7			I	I		I			I	I		I	I		I		H		2		1
353/14/4/1	67.1	14.3			I	I		I			I	I		I	I		I		L		2	1	
Count			7	2	9	7	2	6	2	2	5	12	2	10	12	2	11	3L	10L	4L	25	17	3
Sum				18			15			9			24			25			3H				

See Table 10.

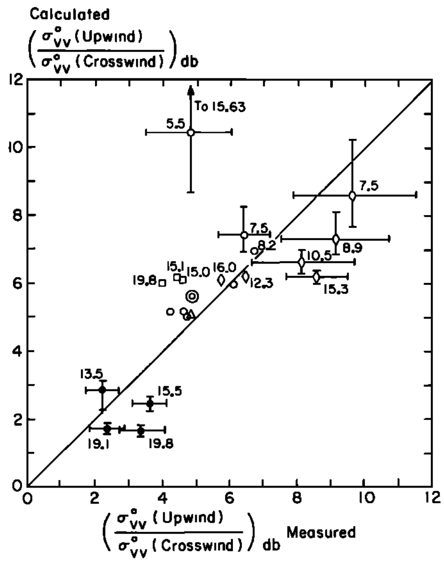

Fig. 19. Measured upwind/crosswind ratios for vertical polarization in decibels on the abscissa versus calculated values on the ordinate for the primary data set.

much as 3 dB. The values of R^2 vary from 0.15 to 0.40. The data are closer to the Schroeder et al. power law than they are to the theory, but even for the power law, the fit is poor. There is one set of three points at 4.6 m s^{-1} that comes close to the theory at upwind and downwind where the waves were categorized as smooth.

The reason for the poor fit is that the wave spectrum used to compute the backscatter was for a fully developed spectrum for the reported wind. The actual waves that were present do not correspond to this assumption for light winds. It is probable that some swell was present. The gravity wave, low-wave number part of the spectrum ($k < 2\pi/82$ cm^{-1}) is probably much higher than the model spectrum used to calculate the backscatter. Moreover, the probability density function for the slopes to tilt the Bragg waves may have variances larger than those predicted from the wind speed. Since specular backscatter is more nearly isotropic, adding a larger isotropic specular component to account for the higher than modeled slope effects may, in part, provide an example of what the waves may have been like. If upwind/downwind differences

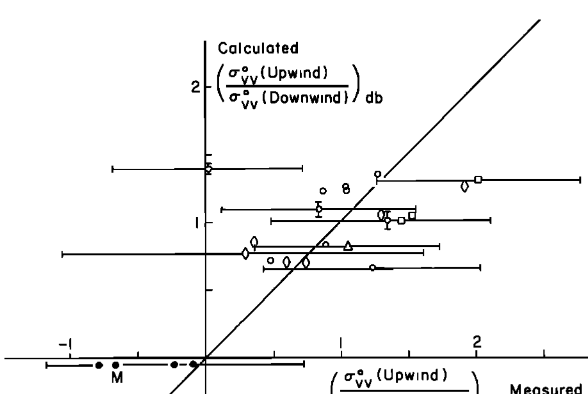

Fig. 20. Measured upwind/downwind ratios for vertical polarization in decibels on the abscissa versus calculated values on the ordinate for the primary data set.

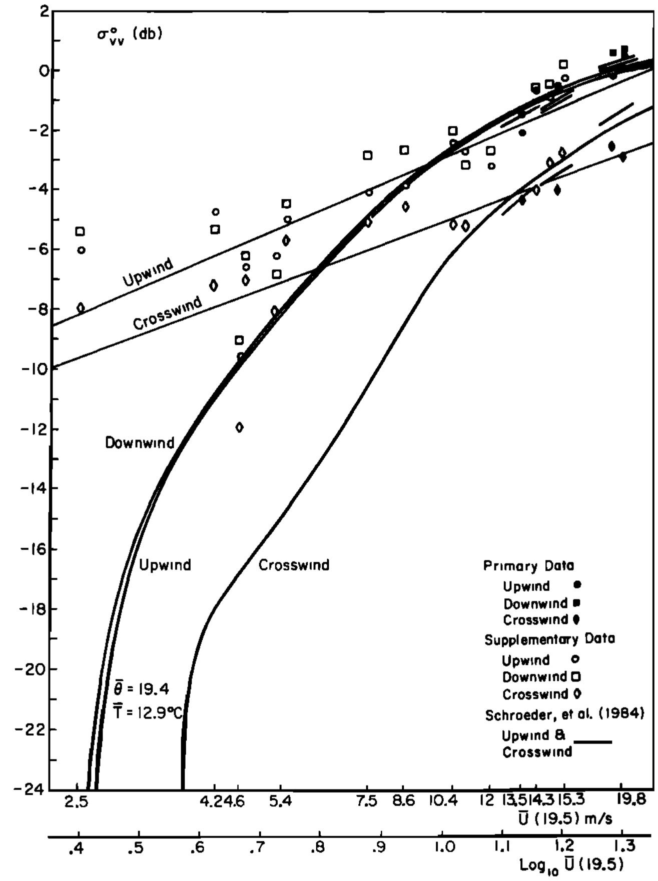

Fig. 21. Theoretical curves for upwind, downwind and cross wind for a 20° incidence angle and a temperature of 12.9°C versus measured values for upwind, downwind and cross wind from the primary and supplementary data sets as coded. The power laws from *Schroeder et al.* [1984] are also shown. (See text.)

are neglected, the data for a wind of 5.4 m s^{-1} can be approximated by

$$\sigma_M{}^0 = 0.31 + 0.039 \cos 2\chi$$
$$= 0.31(1 + 0.13 \cos 2\chi) \qquad (61)$$

The theory would give

$$\sigma_{TH}{}^0 = 0.098 + 0.066 \cos 2\chi$$
$$= 0.098(1 + 0.68 \cos 2\chi) \qquad (62)$$

If 0.212 is added as isotropic specular backscatter to the theory, the result is

$$\sigma_{TH}{}^0 + \sigma_{\text{spec}}{}^0 = 0.098 + 0.212 + 0.066 \cos 2\chi$$
$$= 0.31(1 + 0.21 \cos 2\chi) \qquad (63)$$

For (61), upwind backscatter is about −4.6 dB and crosswind backscatter is about −5.7 dB. For (63), corresponding values are −4.2 dB and −6.1 dB. From Figures 12 and 13, at −6.7 dB (10 $\log_{10}$ 0.212), a wind of about 8 m s^{-1} could have provided the needed gravity wave spectrum. If such a wind had existed a few hours before the circle flight or if gravity waves with an appropriate slope probability density function had propagated into the area where the circle flights were made, then backscatter values similar to those plotted at 5.4 m s^{-1} would have been measured.

At incidence angles near 20°, the specular contribution to

TABLE 12. Comparison of Measured and Calculated Values for Horizontally Polarized Backscatter if Errors for Winds are ± 1 m s^{-1}

			$\sigma^0_{HH(\mathrm{dB})}$												Measured Versus Calculated			Count		
			Upwind Measured	Upwind Calculated			Cross Wind Measured	Cross Wind Calculated			Downwind Measured	Downwind Calculated								
$\bar{\theta}$, deg	$\bar{U}$, m s^{-1}	Viscosity		$\bar{U}-1$	$\bar{U}$	$\bar{U}+1$		$\bar{U}-1$	$\bar{U}$	$\bar{U}+1$		$\bar{U}-1$	$\bar{U}$	$\bar{U}+1$	UP	CR	DN	I	L	H
19.8	13.5	0.0106	−1.75	−2.36	−1.98	−1.63	−3.85	−5.47	−4.77	−4.14	−1.37	−2.35	−1.95	−1.62	I	L	L	1	2	
19.9	15.5	0.0124	−0.52	−1.69	−1.40	−1.15	−3.92	−4.29	−3.78	−3.35	−0.63	−1.68	−1.40	−1.15	L	I	L	1	2	
19.0	19.1	0.0119	0.15	−0.23	−0.09	0.03	−2.54	−1.99	−1.71	−1.48	0.48	−0.21	−0.07	0.05	L	H	L		2	1
18.9	19.8	0.0137	0.66	−0.04	0.08	0.18	−2.80	−1.70	−1.45	−1.25	0.66	−0.12	0.10	0.20	L	H	L		2	1
30.3	9.5	0.0110	−12.25	−13.65	−12.71	−12.22	−15.89	−18.81	−17.80	−16.81	−13.63	−14.66	−13.76	−12.23	I	L	I	2	1	
39.9	5.5	0.0123	−24.16	−29.27	−25.79	−23.57	−29.19	−44.86	−36.55	−32.53	−27.34	−30.31	−26.84	−24.71	I	L	I	2	1	
40.9	7.5	0.0107	−20.18	−24.14	−22.51	−21.18	−25.81	−32.75	−30.34	−28.52	−22.31	−25.25	−23.73	−22.51	L	L	L		3	
39.4	8.2	0.0106	−20.18	−21.84	−20.46	−19.28	−26.12	−29.73	−27.80	−26.25	−22.67	−23.04	−21.76	−20.69	I	L	I	2	1	
40.4	11.3	0.0106	−17.52	−18.91	−18.08	−17.29	−23.04	−25.65	−24.56	−23.62	−20.01	−20.41	−19.66	−18.96	I	L	I	2	1	
40.8	12.8	0.0106	−15.69	−17.96	−17.22	−16.63	−21.88	−24.38	−23.88	−22.71	−17.84	−19.58	−18.93	−18.39	L	L	L		3	
39.1	15.0	0.0118	−14.43	−15.45	−14.92	−14.42	−19.26	−21.30	−20.64	−20.02	−16.54	−17.18	−16.70	−16.26	I	L	I	2	1	
39.4	15.2	0.0125	−13.96	−15.50	−15.04	−14.57	−19.02	−21.44	−20.79	−20.19	−15.84	−17.27	−16.84	−16.41	L	L	L		3	
39.7	15.7	0.0128	−13.93	−15.40	−15.00	−14.55	−18.84	−21.35	−20.73	−20.16	−16.07	−17.21	−16.83	−16.43	L	L	L		3	
38.7	19.4	0.0119	−11.19*	−13.30	−12.97	−12.59	−15.50*	−18.54	−18.09	−17.63	−13.30*	−15.19	−14.89	−14.56	L	L	L		3	
39.1	20.0	0.0137	−13.01*	−13.36	−13.08	−12.72	−18.02*	−18.65	−18.17	−17.78	−13.44*	−15.29	−15.03	−14.72	I	I	L	2	1	
57.8	15.0	0.0118	−22.41	−26.54	−25.94	−25.40	−27.55*	−33.35	−32.68	−32.08	−25.60	−28.41	−27.90	−27.44	L	L	L		3	
58.5	15.1	0.0125	−22.15	−26.87	−26.27	−25.74	−27.95*	−33.75	−33.07	−32.47	−25.61*	−28.76	−28.25	−27.79	L	L	L		3	
58.2	19.8	0.0137	−20.89	−24.40	−24.01	−23.66	−25.20	−31.07	−30.65	−30.28	−24.51	−26.65	−26.34	−26.05	L	L	L		3	
67.2	5.5	0.0123	−36.35	−54.33	−43.97	−40.74	−39.24*	−107.05	−64.62	−52.96	−39.59	−55.97	−45.27	−41.58	L	L	L		3	
67.1	7.5	0.0107	...	...	...	...	...	...	...	...	...	...	...	...						
66.2	8.9	0.0106	−32.34	−36.55	−35.18	−34.03	−39.83	−45.27	−43.17	−41.58	−35.59	−38.00	−36.73	−35.69	L	L	L		3	
65.5	10.5	0.0106	−26.77	−34.11	−33.08	−32.17	−33.84	−41.79	−40.42	−39.29	−28.69*	−35.71	−34.78	−33.98	L	L	L		3	
68.1	12.3	0.0106	−26.74	−33.64	−32.81	−32.08	−32.88	−40.84	−39.83	−38.97	−31.20*	−35.50	−34.76	−34.12	L	L	L		3	
67.3	16.0	0.0128	−24.76	−30.73	−30.17	−29.67	−31.96	−37.67	−37.04	−36.48	−29.38	−32.89	−32.41	−31.98	L	L	L		3	
Total I															7	2	5			
Total H																21				
Total L															16	19	18			
Total count																		14	53	2

$\bar{U}$ is the effective neutral wind at 19.5 m; viscosity is in stokes for fresh water. H, L, and I indicate calculated value too high, calculated value too low, and measured value included in calculated inequality range, respectively.

*Backscatter decreases with increasing wind.

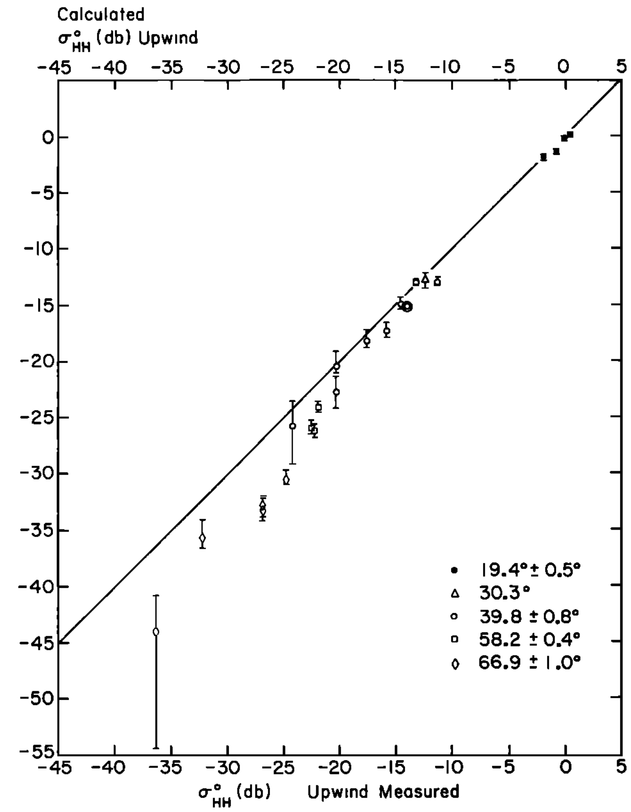

Fig. 22. Measured horizontally polarized backscatter values in decibels (abscissa) for upwind versus values calculated from the model (ordinate) for the primary data set for five incidence angles as coded. The line of perfect agreement is shown.

the backscatter can be important. Especially for light winds, the backscatter can vary for reasons not directly coupled to the local wind speeds over the area where the backscatter is measured. A more complete knowledge of the bivariate probability density function for the wave slopes is then needed to determine the backscatter and, if possible, to determine the wind that produced the Bragg backscatter. This slope probability density function must also be used in (27).

For incidence angles of 30° and higher, the effect of the specular backscatter's being different from the value related to the local wind is not too important for typical wind speeds over the ocean, but from 20° to 30° depending on wind speed, it should be considered in predicting the backscatter and in attempts to recover the wind from the backscatter.

9. RESULTS FOR HORIZONTAL POLARIZATION AT K_u BAND

9.1. *General Properties of Horizontally Polarized Backscatter*

During each circle flight, the radar switched alternately between vertical and horizontal polarization, so that except for small-scale variability in the wind field, both polarizations were measured for the same wind conditions. For incidence angles of 30° and more, horizontal polarization is consistently lower than vertical polarization. For the higher incidence angles, the difference between upwind and downwind backscatter for horizontal polarization becomes clearly evident as shown in Table 1 and as indicated in Table 4 by the effect of this difference on the question of the location of the minimum near cross wind. This marked difference between horizontal polarization and vertical polarization has also been observed for X band and K_a band by *Masuko et al.* [1986]. Note that 318/14/4/12 for a 67.2° incidence angle and a 5.5 m s^{-1} wind speed yields the result that downwind is less than cross wind but that the minimum at 120.6° is less than downwind.

Horizontally polarized backscatter is consistently less than vertically polarized backscatter as shown in the last three columns of Table 1, and the difference increases with increasing incidence angle. For winds from 8.9 to 16 m s^{-1} at the highest incidence angles, downwind can be 9 to 12 dB lower for horizontal polarization compared with vertical polarization.

Since the highest receiver gain channel had to be used for light winds, the elimination of receiver noise would be more critical for horizontal polarization at higher incidence angles. The mean value of the backscatter, A_0, for the lowest wind at 67.2° drops from 7.83 × 10^{-4} to 1.5 × 10^{-4} or nearly 7 dB from vertical polarization to horizontal polarization.

9.2. *Comparison With the Primary Data Set in Terms of Wind Speed Errors*

The computed values for the backscatter for both horizontal and vertical polarization were found with the same computer program for the same runs. At an appropriate place in the program, (26) was used for vertical polarization and (25) was used for horizontal polarizaton. The differences that result are thus the effect of the dielectric properties of seawater for the two polarizations and the variation of the first-order scattering coefficients with instantaneous incidence angle especially with reference to (20).

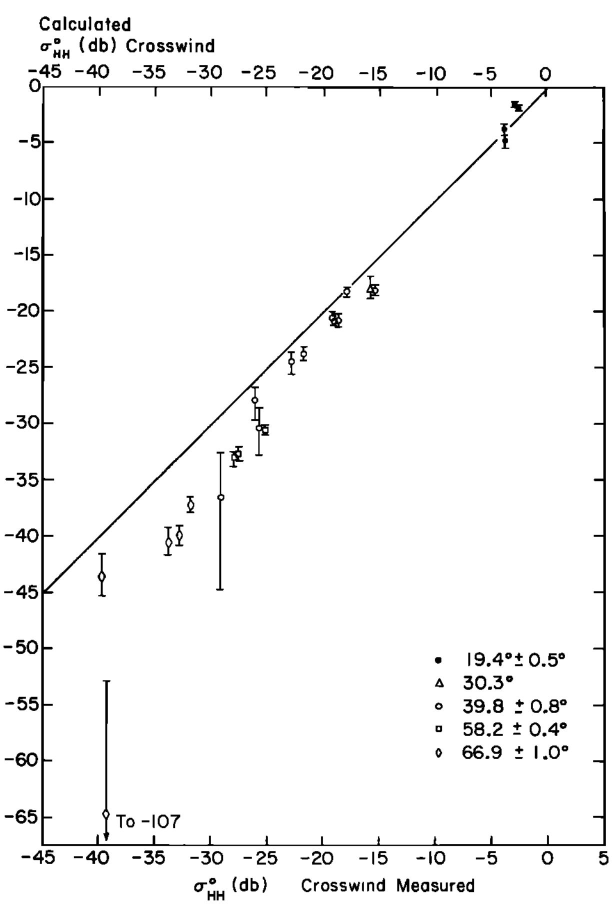

Fig. 23. Same as Figure 22 except for cross wind.

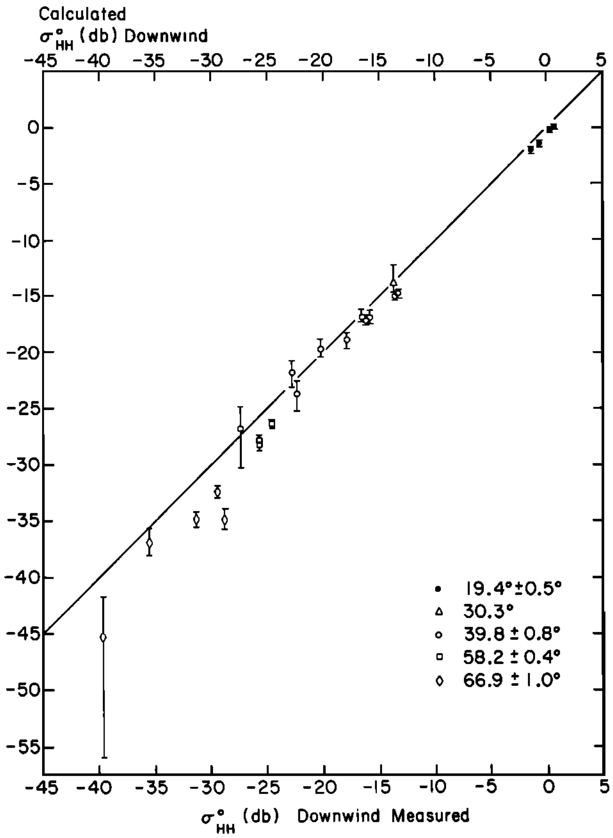

Fig. 24. Same as Figure 22 except for downwind.

Table 12 compares the computed results for the meteorologically reported wind speeds plus or minus 1 m s^{-1} with measured backscatter values at upwind, cross wind (90°) and downwind. By the same scoring system as is used in Table 6 for vertical polarization, the model, in general, predicts values for horizontal polarization that are too low compared with the reported values. It misses completely for the last two ranges of incidence angles. Only 20% of the range of the model values enclose the measured values. For the first three ranges of incidence angle, only 30% meet the criterion. If the value from Table 4 for the minimum near cross wind is used for the 39.4° incidence angle and 8.2 m s^{-1} wind, that value meets the criterion.

Figures 22, 23, and 24 show how well the calculated and measured horizontally polarized backscatter values agree for upwind, cross wind (at 90°) and downwind. The points for Figure 23 would shift to the left by the amounts shown in Table 4 if the minimum near cross wind is used but would still not be close enough to the 45° line except for the point mentioned above. The downwind values in decibels appear to be closest to the line of best fit in an overall sense.

The overall statistics for horizontal polarization under the assumption that both the winds and the backscatter are correct are given in Table 13 based on cross wind at 90° with the data for 5.5 m s^{-1} at 67.2° omitted. The trend with incidence angle in the bias is not consistent for upwind. With the bias removed, the standard deviations in the data are comparable to those for vertical polarization. The upwind/downwind difference in the model is larger for horizontal polarization than for vertical polarization as it is in the data.

9.3. *The Effects of the Estimates of the Errors in the Measurement of σ^0 for the Primary Data Set*

Table 14 for horizontal polarization parallels Table 8 for vertical polarization with three changes. For upwind and downwind, if the range $\sigma^0 - \sigma^0 E$ to $\sigma^0 + \sigma^0 E$ does not include the calculated value from the model, the range is extended to either $\sigma^0 - 2\sigma^0 E$ or $\sigma^0 + 2\sigma^0 E$ as needed, as shown in the column headed $\pm 2\sigma^0 E$. If the $\pm\sigma^0 E$ range included the theoretical value, an "X" is shown. For values near cross wind, the range is extended from the minimum value of the backscatter near cross wind to $\sigma_{\min}{}^0 - \sigma^0 E$ and from the value of the backscatter at 90° to $\sigma^0(90°) + \sigma^0 E$. If this range does not include the calculated value, the range is extended as shown in the column, $\pm 2\sigma^0 E$. Otherwise, an "X" is shown.

The results are shown in the appropriate columns on the right of Table 14 for 1 estimated standard deviation and 2 estimated standard deviations. The model produces values of backscatter that are too low, especially for the higher incidence angles. There is an indication that of the three directions, downwind is modeled most closely in decibels.

Table 15 for horizontal polarization parallels Table 9 except that the range of possible errors for the backscatter measurements is doubled. The computed values do fairly well for the 20°, 30°, and 40° ranges, miss the 58° group, and touch 4 out of 15 of the 67° range for low wind speeds. The patterns for 20° and 30° incidence angles for vertical and horizontal polarization correspond to a decrease in the horizontally polarized calculations relative to the measured values compared with the vertically polarized calculations and the measured values.

TABLE 13. Bias (Computed – Observed), rms Difference, and Standard Deviation in Decibels Less Outrider, Stratified by Upwind, Cross Wind, Downwind, and Incidence Angle for Horizontal Polarization

	Upwind				Cross Wind			Downwind			All Directions			
$\bar{\theta}$, deg	N	Bias	rms	s.d.	Bias	rms	s.d.	Bias	rms	s.d.	N	Bias	rms	s.d.
19.4	4	−0.52	0.60	0.17	−0.06	0.91	0.52	−0.60	0.607	0.04	12	−0.40	0.72	0.18
30.3	1	−0.46	···	···	−0.14	···	···	−0.13	···	···	3	−0.24	0.29	0.11
39.8	10	−1.08	1.29	0.23	−2.17	3.16	0.60	−0.77	1.05	0.74	30	−1.33	1.89	0.25
58.2	3	−0.62	0.68	0.20	−4.557	4.559	0.10	−2.26	2.29	0.23	9	−2.48	2.97	0.58
66.9	4	−5.14	5.32	0.79	−4.73	5.02	0.96	−3.46	3.88	1.07	12	−4.44	4.78	0.53
All angles	22	−1.63	2.46	0.40	−2.48	3.34	0.49	−1.40	2.00	0.31				
All angles, all directions											66	−1.84	2.66	0.23

9.4. *Aspect Angle Variation for Horizontal and Vertical Polarization for the Two-Scale Bragg Model*

As was described in section 7, the circle flight data were processed in two different ways for mission 318. Figure 25 compares horizontally and vertically polarized circle flight data processed in the way described in section 7.4 for winds reported to be 5.5 and 7.5 m s^{-1} with the calculated values from the Bragg model. Figure 26 compares two of the data sets shown in Figure 8 (section 7.5) with values computed from the Bragg model.

As is shown in Figure 25, the backscatter values were averaged in 10° aspect angle ranges, but the values would not necessarily yield an aspect angle at the exact center of the range. The model predicts a large range of backscatter values at a 40° incidence angle at upwind, downwind, and cross wind for both vertical and horizontal polarization for 5.5 $\pm$ 1 m s^{-1} winds. The top part of Figure 25 shows the calculated values for 4.5, 5.5, and 6.5 m s^{-1} and the averaged data plus selected standard deviations for 10° changes in aspect angle. For this light wind, the effect of communication noise in the data reduction procedure could produce the discrepancies that are shown for both polarizations.

For a 7.5 $\pm$ 1 m s^{-1} wind at a 40° incidence angle as in the bottom part of Figure 25, the model calculations for vertical polarization correspond more nearly to an 8.5 m s^{-1} wind. This method of averaging yields an L instead of an I at cross wind. The calculated values for horizontal polarization lie below the measured values for 8.5 m s^{-1} except for one point, as does most of the calculated curve even for 8.5 m s^{-1}.

Figure 26 compares two examples for vertical polarization from Figure 8 with the calculated values from the model for a 12 $\pm$ 1 m s^{-1} wind at an incidence angle of 40.5° and 11.7 $\pm$ 1 m s^{-1} wind for an incidence angle of 67.7° as in Table 3. Neither data set was in the primary data set because of the way the winds were measured as described in section 7.2. They have been chosen to illustrate the difficulty in getting the data and the model to agree. For the 12 m s^{-1} wind, the calculated values lie above most of the data points for the three curves for winds of 11, 12, and 13 m s^{-1}. For the 11.7 m s^{-1} wind, the calculated curves for 10.7, 11.7, and 12.7 m s^{-1} are shown. The data scatter above the calculated curves at upwind and below at cross wind, and they come close at downwind. At cross wind, the data are much lower for 90° than for 270°.

These figures, plus the tabulated and graphed data for vertical and horizontal polarization, show how well the data and the two-scale Bragg model agree. For vertical polarization, at a 40° incidence angle the data for the primary data set agree far better than they do for these examples. The differences are evident, but many of these differences will be explained in section 10.

9.5. *Possible Data Biases*

The possibility that the data might be biased high so as to explain a part of the differences between the model and the measurements needs to be considered before continuing the analysis. The bias is quite possible for light winds as described in section 7.3 and illustrated in Figure 25 for the 5.5 m s^{-1} wind because subtracting an average value for the receiver noise has two effects on the data. If the actual received power and the actual noise for a particular measurement are both low, subtracting an average noise level can produce negative values, which were discarded. Also, the actual noise for a particular measurement can be higher than the average for the noise, so that values are recorded even if there is actually no backscatter.

These two effects combine to make the data that are retained too high, especially for aircraft data. There may also be randomly distributed areas where the light winds have not generated any wave number components that would produce backscatter. For data for winds of less than 5.5 m s^{-1} that were used in the supplementary data set for the study of vertical polarization, this bias is quite possible. For the best circle flight data, this bias may be present for the 5.5 m s^{-1} measurements at both 39.9° and 67.2° incidence angles.

From (54), a value of $(\sigma^0 E)^*$ could be found that would remove the small bias for the high incidence angle range for vertical polarization. However, it would have to increase with increasing incidence angle in an unrealistic way. Were these same values used for the corresponding horizontally polarized data, the value of A_0 would become negative. Conversely, adjustments of the horizontally polarized data would be unrealistic because of the large differences between the model and the data. They would also be too small to affect vertical polarization. It must be concluded that the values of $\sigma^0 E$ that were used in Tables 8 and 14 are a reasonable estimate of the uncertainty in the measurements for all values except perhaps the 5.5 m s^{-1} winds of the primary data set and winds lighter than this for the supplementary data set.

9.6. *Possible Model Biases*

For incidence angles of 30° and greater, there are either 60 or 57 values of backscatter to be compared in Tables 8 and 14. For eight pairs in Table 6 for vertical polarization, the model predicts a value that is high compared with the measurement, and for 24 pairs the model predicts a value that is low based on the $\bar{U} \pm 1$ criterion. For those within the $\bar{U} \pm 1$ criterion, when compared with the model values for $\sigma_{VV}{}^0$ the model predicts a value that is low for 13 of the 28 pairs. Overall, the model is low for 37 pairs and high for 23 for vertical polarization. With three exceptions, the bias for vertical polarization seems to become larger with increasing wind speed and increasing incidence angle. For horizontal polarization, 45 values are low. Of the eight that meet the $\bar{U} \pm 1$ criterion only three of the model values are higher for the reported wind than the measured values, so that 54 values out of 57 are low when the model value for σ^0 is compared to the measured values.

Since our best efforts to tune the model still yielded differences at the high incidence angles, the measured winds would have to be consistently higher than those reported for these high incidence angles to bring the model for vertical polarization into closer agreement with the data. Otherwise, the high–wave number spectrum (equation (11*b*)), would need to be about 60% higher for Bragg wave numbers near a 67° incidence angle for high winds.

Even if this could be done for vertical polarization, it is doubtful that there would be much of an improvement in the results for horizontal polarization.

Although further refinements are undoubtedly possible in the modeling of the Bragg-scattering wave spectrum, the appreciable differences in model versus measurements for horizontal and vertical polarization suggest that other physical effects may be important. In the next section we examine other scattering mechanisms that have been shown, theoretically and experimentally, to produce polarization-dependent scattering.

TABLE 14. Comparison of Estimated Measurement Error for $\pm\sigma^0E$ and

$\bar{\theta}$, deg	$\bar{U}$, m s^{-1}	Upwind: Calculated σ^0	Upwind: Measured σ^0E	Upwind: Measured $\sigma^0-\sigma^0E$	Upwind: Measured σ^0	Upwind: Measured $\sigma^0+\sigma^0E$	Upwind: Measured $\pm2\sigma^0E$	Cross Wind: Calculated σ^0	Cross Wind: Measured σ^0E	Cross Wind: Measured $\sigma_{min}{}^0-\sigma^0E$	Cross Wind: Measured $\sigma_{min}{}^0$	Cross Wind: Measured $\sigma^0(90°)$	Cross Wind: Measured $\sigma^0(90°)+\sigma^0E$	Cross Wind: Measured $\pm2\sigma^0E$
19.8	13.5	−1.98	0.26	−2.01	−1.75	−1.49	X	−4.77	0.26	−4.12	−3.86	−3.85	−3.59	−4.38
19.9	15.5	−1.40	0.26	−0.78	−0.52	−0.26	−1.04	−3.78	0.27	−4.19	−3.92	−3.92	−3.65	X
19.0	19.1	−0.09	0.27	−0.12	0.15	0.42	X	−1.71	0.27	−2.82	−2.55	−2.54	−2.27	−2.00
18.9	19.8	0.08	0.44	0.22	0.66	1.10	−0.22	−1.45	0.61	−3.41	−2.80	−2.80	−2.19	−1.58
30.3	9.5	−12.71	0.87	−13.12	−12.25	−11.38	X	−17.80	0.36	−16.35	−15.99	−15.89	−15.53	−16.71
39.9	5.5	−25.79	0.51	−24.67	−24.16	−23.65	−25.18	−36.55	1.09	−30.87	−29.78	−29.19	−28.10	−31.96
40.9	7.5	−22.51	0.34	−20.52	−20.18	−19.84	−20.86	−30.34	0.48	−26.58	−26.10	−25.81	−25.33	−27.06
39.4	8.2	−20.46	0.89	−21.07	−20.18	−19.29	X	−27.80	1.76	−28.33	−26.57	−26.12	−24.36	X
40.4	11.3	−18.08	0.33	−17.85	−17.52	−17.19	−18.18	−24.56	2.13	−25.55	−23.42	−23.04	−20.91	X
40.8	12.8	−17.22	0.34	−16.03	−15.69	−15.35	−16.37	−23.88	0.73	−22.92	−22.19	−21.88	−21.15	−23.65
39.1	15.0	−14.92	0.36	−14.79	−14.43	−14.07	−15.15	−20.64	0.35	−19.87	−19.52	−19.26	−18.91	−20.22
39.4	15.2	−15.04	0.34	−14.30	−13.96	−13.62	−14.64	−20.79	0.37	−19.60	−19.23	−19.02	−18.65	−19.97
39.7	15.7	−15.00	0.40	−14.33	−13.93	−13.53	−14.73	−20.73	0.57	−19.69	−19.12	−18.84	−18.27	−20.26
38.7	19.4	−12.97	0.36	−11.55	−11.19	−10.83	−11.91	−18.09	0.36	−16.12	−15.76	−15.50	−15.14	−16.48
39.1	20.0	−13.08	0.35	−13.36	−13.01	−12.66	X	−18.17	0.36	−18.39	−18.03	−18.02	−17.66	X
57.8	15.0	−25.94	0.49	−22.90	−22.41	−21.92	−23.39	−32.68	1.07	−29.23	−28.16	−27.55	−26.49	−30.30
58.5	15.1	−26.27	0.33	−22.48	−22.15	−21.82	−22.81	−33.07	0.33	−29.02	−28.69	−27.95	−27.62	−29.35
58.2	19.8	−24.01	0.61	−21.50	−20.89	−20.28	−22.11	−30.65	0.61	−26.54	−25.93	−25.30	−24.59	−27.15
67.2	5.5	−43.97	1.44	−37.79	−36.35	−34.91	−39.23	−64.12	2.48	−42.28	−39.80	−39.24	−36.76	−44.76
66.2	8.9	−35.18	1.14	−33.48	−32.34	−31.20	−34.62	−43.17	2.29	−42.81	−40.52	−39.83	−37.54	−45.10
65.5	10.5	−33.08	0.50	−27.27	−26.77	−26.27	−27.77	−40.42	1.12	−35.29	−34.17	−33.84	−32.72	−36.41
68.1	12.3	−32.81	1.10	−27.84	−26.74	−25.64	−28.94	−39.83	1.18	−35.24	−34.06	−32.88	−31.70	−36.42
67.3	16.0	−30.17	1.15	−25.91	−24.76	−23.61	−27.06	−37.04	1.11	−34.61	−33.50	−31.96	−30.85	−35.72
Total I														
Total L														
Total H														
Total count														

H, L, and I indicate calculated value too high, calculated value too low, and measured value included in calculated inequality range, respectively. X indicates that the $\pm\sigma^0$ range includes the calculated value.

10. EFFECTS OF WEDGES, SPILLING BREAKERS, AND WHITECAPS

10.1. *Observations of Wedges, Spilling Breakers, and Whitecaps*

A two-scale Bragg-scattering model is inherently unable to account for various other features of actual wind-generated waves, in particular those for the fully developed wind seas of this model. The wave number spectrum that has been used appeals to nonlinear considerations to justify its form both for the higher wave numbers in the gravity wave range as in (21) and for physical mechanisms that limit the form of the spectrum in the gravity-capillary range as in (11*b*). For the gravity wave range, those features that are not modeled have to do with the details of how the higher gravity waves in a wind-generated sea actually break and, in so doing, produce surface disturbances with scattering properties that may be quite different from those of tilted Bragg-scattering waves.

The mathematical description of a breaking event is an intractable problem, although some progress for the simplified conditions of one horizontal dimension, height, and time has been made [*Longuet-Higgins*, 1982; *Longuet-Higgins and Cokelet*, 1976]. The short-crested problem for two horizontal dimensions, height, and time has not yet been solved.

A description of breaking events from an observational point of view is, however, possible. When gravity waves are observed, especially from an aircraft, they can be seen to form a pattern of groups of relatively high waves such that the crest to trough heights are high in the middle of a group and taper off in directions both parallel to and normal to the crests of the waves. The groups of waves advance as groups at about one-half the speed of the individual waves in the groups. The group propagation directions are distributed about the wind direction. There are always isolated highest waves somewhere near the center of such groups of waves. Among these randomly scattered wave groups, there will be areas of less well defined lower waves and even areas that are relatively flat, which may contain waves of shorter apparent wavelengths. Individual groups of waves can disappear if followed long enough, and new groups can form where none were identifiable previously. The geometrical properties of wavy surfaces based on a linear wave model have been studied extensively [*Longuet-Higgins and Cartwright*, 1956; *Longuet-Higgins*, 1957, 1958*a*, 1958*b*, 1959, 1960*a*, *b*, *c*].

Waves within a group of waves will move through the group, forming at the rear of a group, growing in height as they advance through the group to some maximum height, and then decreasing in height as they outspeed the group. A particular wave may then perhaps lose its identity in a relatively flat area, or it may catch up to a new group and appear to follow the sequence described previously.

$\pm 2\sigma^0 E$ with Calculated Backscatter in Decibels for U for Horizontal Polarization

Calculated σ^0	Downwind					$\sigma^0 \pm \sigma^0 E$						$\sigma^0 \pm 2\sigma^0 E$					
	Measured					Measured Versus Calculated			Count			Measured Versus Calculated			Count		
	$\sigma^0 E$	$\sigma^0 - \sigma^0 E$	σ^0	$\sigma^0 + \sigma^0 E$	$\pm 2\sigma^0 E$	UP	CR	DN	I	L	H	UP	CR	DN	I	L	H
−1.95	0.28	−1.65	−1.37	−1.09	−1.93	I	L	L	1	2		I	L	L	1	2	
−1.40	0.24	−0.87	−0.63	−0.39	−1.11	L	I	L	1	2		L	I	L	1	2	
−0.07	0.31	0.17	0.48	0.79	−0.14	I	H	L	1	1	1	I	H	I	2		1
0.10	0.55	0.11	0.66	1.21	−0.44	L	H	L		2	1	I	H	I	2		1
−13.76	1.37	−15.00	−13.63	−12.26	X	I	L	I	2	1		I	L	I	2	1	
−26.84	0.72	−28.06	−27.34	−26.62	X	L	L	I	1	2		L	L	I	1	2	
−23.73	0.41	−22.72	−22.31	−21.90	−23.13	L	L	L		3		L	L	L		3	
−21.76	0.77	−23.44	−22.67	−21.90	−21.13	I	I	H	2		1	I	I	I	3		
−19.66	0.43	−20.44	−20.01	−19.58	X	L	I	I	2	1		I	I	I	3		
−18.93	0.80	−18.64	−17.84	−17.04	−19.44	L	L	L		3		L	L	I	1	2	
−16.70	0.37	−16.91	−16.54	−16.17	X	L	L	I	1	2		I	L	I	2	1	
−16.84	0.38	−16.22	−15.84	−15.46	−16.60	L	L	L		3		L	L	L		3	
−16.83	0.39	−16.46	−16.07	−15.68	−16.85	L	L	L		3		L	L	I	1	2	
−14.89	0.36	−13.66	−13.30	−12.94	−14.02	L	L	L		3		L	L	L		3	
−15.03	0.34	−13.78	−13.44	−13.10	−14.12	I	I	L	2	1		I	I	L	2	1	
−27.90	0.56	−26.16	−25.60	−25.04	−26.72	L	L	L		3		L	L	L		3	
−28.25	0.68	−26.29	−25.61	−24.93	−26.97	L	L	L		3		L	L	L		3	
−26.34	0.55	−25.06	−24.51	−23.96	−25.61	L	L	L		3		L	L	L		3	
−45.27	2.66	−42.25	−39.59	−36.93	−44.91	L	L	L		3		L	L	L		3	
−36.73	1.47	−37.06	−35.59	−34.12	X	L	L	I	1	2		L	I	I	2	1	
−34.78	1.12	−29.81	−28.69	−27.57	−30.93	L	L	L		3		L	L	L		3	
−34.76	1.14	−32.34	−31.20	−30.06	−33.48	L	L	L		3		L	L	L		3	
−32.41	1.21	−30.59	−29.38	−28.17	−31.80	L	L	L		3		L	L	L		3	
						5	4	5				8	5	10			
						18	17	17				15	16	13			
							2	1					2				
									14	52	3				23	44	2

Some of the waves that advance through these wave groups attain crest to trough heights that make them hydrodynamically unstable. The first indication of this is the formation of a wedge with a sharp turn at the crest enclosing an interior volume of water locally by two planes at an angle of about 120°. In random waves this interior angle could be considerably less than 120°, but the value of 120° was determined by *Michell* [1893] for periodic long-crested deepwater waves. Although some waves may produce this wedge, travel on, and not break, the usual sequence of events is that a spilling breaker begins to form. If the wave continues to try to increase in height, the spilling breaker continues to be formed, and wedges form to each side along the crest which then make the spilling breaker even wider. As the individual wave continues onward through the group, it decreases in height, hydrodynamic stability is restored, and the generation of the spilling breaker ceases.

A source of the water in the spilling breaker is at the crest of the wave. This water no longer satisfies the set of hydrodynamic equations that are used to describe wave motion because it is a shearing turbulent motion and must have considerable vorticity. This water falls, or slides, or moves, down the downwave side of the advancing wave crest, and as it does so, air is mixed with it to form bubbles, and water from the wave below is entrained to increase the volume of water plus air in the breaker. The air bubbles make the breakers appear white, so that other names for them are "white horses" and "whitecaps."

Models for spilling breakers have been developed by *Longuet-Higgins and Turner* [1974] and *Banner* [1985]. An important feature of these models is that there is a leading edge of the spilling breaker, which behaves like a bore or a local hydraulic jump, on the downwave side. There is a sharp angle, of perhaps as much as 270°, containing a mixture of air and water, with the remaining part consisting of air. This toe of the spilling breaker in a two-dimensional analysis may have some of the properties of the corner reflectors used in the study of synthetic aperture radar (SAR) images for calibration purposes.

The entrained air bubbles are left behind as the nonbreaking wave advances and gradually rise to and break through the surface. The whitecap thus persists for some time after the mechanism that created it has ceased. Examples of whitecap coverage are shown by *Neumann and Pierson* [1966].

Figure 27 is a schematic drawing with the vertical scale exaggerated. It shows a section through a wave group in the upwind/downwind direction as the wave on the left at $t = t_0$ increases in height from t_0 to $t_0 + \tau$ until it forms a wedge at $t_0 + 2\tau$ that develops into a spilling breaker at $t_0 + 3\tau$. It then travels on, decreasing in height and leaving the foam patch behind.

There are probably also plunging breakers on the open sea

TABLE 15. Combined Effect of Wind Speed and Backscatter Bias Errors for Horizontal Polarization

$\bar{\theta}$, deg	$\bar{U}$, m s^{-1}	In $\bar{U}+1$			In $\sigma^0 \pm \sigma^0 E$			In Both			In Either or Corner			In $\sigma^0 \pm 2\sigma^0 E$			In Either $\bar{U} \pm 1$ or $\sigma^0 \pm 2\sigma^0 E$			In Either or Corner			Out			Count		
		UP	CR	DN	UP	CR	DN	UP	CR	DN	UP	CR	DN	UP	CR	DN	UP	CR	DN	UP	CR	DN	UP	CR	DN	I	L	H
19.8	13.5	I			I			I			I		B	I			I			I	B	B				3		
19.9	15.5		I			I			I			I			I			I			I		L		L	1	2	
19.0	19.1				I						I			I		I	I		I	I		I		H		2		1
18.9	19.8												B	I		I	I		I	I	A	I				3		
30.3	9.5	I		I	I		I	I		I	I		I	I		I	I		I	I		I		L		2	1	
39.9	5.5	I		I			I			I	I		I			I	I		I	I		I		L		2	1	
40.9	7.5												B									B	L	L		1	2	
39.4	8.2	I		I	I	I		I			I	I	I	I	I	I	I	I	I	I	I	I				3		
40.4	11.3	I		I		I	I			I	I	I	I	I	I	I	I	I	I	I	I	I				3		
40.8	12.8											B	B			I			I		B	I	L			2	1	
39.1	15.0	I		I			I			I	I		I	I		I	I		I	I	B	I				3		
39.4	15.2																			B		B		L		2	1	
39.7	15.7												B			I			I	B	B	I				3		
38.7	19.4																						L	L	L		3	
39.1	20.0	I	I		I	I		I	I		I	I		I	I		I	I		I	I				L	2	1	
57.8	15.0																						L	L	L		3	
58.5	15.1																						L	L	L		3	
58.2	19.8																						L	L	L		3	
67.2	5.5												B									B	L	L		1	2	
66.2	8.9						I					B	I		I	I		I	I		I	I	L			2	1	
65.5	10.5																					B	L	L		1	2	
68.1	12.3																						L	L	L		3	
67.3	16.0																						L	L	L		3	
Count		7	2	5	5	4	5	4	2	4	8	4	6	8	5	10	9	5	10	9	5	10	12L	12L	8L	36	32	1
Corner												2	6							2	5	5		1H				
Sum			14			14			10			26			23			24			36			33				

A denotes high σ^0 and low $\bar{U}$; B denotes low σ^0 and high $\bar{U}$.

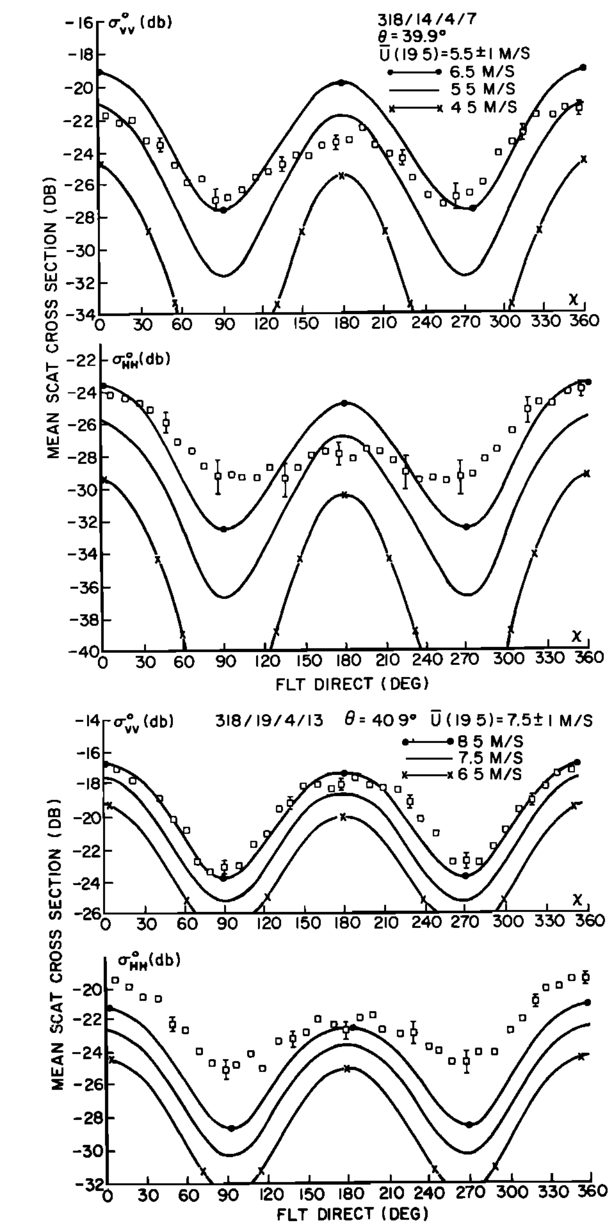

Fig. 25. Aspect angle (or azimuth) dependence of vertically and horizontally polarized backscatter from the model for $\bar{U} - 1$, $\bar{U}$ and $\bar{U} + 1$ with $\bar{U}$ equal to 5.5 and 7.5 m s^{-1} for an incidence angle near 40° compared to bin-averaged backscatter values with some confidence intervals shown.

similar to those modeled by *Longuet-Higgins and Cokelet* [1976]. They could produce specular backscatter slopes for any incidence angle just before breaking. However, spilling breakers as described above greatly outnumber the plunging breakers and may well be one of the dominant effects to be considered in the study of backscatter from a wind generated sea.

Monahan and O'Muircheartaigh [1980, 1981, 1986] have studied the properties of whitecaps including the fraction of the sea surface covered by whitecaps. The most recent report, though directed toward applications to passive remote sensing, [*Monahan and O'Muircheartaigh*, 1986], contains many results that parallel the results of *Kahma and Donelan* [1987] and properties of the wave spectral model derived above.

A wind speed at 10 m is defined by them to be the velocity

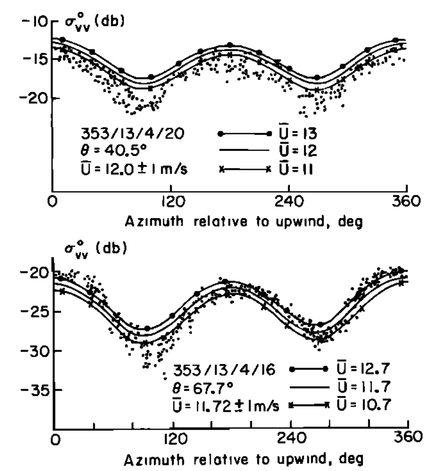

Fig. 26. Calculated backscatter for vertical polarization versus AAFE RADSCAT data for the conditions shown.

U_B when the whitecap coverage, defined in a standardized way, equals 0.1%. The value of U_B is a function of the air/water temperature difference, the wind at 10 m, and the water temperature. For neutral stratification, U_B is nearly 3.4 m s^{-1} for 0°C water and about 2.7 m s^{-1} for 30°C water. For a stably stratified atmosphere, for perhaps some constant water temperature, the wind at 10 m must be about 7.5 m s^{-1} for 0.1% whitecap coverage if the water is 8°C colder than the air. If the water is 4°C warmer than the air, a wind of slightly more than 2 m s^{-1} is needed. Were the data stratified in terms of the effective neutral wind by means of Monin-Obukhov theory, the effect of water temperature could be more clearly isolated.

The number of wedges and active spilling breakers in a wind sea at some instant of time is in some way related to the fraction of whitecap coverage, but since larger whitecaps last longer, the relation may not be a simple one. The fraction of the sea surface covered by whitecaps, which can be as high as 0.20 for 20 m s^{-1} winds, has been represented by a power law.

That whitecap coverage of the sea surface can be solely a

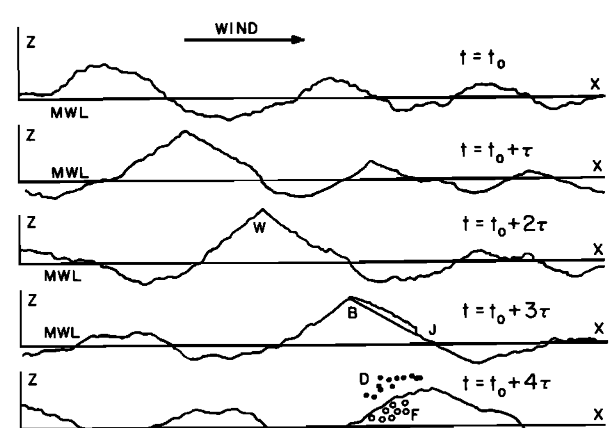

Fig. 27. Schematic diagram, with the vertical scale exaggerated, through the center line of a group of waves. As the wave on the left at the top advances from $t = t_0$ to $t = t_0 + \tau$, it steepens and forms a sharp wedge (labeled W) at $t = t_0 + 2\tau$. This is followed for a short while by a spilling breaker (B), with a hydraulic jump (J) at the toe of the breaker, as at $t = t_0 + 3\tau$. As the wave decreases in height on progressing through the group, the breaking action ceases and a foam patch (F) and water drops (D) are left behind.

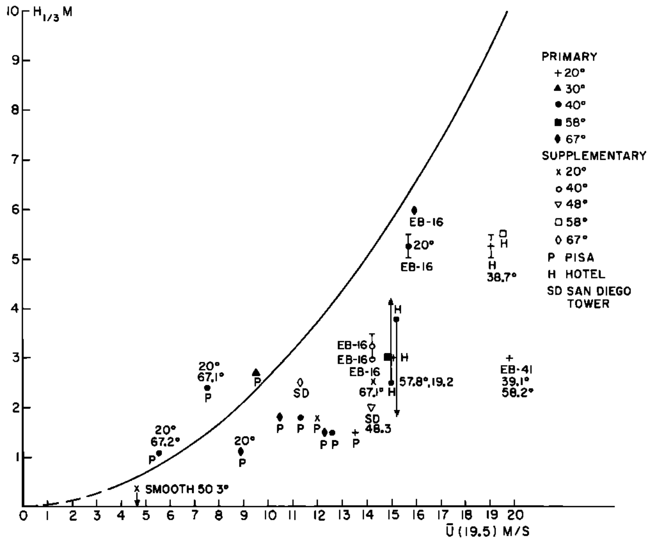

Fig. 28. Reported wave heights, interpreted as significant wave heights, for the wind speeds during the circle flights of the primary and supplementary data sets, coded by incidence angle and location.

function of the above parameters seems to be a doubtful hypothesis. The most direct counterexample is the probable fetch dependence. A constant offshore wind for a simple coastal geometry, constant air-sea temperature difference, and constant water temperature would generate waves that would increase in height as a function of fetch. The number and size of the whitecaps would thus be a function of fetch as well as a function of the other variables if such measurements were repeated for different winds, air/sea temperature differences, and water temperatures.

The whitecap production index developed by *Cardone* [1969] has been extended by *Monahan* [1971, 1986] to describe the rate of whitecap area formation, and the effect of fetch has been studied [*Monahan and Monahan*, 1985]. These results may be extendable to allow the calculation of the effects of wedges and breakers on backscatter.

10.2. *Wave Height Versus Wind Speed for the Circle Flight Data*

The slopes that enter into the calculation of Bragg backscatter are from the high-wave number part of the spectrum. Whether or not the seas are fully developed for the wind at 19.5 m is not very critical (see section 5.5). On the other hand, for wedges, spilling breakers, and whitecaps, whether or not the seas have reached full development and are in equilibrium with the local wind is important. Missions with the primary objective of measuring backscatter as a function of wind speed may not pay sufficient attention to the question of stage of development of the wave field.

It is difficult to find conditions that correspond to an equilibrium between the wind and the waves for sufficiently long fetches, wind durations, and high winds. This is illustrated by *Moskowitz* [1964], who searched the wind fields associated with 460 spectral estimates before it was possible to find 54 spectral estimates that would correspond to fully developed seas.

Figure 28 shows the significant wave heights as a function of the wind speed as reported for 23 of the 24 primary data sets and for 13 of the 29 supplementary data sets. Many of the reported heights are visual estimates in 0.5-m steps, which are not very reliable. Swell cannot always be distinguished from a wind sea by visual observations, but if swell was reported it is shown by an arrow pointing to its value originating from the coded point. The points are coded by incidence angle starting at the top of Table 2 and continuing to Table 3. As the incidence angle was varied for a particular mission and flight, the wave height and wind speed were often reported as unchanged. For such points, both the higher incidence angles and the incidence angles for the supplementary data set are shown near the point as coded for the first occurrence in the tables. Also, the location of the measurements is shown as coded. The highest waves at PISA were 2.7 m for a 9.5 m s^{-1} wind from 230°.

The waves are not a monotonically increasing function of wind speed. Also shown is the significant height for the fully developed spectrum used in the backscatter model. The significant wave heights are about 20% higher for this model than those of *Pierson and Moskowitz* [1964]. The backscatter values flagged with an asterisk in Tables 6 and 12 are generally those that are associated with a decrease in reported wave height for increasing wind speed. The most striking example is for the two circle flights for incidence angles of 38.7° and 39.1° for 19.4 and 20 m s^{-1}. The wave height for the 19.4 m s^{-1} wind was about 5 to 5.5 m, whereas for the 20 m s^{-1} wind it was about 3 m. The backscatter for the 19.4 m s^{-1} wind was 1.33 and 1.71 dB higher at upwind and cross wind for vertical polarization and 1.82, 2.52, and 0.14 dB higher for upwind, cross wind, and downwind, respectively, for horizontal polarization compared with the 20 m s^{-1} wind. Since the area under the variance spectrum varies as the square of the wave height, a factor of about 4 is involved, and consequently the effects of tilt are considerably greater at the lower of these two wind speeds.

Waves in the North Sea measured at PISA exceeded the heights for fully developed seas, from the available reports, for

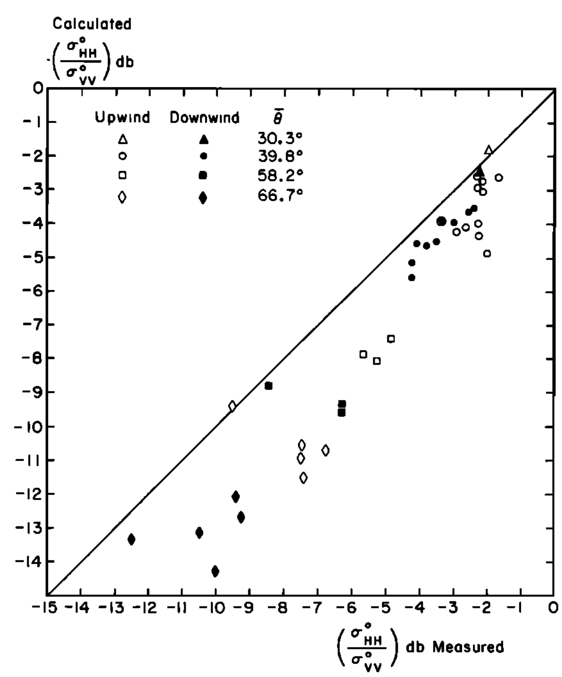

Fig. 29. Measured ratio in decibels of horizontally polarized to vertically polarized backscatter (abscissa) versus calculated values (ordinate) for upwind and downwind for various incidence angles as coded on the figure.

TABLE 16. Estimated Values for $\sigma_T{}^0$, $\sigma_W{}^0$, and $\sigma_J{}^0$ for $\theta = 68.1°$ and $\bar{U} = 12.3$ m s^{-1}

	Horizontal Polarization			Vertical Polarization		
	UP	CR	DN	UP	CR	DN
$\sigma_B{}^0$	0.524	0.104	0.334	8.63	2.07	6.80
$\sigma_T{}^0$	0.286	0.286	0.286	0.86	0.86	0.86
$\sigma_B{}^0 + \sigma_T{}^0$	0.810	0.390	0.620	9.49	2.93	7.66
$\sigma_W{}^0$	0.36		0.36	1.34		1.34
$\sigma_B{}^0 + \sigma_T{}^0 + \sigma_W{}^0$	1.17		0.98	10.83		9.00
$\sigma_J{}^0$	0.95			1.87		
$\sigma_B{}^0 + \sigma_T{}^0 + \sigma_W{}^0 + \sigma_J{}^0$	2.12			12.70		
Measured $- \sigma^0 E$	1.64	0.299	0.583	10.54	2.02	7.70
Measured	2.12	0.393	0.759	11.59	2.48	8.55
Measured $+ \sigma^0 E$	2.73	0.676	0.986	12.73	3.39	9.48

Values are in antilog form times 10^3.

only three flights for winds of less than 10 m s^{-1}. From 10 to 14 m s^{-1}, fetch limitations for many wind directions limit the wave height. The high waves off the west coast of the United States are the closest to full development. Westerly to northwesterly winds at *Hotel* and EB41 also imply fetch-limited seas.

10.3. *The Scattering of Electromagnetic Waves by Wedges*

The scattering of electromagnetic waves by wedges has been described theoretically by *Lyzenga et al.* [1983] and applied to the backscatter data of *Guinard and Daley* [1970]. They cite *Kalmykov and Postovoytenko* [1976] and *Lewis and Olin* [1980], who suggest that wedges enhance backscatter at high incidence angles, the former for horizontal and the latter for vertical polarization. *Kwoh and Lake* [1984] have merged theory and observations in a study made in an experimental wave tank. For the experimental part, waves were generated in a wave tank in the complete absence of a wind that were steep enough and irregular enough to produce a wedge at the wave crest every so often. This wedge often generated parasitic capillary waves [*Longuet-Higgins*, 1963] which were analyzed separately.

The major thrust of the investigation was to study scattering from wedges over the entire upper half plane for transmitted radar waves at X band (9.23 GHz) at 40°, 55°, and 67.7° incidence angles and backscatter from wedges at these same angles. The theory and the data agreed quite well for this aspect of the study. Measured backscatter from a wedge varied from -30 dB to -15 dB for horizontal polarization and from -20 to -7 dB for vertical polarization at 67.7°. Corresponding values were from -25 to -15 dB and -15 to -10 dB at 55° and from -25 to -5 dB and -14 to -1 dB at 40°. At 67.7°, the measured polarization ratio, that is, $(\sigma_{VV}{}^0/\sigma_{HH}{}^0)_{\text{dB}}$, varied from 6 to 13 dB; at 55° it varied from 4 to 7 dB, and at 40°, it varied from 1 to 7 dB. The values had considerable scatter but appeared to be concentrated near 8 dB for 67.7°, 6 dB for 55°, and 2 to 3 dB for 40°.

The variation from one measurement to the next is probably related to the curvature at the wedge, with some wedges being sharper than others, and to variations in the interior angle about the theoretical value of 120°. Wedges on the crests of waves in a wind sea will depart from the wedges of this experiment in numerous ways. They will not be straight; the interior angle will probably increase from 120°, or so, to each side, and they may not be as sharply pointed.

10.4. *The Scattering of Electromagnetic Waves by Spilling Breakers*

Wetzel [1986] has treated numerous aspects of backscatter from the hydraulic jump at the toe of a spilling breaker with models for the breaker sections normal to the direction of wave travel based on the results of *Longuet-Higgins and Turner* [1974]. Both physical optics models independent of polarization and models dependent on polarization and scale are given.

Wetzel's Figure 5 is a schematic drawing that shows the relative importance of wedge, spilling breaker, and rough surface plus spray models as a function of frequency. The concept that the backscatter from a breaker, and probably from a wedge, will be reduced by a roughness factor for scales comparable to and smaller than the radar wavelength is introduced. The various effects probably overlap and contribute various proportions to the total as the wave number is varied. Wedges would be dominant at L band; both wedges and breakers would be important at C band; breakers and rough surfaces (plus spray) would be important at X and K_u band. These possible effects vanish at K_a band.

Wetzel interprets his results very cautiously, and in a sense, this work can be considered a guide to avenues for future research and more detailed analysis. The "fugitive" nature of breakers (a characterization by Phillips) and the need for a morphology of an evolving breaker is emphasized so as to permit extending the backscatter theory in a more consistent way.

In this work a breaker is treated as a single target so that the backscattering cross section of the target is computed. Several different ways of doing this all lead to a cross section of about 1 m^2. For scatterometry purposes, if there was one spilling breaker per, say, 10,000 m^2 of the incident wave front, the normalized backscattering cross section would be $10^{-4}/\cos\theta$ for the dimensionless quantity, σ^0, as calculated in our model for the combined effects of specular and Bragg scattering.

Banner and Fooks [1985] have used the concept of the artifice of steady motion [*Lamb*, 1932, chaper IX, article 250] to develop an experimental facility in which a spilling breaker can be produced that stands still in the wave flume and can be observed continuously along cross sections near the center line of the flume and normal to it. A steady moving current in what would be the upwind direction was produced in the flume, and a curved inclined plane at the entrance of the

TABLE 17. Estimated Effects of Bragg Scattering, Wedges, and Spilling Breakers on

$\bar{\theta}$, deg	$\bar{U}$, m s^{-1}	Polarization	$\sigma_B{}^0$ UP	$\sigma_B{}^0$ CR	$\sigma_B{}^0$ DN	$\sigma_T{}^0$	$\sigma_W{}^0$	$\sigma_J{}^0$	$\sigma_{BBW}{}^0$ UP	$\sigma_{BBW}{}^0$ CR	$\sigma_{BBW}{}^0$ DN	$\sigma^0 - \sigma^0 E$ Measured UP	$\sigma^0 - \sigma^0 E$ Measured CR	$\sigma^0 - \sigma^0 E$ Measured DN
57.8	15	*HH*	2.55	0.54	1.62	0.90	0.45	2.24	6.14	1.44	2.97	5.13	1.20	2.40
		VV	17.58	4.35	13.90	2.21	0.22	0.99	21.0	6.56	16.33	19.31	6.56	16.33
58.5	15.1	*HH*	2.36	0.49	1.50	0.95	0.45	2.24	6.10	1.44	2.90	5.65	1.25	2.35
		VV	17.02	4.15	13.43	2.25	0.50	0.99	21.06	6.70	16.48	19.31	6.70	12.97
58.2	19.8	*HH*	3.97	0.86	2.32	1.36	0.32	2.50	8.15	2.22	4.00	7.08	2.22	3.12
		VV	23.6	5.93	17.58	...	...	...	...	...	...	22.91	9.02	14.29
66.2	8.9	*HH*	0.303	0.0482	0.212	0.0405	0.0795	0.160	0.583	0.0887	0.332	0.449	0.052	0.197
		VV	5.43	1.009	4.52	0.040	0.20	0.13	5.80	1.049	4.76	4.75	0.493	4.01
65.5	10.5	*HH*	0.492	0.0907	0.3326	0.2343	0.6311	0.743	2.10	0.325	1.198	1.87	0.296	1.044
		VV	7.50	1.64	6.14	0.66	3.20	1.74	13.10	2.30	10.00	10.88	1.81	9.95
68.1	12.3	*HH*	0.524	0.104	0.334	0.286	0.36	0.95	2.12	0.390	0.98	1.64	0.279	0.583
		VV	8.63	2.07	6.80	0.86	1.34	1.87	12.70	2.93	9.00	10.54	2.02	7.70
68.1	16.0	*HH*	0.962	0.198	0.575	0.436	0.49	1.96	3.85	0.635	1.50	2.56	0.346	0.870
		VV	12.44	3.04	9.31	1.01	1.50	3.92	18.87	4.05	11.82	12.08	3.33	7.66

Notation is as follows: $\sigma_B{}^0$, Bragg; $\sigma_T{}^0$, turbulence; $\sigma_W{}^0$, wedges; $\sigma_J{}^0$, hydraulic jumps; $\sigma_{BBW}{}^0$, Bragg, breakers, and wedges; $\sigma_{BW}{}^0$, breakers and wedges. Values are in antilog form times 10^3 except last two backscatter ratios. An ellipsis means that the value cannot be calculated because Bragg at downwind exceeds measured values.

working section produced a train of stationary gravity waves. An obstacle like an aircraft wing with a length of 96 mm and a chord of 21 mm was placed below the water so that one of these waves became unstable and resulting in a spilling breaker. They state that

> ...adjustment of the depth and angle of inclination of the obstacle allowed fine-tuning of the degree of breaking, ranging from incipient to very strong: this latter condition, not studied here, had the appearance of a local hydraulic jump. The properties of the hydrodynamic disturbances under gentle breaking were investigated in this study with the obstacle inclined just beyond the point for incipient breaking of the wave immediately downstream. Two wavelengths, 0.20 and 0.33 m, were chosen as representative of small-scale breaking waves. At these scales little, if any, air entrainment or spray was present.

Their Figure 2 shows the two cases that were studied. The higher breaker of the two shows a weak hydraulic jump with a curved forward edge and smooth water ahead of the breaker since there was no wind. There are undulations on the breaker part and also behind it, with very irregular forms that were investigated in terms of flows with vorticity. A relationship between wave number and frequency for the turbulent undulations on the breaker was found for the strongly sheared flow produced by the opposing currents in the breaker and the wave below [*Banner*, 1985]. Backscatter measurements were made at incidence angles of 50°, 30°, and 10° in what would correspond to the upwind direction for moving waves for 10-cm portions of the breaker along the long axis of the working section. The appearance of the turbulence undulations behind the breaker jump suggests that cross-wind backscatter would have been as strong as that measured in the upwind direction if such measurements had been made.

The backscattered power at X band (9.23 GHz) that was measured depended on the location of the entire 10-cm area that was sampled, and thus the contribution of the toe of the breaker was not isolated from the turbulent undulations near it. Had a more intense spilling breaker as described in the above quotation been investigated, the effects of the toe of the breaker, or of the hydraulic jump, might have been much more pronounced. The backscattered power reached a peak somewhere in the vicinity of the toe of the breaker. Vertically polarized backscatter was up to 3 dB stronger than horizontally polarized backscatter.

10.5. *Modifications of the Two-Scale Bragg-Scattering Model to Account for Wedges and Spilling Breakers*

The horizontally polarized backscatter values from the model are much lower than the measured values. To emphasise that the effect is dominantly for discrepancies for horizontal polarization, the inverse of the polarization ratio is shown in Figure 29 as values of $(\sigma_{HH}{}^0/\sigma_{VV}{}^0)_{\mathrm{dB}}$ for upwind and downwind. All but two of the points fall below the line of perfect agreement. The discrepancies for incidence angles near 40° amount to 1 or 2 dB, those near 50° amount to 2 or 3 dB, and those near 67° amount to 3 or 4 dB. For high incidence angles and high winds the model is biased low for both vertical and horizontal polarization. For an error of 3 dB there need to be additional effects equal in importance to the effects already considered in the two-scale model. It was found in section 8.1 that specular backscatter at times exceeded the Bragg backscatter for a 20° incidence angle. When the two effects were equal, the combined effect was thus 3 dB higher than either one alone. From the differences shown in the various tables and figures, these effects, assumed to be due to wedges and breakers, need to be greater than those for Bragg scattering alone for horizontal polarization.

A model for the effects of wedges and spilling breakers is needed. As a working hypothesis we offer the following. In antilog form, for either polarization and omitting subscripts for polarization, let the cross-wind CR, downwind DN and upwind UP backscatter be defined by

$$\sigma_{\mathrm{CR}}{}^0 = \sigma_B{}^0 + \sigma_T{}^0 \tag{64}$$

$$\sigma_{\mathrm{DN}}{}^0 = \sigma_B{}^0 + \sigma_T{}^0 + \sigma_W{}^0 \tag{65}$$

$$\sigma_{\mathrm{UP}}{}^0 = \sigma_B{}^0 + \sigma_T{}^0 + \sigma_W{}^0 + \sigma_J{}^0 \tag{66}$$

where $\sigma_B{}^0$ is the result from the two-scale Bragg model.

It is assumed that the turbulent undulations on the spilling breaker are isotropic as represented by $\sigma_T{}^0$ and return the

Horizontally and Vertically Polarized Backscatter for Incidence Angles Near 58° and 67°

σ^0 Measured			$\sigma^0 + \sigma^0 E$ Measured			$(\sigma_{BW}{}^0/\sigma_B{}^0)_{\mathrm{dB}}$			$(\sigma_{VV}{}^0/\sigma_{HH}{}^0)_{\mathrm{dB}}$			Wave Height, m
UP	CR	DN	UP	CR	DN	UP	CR	DN	*T*	*W*	*J*	
5.74	1.53	2.75	6.42	2.24	3.13	1.5	2.2	−0.8	3.9	−3.1	3.5	2.5
21.00	6.78	15.80	22.80	7.96	16.33	−7.1	−2.9	−7.6				
6.10	1.35	2.75	6.58	1.73	3.21	2.0	2.9	−0.3	4.3	0.5	3.5	3
21.00	7.21	14.62	24.21	8.28	16.48	−6.2	−2.1	−6.4				
8.15	2.95	3.54	9.38	3.47	4.01	0.2	2.0	−1.4	...	...	...	3
24.89	9.51	15.63	27.04	10.89	17.10	...	...	...				
0.583	0.0887	0.276	0.759	0.1262	0.387	−0.03	−0.08	−2.5	0.0	4.0	−0.9	1.1
5.26	0.641	4.93	5.82	0.834	6.07	−11.7	−1.4	−12.74				
2.10	0.383	1.352	2.36	0.535	1.750	5.1	4.1	5.6	4.5	7.1	3.7	1.8
11.93	1.83	11.04	13.15	2.37	12.24	−1.3	−4.0	−2.0				
2.12	0.393	0.759	2.73	0.676	0.986	4.8	4.4	2.9	4.8	5.7	2.9	1.5
11.59	2.48	8.55	12.73	3.39	9.48	−3.3	−3.8	−5.0				
3.34	0.447	1.15	4.35	0.882	1.52	4.8	3.4	2.1	3.6	4.9	3.0	6.0
15.78	4.05	10.12	20.60	5.49	13.36	−2.9	−4.8	−5.7				

same incoherent amount to the radar for all aspect angles. Backscatter from wedges, $\sigma_W{}^0$, is assumed to be dominantly incoherent in either the upwind or downwind direction with no important contribution to cross wind. The aspect angle spread to each side of upwind and cross wind would have to be a subject of further research. Finally, the effect of the hydraulic jump at the toe of the spilling breaker, $\sigma_J{}^0$, can only be seen by the radar from geometrical considerations when the radar is looking upwind. The dependence on aspect angle near upwind would need to be the subject of further research.

A full theory for the effects of wedges and spilling breakers would have to start with values for the number; dimensions, including the sharpness of the angles at the wedge; and three-dimensional orientation of the wedges in a given seaway. Their size would be a function of the radar wave number. The backscatter from this distribution of wedges would then have to be combined incoherently to obtain the amount contributed to the values of σ^0 for each polarization. The measurements made so far under idealized laboratory conditions are insufficient for detailed calculations. There are no theoretical results for backscatter from the hydraulic jumps at the toes of spilling breakers. These are also actually moving and changing three-dimensional structures with a large variety of possible shapes. When the breaker action ceases, the undulations on the turbulent patch of water are left behind and may persist first at the crest of the no-longer-breaking wave and then on the upwind side.

In Table 16 the values of $\sigma_T{}^0$, $\sigma_W{}^0$, and $\sigma_J{}^0$ starting with the values for $\sigma_B{}^0$ are calculated according to a simple set of rules. The values from the Bragg model for the wind speed data under analysis are in the first row. The last three rows give the measured values and those for minus one error bound and plus one error bound as calculated from Tables 8 and 14. Values for $\sigma_T{}^0$, $\sigma_W{}^0$, and $\sigma_J{}^0$ in accordance with (64) to (66) are then determined so that the appropriate totals will add to a value close to the measured value but within the error uncertainty of the measurement. Based on similar calculations for the other circle flights, an attempt was also made to have the various effects increase with increasing wind speed in a smooth way. Adding too much or too little to first the cross-wind value and then the downwind value may use up too much or too little of the available amounts so that upwind becomes unrealistic. The sums that result are thus not always exactly at the measured values for this reason.

Table 17 shows the results of similar calculations for the 58° and 67° incidence angle data. The calculations did not yield and results for vertical polarization for the 58.2° incidence angle, 19.8 m s^{-1} wind because the values that would be needed are far outside of the $\pm\sigma^0 E$ bounds. This result is again an example of wave conditions where the waves are not high enough to correspond to the assumptions of the Bragg model. Also, the value 1.049 used for cross wind for the 66.2°, 8.9 m s^{-1} data is outside the $\pm\sigma^0 E$ bound but within the $+2\sigma^0 E$ bound.

The values in this table are in general agreement with the present understanding of the increasing nonlinearity of wind waves with increasing height and wind speed. For horizontal polarization 66.2°, 8.9 m s^{-1} the effects are relatively small, as is shown by the column headed $(\sigma_{BW}{}^0/\sigma_B{}^0)_{\mathrm{dB}}$. This quantity is the ratio of the sum of $\sigma_T{}^0$, $\sigma_W{}^0$, and $\sigma_J{}^0$ to the value of $\sigma_B{}^0$. If it is near zero in decibels, the combined effect of breakers and wedges is the same as the contribution from Bragg scattering. For this circle flight, for horizontal polarization, breakers and wedges are only as important as Bragg scattering.

As the wind increases for the data with incidence angles near 67°, the effect of wedges and breakers is more important

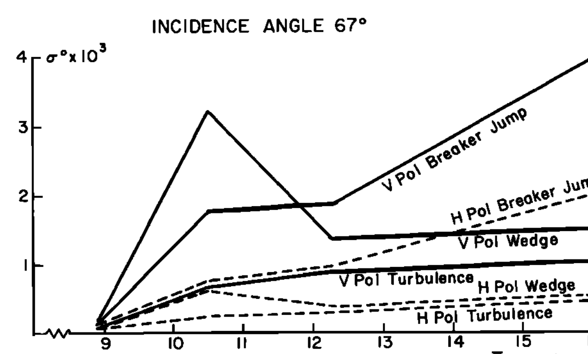

Fig. 30. Estimated contributions to the total backscatter from turbulent undulations on spilling breakers, hydraulic jumps at the toes of spilling breakers, and wedges for horizontal and vertical polarization at incidence angles near 67°.

TABLE 18. Estimated Effects of Bragg Scattering, Wedges, and Spilling Breakers on

$\bar{\theta}$, deg	$\bar{U}$, m s^{-1}	Polarization	σ_B^0			σ_T^0	σ_W^0	σ_J^0	σ_{BBW}^0			$\sigma^0 - \sigma^0 E$ Measured		
			UP	CR	DN				UP	CR	DN	UP	CR	DN
40.4	11.3	*HH*	15.56	3.50	10.81	0.17	0.04	1.93	17.70	3.69	11.02	16.40	2.79	9.036
40.8	12.8	*HH*	18.97	4.09	12.79	1.70	1.95	4.35	26.97	5.79	16.44	24.95	5.10	13.68
39.1	15.0	*HH*	32.21	8.63	21.38	1.67	1.10	2.52	37.61	10.30	24.15	33.19	10.30	20.37
39.4	15.2	*HH*	31.33	8.34	20.70	3.60	3.70	4.37	43.00	11.94	28.00	37.15	10.96	23.87
39.7	15.7	*HH*	31.62	8.45	20.75	3.04	3.25	6.39	44.30	11.49	27.04	36.89	10.74	22.59
38.7	19.4	*HH*	50.47	15.52	32.43	9.96	6.40	9.20	76.03	25.48	48.79	69.98	24.43	43.05
38.7	19.4	*VV*	100.23	30.20	73.11	8.52	6.07	6.80	121.62	46.13	87.70	120.09	38.72	76.03

Notation is as follows: σ_B^0, Bragg; σ_T^0, turbulence; σ_W^0, wedges; σ_J^0, hydraulic jumps; σ_{BBW}^0, Bragg, breakers, and wedges; σ_{BW}^0, breakers and wedges. Values are in antilog form times 10^3 except last two backscatter ratios. Swell is given in parentheses.

than Bragg scattering by a factor of 2 or 3 for horizontal polarization. The effect of wedges and breakers is less important than Bragg scattering by a factor of 2 or 3 for vertical polarization.

Nevertheless, backscatter from wedges and breakers is greater for vertical polarization than for horizontal polarization, as is shown by the column $(\sigma_{VV}^0/\sigma_{HH}^0)_{dB}$ for the effect of turbulence T, wedges W, and hydraulic jumps J for the three highest winds in the 67° incidence angle group. The polarization ratios for wedges are 7.1, 5.7, and 4.9 dB, and those for hydraulic jumps are 3.7, 2.9, and 3.0 dB. One would not expect the nearly perfect wedges of the *Kwoh and Lake* [1984] experiment, so that these ratios are somewhat lower than their experimental results. The hydraulic jump values are close to those reported by *Banner and Fooks* [1985].

Although these effects are relatively small for vertical polarization, they remove much of the bias found in Table 7, since four of the 67° circle flights for vertical polarization would be essentially within $\pm\sigma^0 E$ of the measured values.

For Table 17, the nine values that can be compared give the result for horizontal polarization at incidence angles near 58° that the Bragg model is biased low by −3.80 dB, with an rms variability of 4.07 dB and a standard deviation of 1.53 dB relative to the measured values. The estimated effects of breakers and wedges yield an overall bias of −0.13 dB, an rms variability of 0.61 dB, and a standard deviation of 0.63 dB. For the six values for vertical polarization, the corresponding values are −1.17, 1.47, and 0.96 dB for the Bragg values and 0.03 dB (bias), 0.38 dB (rms), and 0.42 dB (standard deviation) when the effects of breakers and wedges are included. At 67°, for the 12 values that can be compared for horizontal polarization, the values are −4.7 dB (bias), 5.02 dB (rms), and 1.85 dB (standard deviation) when the Bragg model is compared with the measured values. When wedges and breakers are included as in σ_{BBW}^0, the corresponding values are +0.02, 0.76, and 0.79 dB. Similarly, for vertical polarization, they are −0.78 dB (bias), 1.34 dB (rms), and 1.14 dB (standard deviation) for Bragg versus measured and +0.47, 0.81, and 0.64 dB with wedges and breakers included.

One might object to the above results, since values for the effect of breakers and wedges have merely been added to the Bragg values to get values close to the observed values, but the results of this simple calculation correlate well with laboratory measurements, confirm the suggestion of *Lyzenga et al.* [1983], and reinforce the conclusions of both *Kalmykov and Postovoytenko* [1976] and *Lewis and Olin* [1980]. At high incidence angles of 58° to 67°, these effects are important.

The values from Table 17 for vertical polarization at an incidence angle of 67° and for σ_J^0, which represent the normalized backscattering cross section from the spilling breakers in a wind sea looking upwind, can be combined with the results of *Wetzel* [1986], who estimated the cross section from a single breaker as an isolated target to be 1 m^2. For example, for a wind speed of 8.9 m s^{-1}, σ_J^0 is 1.3×10^{-4} and the reciprocal is 7692. Thus one spilling breaker for each 7692 m^2 of the radar wave front would be needed. Projected onto the sea surface for this incidence angle, the area involved would be 19,686 m^2. For an area 140 m by 140 m, one active spilling breaker with dimensions appropriate to K_u band with a cross section of 1 m^2 would result. For the 10.5, 12.3, and 16 m s^{-1} winds of the table, there would need to be one spilling breaker for a square area 38 by 38 m, 49 by 49 m, and 25 by 25 m, respectively. From Table 2, the area under the gravity wave spectrum for the 10.5 m s^{-1} wind was about 40% greater than that under the spectrum for the 12.3 m s^{-1} wind. There may well have been more breakers and wedges when the wind was 10.5 m s^{-1}.

Figure 30 is a graph of the values of σ_T^0, σ_W^0, and σ_J^0 in Table 17 for incidence angles near 67°. The amounts to be added to the Bragg backscatter values are substantial, especially for horizontal polarization relative to the Bragg values. Except for large values for the 10.5 m s^{-1} wind, the values increase with increasing wind speed.

These values seem to be reasonable, but at present there is no way to check them. One possible way to gain an understanding of these effects is suggested in section 11.5.

The same calculations were done for wind speeds of 11.3 m s^{-1} and greater for incidence angles near 40°, as in Table 18. For this incidence angle, the polarization ratio is only about 2 to 3 dB according to Kwoh and Lake. No effect of breakers and wedges for vertical polarization could be found except for the highest waves for 19.4 m s^{-1} winds. Even for horizontal polarization, the effect of breakers and wedges was much less than the Bragg values as shown in the column for $(\sigma_{BW}^0/\sigma_B^0)_{dB}$, where wave height and wind speed each have an effect. These relatively small effects for breakers and wedges are sufficient to bring about an agreement between the σ_{BBW}^0 and the σ^0 measured values within $\pm\sigma^0 E$.

From Table 18, for horizontal polarization for incidence angles near 40° for 18 values, the Bragg model was biased low by −1.49 dB, with an rms value of 1.91 dB and a standard deviation of 1.84 dB. The estimated effects of breakers and wedges resulted in a bias of −0.15 dB, an rms variability of 0.66 dB, and a standard deviation of 0.66 dB.

Figure 31 shows the values of σ_T^0, σ_W^0, and σ_J^0 for horizontal polarization for incidence angles near 40°. The erratic

Horizontally and Vertically Polarized Backscatter for Incidence Angles Near 40°

σ^0 Measured			$\sigma^0 + \sigma^0 E$ Measured			$(\sigma_{BW}{}^0/\sigma_B{}^0)_{dB}$			$(\sigma_{VV}{}^0/\sigma_{HH}{}^0)_{dB}$			Wave Height, m
UP	CR	DN	UP	CR	DN	UP	CR	DN	T	W	J	
17.70	4.55	9.98	19.10	8.11	11.02	−8.6	−13.1	−17.1				1.8
26.97	6.49	16.44	29.17	7.67	19.77	−3.7	−3.8	−5.4				1.5
36.06	11.85	22.18	39.17	12.85	24.15	−7.8	−7.1	−8.9				2.5(4.3)
40.17	11.94	26.06	43.45	13.64	28.44	−4.3	−3.6	−4.5				3.8(1.8)
40.46	12.25	24.72	44.36	13.06	27.04	−4.0	−4.4	−5.2				5.5/6.0
76.03	26.53	46.77	82.60	30.62	50.82	−3.0	−2.0	−3.0	0.7	−0.2	+1.3	5/5.5
111.42	42.27	81.66	121.62	46.13	87.70	−7.0	−3.7	−7.0				5/5.5

behavior is partially explainable as an effect of the variations in wave height for the various wind speeds. Near 15.7 and 16.0 m s^{-1}, $\sigma_W{}^0$ for 67° is 0.5×10^{-3}, and for 40° it is 3.2×10^{-3} for an increase of 8 dB, which is reasonable compared with the scatter in the data of Kwoh and Lake. Families of curves for $\sigma_T{}^0$, $\sigma_W{}^0$, and $\sigma_J{}^0$ as functions of wind speed with wave height as a parameter could be used to refine the predicted backscatter values, given sufficient data.

The various sources of scatter in the data for vertical polarization in terms of $\pm\sigma^0 E$ and $\bar{U} \pm 1$ at an incidence angle of 40° for winds above 11 m s^{-1} and below 16 m s^{-1} amount to values ranging from about −0.005 to +0.015 in antilog form as computed from Tables 6 and 8. Moreover, for wedges the polarization ratio is only 2 to 3 dB. The possible effects of breakers and wedges for this range of wind and wave conditions cannot be detected in the vertical polarization data because of these sources of variability. Moreover, the data scatter above and below the theoretical curves because of these uncertainties.

A polarization ratio close to 0 dB as suggested by the backscatter values for the 19.4 m s^{-1} wind in Table 18 would mean that the additional effect of breakers and wedges for vertical polarization at 40° incidence angle would have a smaller effect than at the higher incidence angles. Section 5.3 describes one of the other mechanisms for upwind/downwind backscatter differences that are complementary to these effects especially for lighter wind.

The use of the same parameter defined in section 5.3, which accounts for upwind/downwind differences for vertical polarization and which was used to tune the model, does not explain the much larger upwind/downwind difference for horizontal polarization, although it does yield somewhat larger differences for horizontal polarization compared with vertical polarization. Hydraulic jumps associated with spilling breakers are an alternate possible explanation.

10.6. *A Synthesis*

Wright [1966] showed that backscattering from capillary waves in the absence of breaking waves and wedges followed the Bragg-scattering theory and was proportional to the square of the amplitude of the waves. *Valenzuela* [1978] has reviewed the methods for treating specular reflection. *Kwoh and Lake* [1984] showed that wedges produced backscatter in the absence of wind, Bragg waves, and breaking waves and that the results agreed with an appropriate theory. *Banner and Fooks* [1985] showed that spilling breakers produced backscatter from the turbulent undulations originating on the spilling region and the toe of the breaker as opposed to wedges and wind-generated Bragg waves.

The second point made by *Kwoh and Lake* [1984] in their conclusions with reference to possible objections to their study was that "The short gravity waves we have investigated are artificially devoid of high-frequency Bragg waves, which should be more prevalent on a natural wind-generated surface like the ocean, i.e. our investigation may be irrelevant to ocean scattering." To the contrary, the effect of wedges is one of the five effects that our study indicates need to be considered to explain radar backscatter for both vertical and horizontal polarization over the full range of incidence angles from 20° to 67°.

Theoretical calculations by *Wetzel* [1986] provide a way to study breakers in term of electromagnetic theory. The roughness factor described by *Wetzel* [1986] can be used to improve wedge-scattering theory.

By isolating each effect from the others, the five papers cited above have shown that each produces backscatter, and our analysis, with a two-scale viscosity-dependent Bragg-scattering model for a starting point, shows that specular reflection especially for low winds cannot be neglected near an incidence angle of 20° and that the effects of wedges and spilling breakers (hydraulic jumps and turbulence) can provide the needed corrections to explain the biases in a Bragg model for 40°, 58°, and 67° incidence angles for horizontal polarization and for 58° and 67° incidence angles and high winds and waves at 40° for vertical polarization. No single effect is sufficient to explain the observed backscatter for the entire range of incidence angles of importance to remote sensing.

11. Two-Scale Bragg Model Results for L, C, X, and K_a Bands

11.1. *Introduction*

In the preceding material it was shown that the two-scale Bragg-scattering model developed in sections 2 to 6 yielded results that agreed with the circle flight data for K_u band quite well for incidence angles near 40° for vertical polarization even for a data set that did not correspond to the fully developed seas of the model. For incidence angles near 20°, departures from the model spectrum become important to account for specular reflection, and for higher incidence angles the contribution from wedges and breaking waves needs to be considered for both vertical and horizontal polarization. The contributions from wedges and breaking waves are, in essence, corrections to be added to the Bragg model, especially for vertical polarization since they are small relative to the Bragg

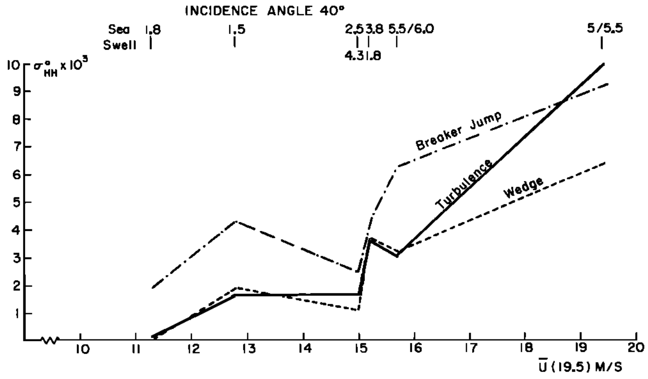

Fig. 31. Estimated contributions to the total backscatter for horizontal polarization from breakers and wedges at incidence angles near 40°.

backscatter. For horizontal polarization, wedges and breakers are much more important and are probably the main explanation for the large upwind/downwind differences for horizontal polarization.

11.2. *General Results for L, C, X, and K_a Bands*

The two-scale Bragg model was applied to calculate backscatter for *L*, *C*, *X*, and K_a band radars. In this section the results for upwind vertical polarization are described. Figures 32, 33, and 34, and 35 are for these four different radar wave numbers. The parameters chosen for K_u band were used throughout with $\varepsilon = 1$ (section 5.3), $\Gamma = 40$ (section 5.6), and the remaining values given in section 5.4. The figures should be compared not only with each other but also with Figure 9 and with Figures 4 and 5. The values for the complex dielectric constants that were used are given in Table 19.

An overview of Figures 32, 33, 34, 9, and 35 shows that backscatter varies by a greater amount with increasing radar wave number for wind speeds from 4 to 20 m s^{-1} from *L* to K_u band. For increasing radar wave number, the curves become less and less like a power law, and the effect of water temperature becomes more and more important. There is no indication of saturation at *L* band. *C* band saturates at such high winds that the predicted effect may never be verified. *X* band saturates at wind speeds somewhat greater than those for K_u band. The effects of breakers and wedges for such high winds and high waves might cause the curves to continue to increase despite the decrease in the Bragg-scattering waves. This is especially so for horizontal polarization.

The size of the wedges and breakers needed to produce backscatter varies as the radar wavelength. *Kwoh and Lake* [1984] used 15 radar wavelengths, $-7.5\lambda_e$ to $+7.5\lambda_e$ for their theoretical calculations at *X* band, so that the wedge was about 45 cm in width. In proportion, a wedge at *L* band would need to be about 352 cm wide, at *C* band it would have to be 85 cm wide, at K_u band only 30 cm wide, and at K_a band a mere 13 cm. The number of wedges will increase with increasing wave number, and the longer-wavelength radars will not respond to many of the smaller ones as wedges. Correspondingly larger spilling breakers will also be needed. If treated as a right angle at the hydraulic jump, the dimensions for each side might be comparable to one half of the lengths given above. Wedges and spilling breakers certainly occur in wind-generated waves with all of the above dimensions for high winds and high waves.

The range of wind speeds for which the effects of wedges and spilling breakers would be relatively less important than Bragg scattering would increase with increasing radar wavelength.

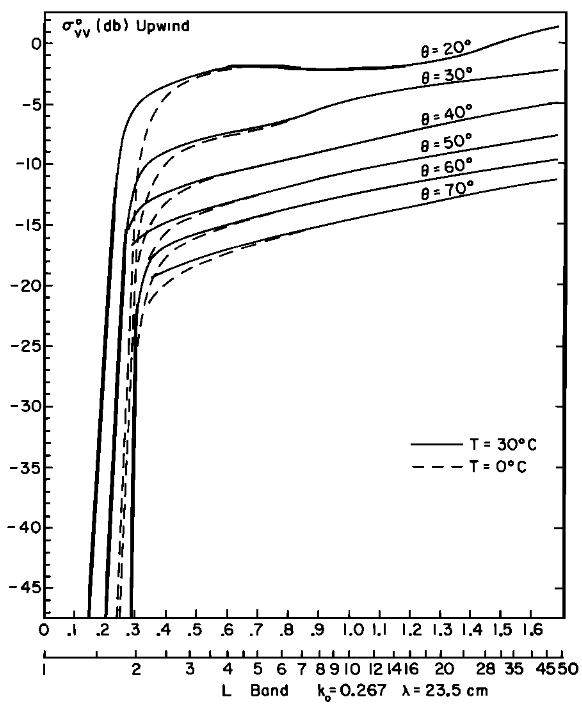

Fig. 32. Vertically polarized backscatter for the two scale model for *L* band at upwind with $\log_{10} \bar{U}(19.5)$ in meters per second on the abscissa and $\sigma_{VV}{}^0$ in decibels on the ordinate. The solid curves are for a water temperature of 30°C, and the dashed curves are for a water temperature of 0°C; θ is the incidence angle. The auxiliary scale is the wind speed at 19.5 m in meters per second.

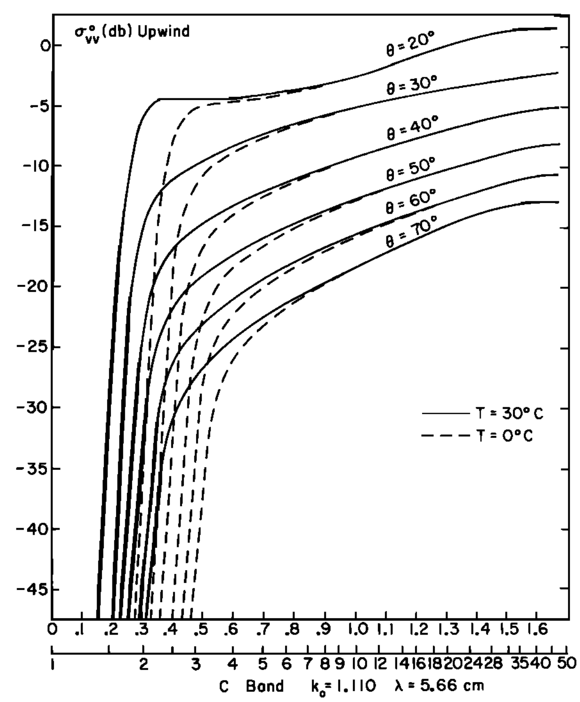

Fig. 33. Same as Figure 32 except for *C* band.

11.3. *L Band*

L band backscatter, for a two-scale model except for the sharp drop near 2 to 3 m s^{-1} and at a 20° incidence angle, is fairly close to a power law. Not all of the curves for very light winds are graphed because the curves cross back and forth owing to the behavior of the critical wind speed shown in Figure 5. At a 40° incidence angle, a power law model for upwind would result in

$$\sigma_{VV(\mathrm{dB})}{}^{0} = 10(-1.405 + 0.58 \log_{10} \bar{U}(19.5)) \qquad (67)$$

For the Seasat 1 SAR, *L* band data for swaths with incidence angles from 20° to 26°, according to *Thompson et al.* [1983], the wind speed power law is given by 0.5 ± 0.1 with a very weak dependence on cos 2χ and no detectable dependence on cos χ. Specular backscatter has strange effects in this incidence angle range according to Figure 32, but the power law for winds above 4 m s^{-1} is very little changed from 30° to 70° incidence angles, whereas the level drops by 10 dB. Aspect angle calculations with the model also show this weak dependence on cos 2χ and little, if any, upwind/downwind difference for vertical polarization.

11.4. *C Band*

The effects of water temperature on *C* band according to the model as in Figure 33 are most pronounced for winds under 3 m s^{-1}, but they should be detectable for winds up to 6 or 7 m s^{-1}. A power law fit for incidence angles of 40° and higher would do moderately well above 5 m s^{-1} for winds to as high as those for which *C* band backscatter has been measured to date. The power laws for *C* band have been found to be somewhat lower than those for K_u band and higher than the 0.5 ± 0.1 power law for *L* band. There really is no power law for the full range of wind speeds, water temperatures, and wave development to be expected over the ocean.

In the design of scatterometers, these results suggest that

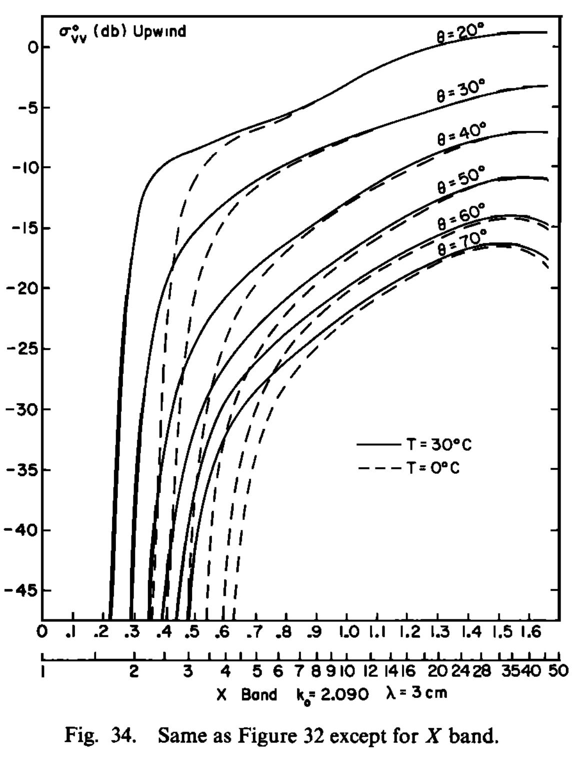

Fig. 34. Same as Figure 32 except for *X* band.

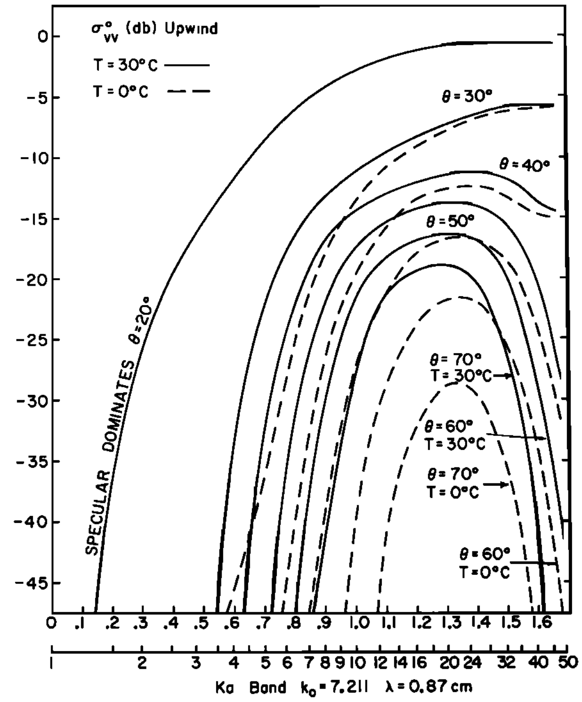

Fig. 35. Same as Figure 32 except for K_a band.

aircraft data used to develop a model function will require conventional data on the spectra of the waves as well as accurate wind data. Some of the difficulties in obtaining accurate wind observations, especially near a coastline, have been described by R. Ezraty of the Institut de Recherche pour l'Exploitation de la Mer, Centre de Brest, France (personal communcation, 1986), who leads a group responsible for in situ wind measurements for the European remote sensing satellite (ERS) 1 and *C* band aircraft measurements of backscatter. They find for example that the values for the standard deviations of 2-, 8.5-, and 30-min wind averages relative to a 60-min average are about 50% greater than those calculated by *Pierson* [1983].

Since the variation of backscatter with wind speed is weaker than for *X* band and K_u band, the backscatter will have to be measured more accurately to obtain comparable accuracy in wind recovery algorithms. On the other hand, high-wind speed saturation may be less of a problem.

11.5. *X Band*

For *X* band (Figure 34) the effect of water temperature is very important for winds under 5 m s^{-1}. Water temperature can produce effects over a considerable range of wind speeds depending on incidence angle and can result in differences of about a meter per second for the same backscatter value for the higher incidence angles.

Some interesting results might be obtained by comparing simultaneous wave images for vertical and horizontal polarization with both upwind and downwind passes for a real aperture radar at *X* or K_u band. A color composite such as that of *Ulaby et al.* [1986] might reveal interesting features of the wave pattern, in particular the distribution of non-Bragg scatterers.

11.6. K_a *Band*

The strangest results of all from the two-scale model are those for K_a band as shown in Figure 35. At a 70° incidence

TABLE 19. Frequencies, Wavelengths, and Dielectric Constants Used in Each Radar Band

Band	Frequency, GHz	Wave Number, cm^{-1}	Wave-length, cm	Dielectric Constant*
L	1.275	0.267	23.50	$72 - i59.0$
C	5.3	1.110	5.66	$60 - i36.0$
X	10.0	2.090	3.00	$49 - i35.5$
K_u (RADSCAT)	13.9	2.911	2.16	$39 - i38.5$
K_u (SASS)	14.6	3.058	2.05	$39 - i38.5$
K_a	34.43	7.211	0.87	$16 - i24.5$

*Values taken from *Saxton and Lane* [1952] for seawater at 10°C.

angle the Bragg wave would be 5 mm long. The combined effect of viscosity and a wind at 2.5 mm above the surface result in no Bragg backscatter for winds under 7 m s^{-1} over 30°C water and none for winds under 12 m s^{-1} for 0°C water. The effect of a decreasing wind at small heights above the surface for an increasing wind at 10 m produces saturation for winds in the 16 to 24 m s^{-1} range, and backscatter then decreases with increasing wind speed. The recovery at extremely high winds is due to the contribution from specular reflection. Wedges with widths of 13 cm are probably quite frequent, but a sharp enough corner for them to be effective may not be possible for radar waves about 8.7 mm long because of surface tension. Similarly, very small spilling breakers of the dimensions needed to produce additional backscatter may be rare. The entire question of backscatter from K_a band is open.

12. CONCLUDING REMARKS

Over the last 2 decades, scatterometry has demonstrated its potential for providing remote oceanic winds for assimilation in large-scale oceanic and atmospheric models and for other uses such as wave forecasting. The connection between observed radar backscatter and surface wind has been based on empirical fits without recourse to theoretical arguments on the response of surface waves to the near-surface wind. This work is an attempt to fill that gap.

A model for the response of waves in the gravity-capillary equilibrium region of the spectrum was proposed on the basis of a local (in wave number) balance between wind input and dissipation. The wind input function was constructed on the basis of laboratory observations of shortwave growth guided by field studies of longer waves. The dissipation function was developed from ideas of viscous dissipation and wave breaking in response to local accelerations and modified by kinematic effects of phase and group velocity differences. The resulting equilibrium spectrum was appended to an observed fully developed spectral form, and the complete spectrum was integrated to yield upwind and cross-wind slope variances as functions of wind speed and cutoff wave number. These slope variances were used in a two-scale model to prescribe the distribution (Gaussian) of tilted patches of Bragg scatterers on the ocean surface and to determine the degree of specular reflection.

At any given wave number the fully developed equilibrium spectrum depends only on the neutral equivalent wind speed and water temperature. At low wind speeds the wind input term may be insufficient to overcome temperature dependent viscous dissipation, and until a threshold wind speed is crossed, backscatter levels will be undetectable by present means from spacecraft. Since this threshold is water temperature dependent, failure to include viscosity effects would lead to a distribution of calm winds that is biased to areas of cold water and that depends on wavelength and hence radar frequency and incidence angle. Recent laboratory work in light winds validates the water temperature effects of the model.

The empirical parameters that determine the separation of scales between scattering waves and tilting waves, the modulation of the one by the other, and the rate of dissipation are tuned by comparison with the most accurate 24 runs of the very well documented radar scatterometer work of *Schroeder et al.* [1984]. Further comparisons with an additional 29 runs demonstrate the model's accuracy for vertically polarized backscatter. In general, when reported errors in the wind measurements and in the backscatter noise levels are considered, the model shows excellent agreement with the data. The combination of low winds and low incidence angle sometimes indicates that the model underpredicts, but these conditions are particularly susceptible to enhanced backscatter from swell propagating from elsewhere.

One aspect of this model that is particularly important in the context of global remote anemometry is the saturation and eventual decay of Bragg-backscattered power at high wind speeds. This could lead to ambiguity in the estimation of high winds for high radar frequencies and incidence angles. It is demonstrated that scattering by wedges and breakers may become relatively important at high wind speeds and wave numbers and will tend to reduce the tendency of the backscatter to saturate. This is particularly true of horizontally polarized backscatter, where these additional effects may dominate at high wind speeds.

It was found that the corrections required to bring the model's backscatter at high wind speeds into agreement with the data showed general agreement with four independent theoretical and laboratory studies both with regard to the wind speed dependence of the backscatter from wedges and breakers and with their polarization ratios.

It would seem that this approach to scatterometry modeling is fruitful and capable of good fidelity with observations in the ranges of wind speed, radar frequency, and incidence angle where specular and Bragg scattering dominate. Further development is needed to permit incorporation of backscatter due to wedges and breakers.

Finally, the model is exercised at L, C, X, and K_a bands to demonstrate the differences in wind speed and water temperature sensitivity. In subsequent research we will test the model against observations in these radar bands if such become available. By covering wide ranges of wave number and wind speed, we will be able to refine the model and perhaps, in so doing, improve our understanding of scatterometry and of the energy balance in the equilibrium ranges of spectra at various stages of development.

Acknowledgments. M. A. Donelan was a guest of the Max-Planck-Institut für Meteorologie, Hamburg, Federal Republic of Germany, and the recipient of a research fellowship from the Alexander von Humboldt Stiftung, Bonn, during the early part of this work. He wishes to thank both these organizations for their hospitality and generosity. Conversations with P. Woiceshyn at the start of our investigation concerning the effects of water temperature were helpful. K. Kahma provided valuable insight for the interpretation of the concept of a threshold wind. L. C. Schroeder gave us valuable help in interpreting the AAFE RADSCAT circle flight measurements and provided additional unpublished details on the calibration procedures for this instrument, which were done under the direction of W. L. Jones with the help of M. Komen and R. Segura as well as the authors of the data reports cited herein. His comments on draft portions of this paper were incorporated in the final version. Discussions with M. Banner at the end of this study provided clarifications of his research. W. Plant raised some questions concerning aspects of the model. We appreciate his interest and have extended our discussion of these aspects. The help of W. B. Sylvester in carrying out some of the needed calculations at City College is acknowledged. The City College contribution to this research was supported by NASA grant NAGW-690. The reviews of this paper, both as originally submitted and as finally submitted, are appreciated. Errors have been corrected, and changes have been made to improve the paper on the basis of the reviews.

REFERENCES

Al-Zanaidi, M. A., and W. H. Hui, Turbulent air flow over water waves—A numerical study, *J. Fluid Mech.*, *148*, 225–246, 1984.

Atlas, D., R. C. Beal, R. A. Brown, P. DeMay, R. K. Moore, C. G. Rapley, and C. Swift, Problems and future directions in remote sensing of the oceans and troposphere: A workshop report, *J. Geophys. Res.*, *91*(C2), 2525–2548, 1986.

Badgley, F. I., C. A. Paulson, and M. Miyake, Profiles of wind, temperature and humidity over the Arabian Sea, 62 pp., University Press of Hawaii, Honolulu, 1968.

Banner, M. L., Surging characteristics of spilling regions of quasi-steady breaking water waves, *Appl. Math. Prepr. AM 86/1*, 38 pp., Univ. of N. S. W., Kensington, Australia, 1985.

Banner, M. L., and E. H. Fooks, On the microwave reflectivity of small-scale breaking water waves, *Proc. R. Soc. London, Ser. A*, *399*, 93–109, 1985.

Barrick, D. E., and W. H. Peake, A review of scattering from surfaces with different roughness scales, *Radio Sci.*, *3*, 865–868, 1968.

Benjamin, T. B., Shearing flow over a wavy boundary, *J. Fluid Mech.*, *6*, 161–205, 1959.

Bjerkaas, A. W., and F. W. Reidel, Proposed model for the elevation spectrum of a wind-roughened sea surface, *Rep. APL-TG-1328-I-31*, 31 pp., Appl. Phys. Lab., Johns Hopkins Univ., Laurel, Md., 1979.

Black, P. G., R. C. Gentry, V. J. Cardone, and J. D. Hawkins, SEASAT microwave wind and rain observations in severe tropical and mid-latitude marine storms, *Adv. Geophys.*, *27*, 197–277, 1985.

Bretschnieder, C. L., H. J. Crutcher, J. Darbyshire, G. Neumann, W. J. Pierson, H. Walden, and B. W. Wilson, Data for high wave conditions observed by the OWS "Weather Reporter" in Dec. 1959, *Dtsch. Hydrogr. Z.*, *15*(6), 243–255, 1962.

Britt, C. L., and L. C. Schroeder, SASS-I model function evaluation and upgrade, *Eur. Space Agency Spec. Publ. ESA SP-215*, 623–629, 1984.

Brown, R. A., On a satellite scatterometer as an anemometer, SEASAT II, Scientific results, *J. Geophys. Res.*, *88*(C3), 1663–1673, 1983.

Cardone, V. J., Specification of the wind field distribution in the marine boundary layer for wave forecasting, Ph.D. dissertation, 131 pp., New York Univ., N. Y., 1969. (Available as NTIS AD702490 from Natl. Tech. Inf. Serv., Springfield, Va.)

Chan, H. L., and A. K. Fung, A theory of sea scatter at large incident angles, *J. Geophys. Res.*, *82*(24), 3439–3444, 1977.

Chia, R. C., The theory of radar backscatter from the sea, Ph.D. thesis, 120 pp., Univ. of Kans., Lawrence, 1968.

Cox, C. S., Measurements of slopes of high-frequency wind waves, *J. Mar. Res.*, *16*, 199–225, 1958.

Cox, C. S., and W. Munk, Statistics of the sea surface derived from sun glitter, *J. Mar. Res.*, *13*, 198–227, 1954.

Crapper, G. D., An exact solution for progressive capillary waves of finite amplitude, *J. Fluid Mech.*, *2*(6), 532–540, 1957.

Delnore, V. E., G. S. Bahn, W. L. Grantham, R. F. Harrington, and W. L. Jones, Active and passive microwave measurements in hurricane Allen, *NASA Tech. Memo, TM-86390*, 138 pp., 1985.

Donelan, M. A., The dependence of the aerodynamic drag coefficient on wave parameters, in *Proceedings of the First International Conference on Meteorology and Air Sea Interaction of the Coastal Zone*, pp. 381–387, American Meteorological Society, Boston, Mass., 1982.

Donelan, M. A., and W. J. Pierson, Does the scatterometer see wind speed or friction velocity?, *NASA Conf. Publ., CP 2303*, 75–87, 1984.

Donelan, M. A., M. S. Longuet-Higgins, and J. S. Turner, Whitecaps, *Nature*, *239*(5373), 449–451, 1972.

Donelan, M. A., J. Hamilton, and W. H. Hui, Directional spectra of wind generated waves, *Philos. Trans. R. Soc. London, Ser. A*, *315*, 509–562, 1985.

Dorsey, N. E., Properties of ordinary water-substance, *ACS Monogr.*, *81*, 673 pp., 1940.

Duffy, D. G., and R. Atlas, The impact of SEASAT-A scatterometer data on the numerical prediction of the QE-II storm, *J. Geophys. Res.*, *91*(C2), 2241–2248, 1986.

Durden, S. L., and J. E. Vesecky, A physical radar cross section model for a wind driven sea with swell, *IEEE J. Oceanic Eng.*, *OE-10*(4), 445–451, 1985.

Forristall, G. Z., Measurements of a saturated range in ocean wave spectra, *J. Geophys. Res.*, *86*(C9), 8075–8084, 1981.

Fung, A. K., and K. K. Lee, A semi-empirical sea spectrum model for scattering coefficient estimation, *IEEE J. Oceanic Eng.*, *OE-7*, 166–176, 1982.

Garratt, J. R., Review of drag coefficients over oceans and continents, *Mon. Weather Rev.*, *105*, 915–929, 1977.

Guinard, N. W., and J. C. Daley, An experimental study of a sea clutter model, *Proc. IEEE*, *58*(4), 543–550, 1970.

Guinard, N. W., J. T. Ransone, Jr., and J. C. Daley, Variation of the NRCS of the sea with increasing roughness, *J. Geophys. Res.*, *76*, 1525–1538, 1971.

Haimbach, S. P., and J. Wu, Directional slope distributions of wind-disturbed water surface, *Radio Sci.*, *21*(1), 73–79, 1986.

Hasselmann, D., J. Bosenberg, M. Dunckel, K. Richter, M. Grunewald, and H. Carlson, Measurements of wave induced pressure over surface gravity waves, in *Wave Dynamics and Radio Probing of the Ocean Surface*, edited by O. M. Phillips and K. Hasselmann, pp. 353–368, Plenum, New York, 1986.

Hsiao, S. V., and O. H. Shemdin, Measurements of wind velocity and pressure with a wave follower during MARSEN, *J. Geophys. Res.*, *88*(C14), 9841–9849, 1983.

Hsu, C. T., E. Y. Hsu, and R. L. Street, On the structure of turbulent flow over a progressive water wave: Theory and experiment in a transformed, wave following co-ordinate system, *J. Fluid Mech.*, *105*, 87–117, 1981.

Jackson, F. C., W. T. Walton, and P. L. Baker, Aircraft and satellite measurements of ocean wave directional spectra using scanning-beam microwave radar, *J. Geophys. Res.*, *90*(C1), 987–1004, 1985*a*.

Jackson, F. C., W. T. Walton, and C. Y. Peng, A comparison of in situ and airborne radar observations of ocean wave directionality, *J. Geophys. Res.*, *90*(C1), 1005–1018, 1985*b*.

Jeffreys, H., On the formation of waves by wind, *Proc. R. Soc. London, Ser. A*, *107*, 189–206, 1924.

Jeffreys, H., On the formation of waves by wind, II, *Proc. R. Soc. London, Ser. A.*, *110*, 341–347, 1925.

Jones, W. L., and L. C. Schroeder, Radar backscatter from the ocean: Dependence on surface friction velocity, *Boundary Layer Meteorol.*, *13*, 133–149, 1978.

Jones, W. L., L. C. Schroeder, and J. L. Mitchell, Aircraft measurements of the microwave scattering signature of the ocean, *IEEE J. Oceanic Eng.*, *OE-2*(1), 52–61, 1977.

Jones, W. L., L. C. Schroeder, D. H. Boggs, E. M. Bracalente, R. A. Brown, G. J. Dome, W. J. Pierson, and F. J. Wentz, The SEASAT-A satellite scatterometer: The geophysical evaluation of remotely sensed wind vectors over the ocean, *J. Geophys. Res.*, *87*(C5), 3297–3317, 1982.

Kahma, K. K., A study of the growth of the wave spectrum with fetch, *J. Phys. Oceanogr.*, *11*, 1503–1515, 1981.

Kahma, K. K., and M. A. Donelan, A laboratory study of the minimum wind speed for wind wave generation, 34 pp., Can. Centre for Inland Waters, Burlington, Ont., 1987. (Available from M. A. Donelan, Can. Centre for Inland Waters, Burlington, Ont.)

Kalmykov, A. A., and V. V. Postovoytenko, On polarization features of radio signals scattered from the sea surface at small grazing angles, *J. Geophys. Res.*, *81*(12), 1960–1964, 1976.

Kawai, S., Generation of initial wavelets by instability of a coupled shear flow and their evolution to wind waves, *J. Fluid Mech.*, *9*, 661–703, 1979.

Keller, W. C., and J. W. Wright, Microwave scattering and the straining of wind-generated waves, *Radio Sci.*, *10*, 139–147, 1975.
Keller, W. C., W. J. Plant, and D. E. Weissman, The dependence of *X* band microwave sea return on atmospheric stability and sea state, *J. Geophys. Res.*, *90*(C1), 1019–1029, 1985.
Kinsman, B., *Wind waves: Their Generation and Propagation on the Ocean Surface*, 676 pp., Prentice Hall, Englewood Cliffs, N. J., 1965. (Reprinted by Dover, New York, 1984).
Kitaigorodskii, S. A., On the theory of the equilibrium range in the spectrum of wind generated gravity waves, *J. Phys. Oceanogr.*, *13*, 816–827, 1983.
Kitaigorodskii, S. A., and Yu. A. Volkov, On the roughness parameter of the sea surface and the calculation of momentum flux in the near water layer of the atmosphere, *Izv. Acad. Sci. USSR Atmos. Oceanic Phys.*, Engl. Transl., *1*, 973–988, 1965.
Kwoh, D. S. W., and B. M. Lake, A deterministic, coherent, and dual-polarized laboratory study of microwave backscattering from water waves, I, Short gravity waves without wind, *IEEE J. Oceanic Eng.*, *OE-9*(5), 291–308, 1984.
Lamb, H., *Hydrodynamics*, 6th ed., 738 pp., Cambridge University Press, New York, 1932. (Reprinted by Dover, New York, 1945.)
Large, W. G., and S. Pond, Open ocean momentum flux measurements in moderate to strong winds, *J. Phys. Oceanogr.*, *11*, 324–336, 1981.
Larson, T. R., and J. W. Wright, Wind-generated gravity-capillary waves: Laboratory measurements of temporal growth rates using microwave backscatter, *J. Fluid Mech.*, *70*, 417–436, 1975.
Lewis, R. L., and I. D. Olin, Experimental study and theoretical model of high resolution backscatter from the sea, *Radio Sci.*, *15*, 815–826, 1980.
Leykin, I. A., and A. D. Rozenberg, Sea-tower measurements of wind-wave spectra in the Caspian Sea, *J. Phys. Oceanogr.*, *14*(1), 168–176, 1984.
Liu, W. T., and W. G. Large, Determination of surface stress by SEASAT-SASS, *J. Phys. Oceanogr.*, *11*, 1603–1611, 1981.
Longuet-Higgins, M. S., The statistical analysis of a random moving surface, *Philos. Trans. R. Soc. London, Ser. A*, *249*(966), 321–387, 1957.
Longuet-Higgins, M. S., On the intervals between successive zeros of a random function, *Proc. R. Soc. London, Ser. A*, *246*, 99–118, 1958*a*.
Longuet-Higgins, M. S., The statistical distribution of the curvature of a random Gaussian surface, *Proc. Cambridge Philos. Soc.*, *55*, 91–100, 1958*b*.
Longuet-Higgins, M. S., The distribution of the sizes of images reflected in a random surface, *Proc. Cambridge Philos. Soc.*, *55*, 91–100, 1959.
Longuet-Higgins, M. S., Reflection and refraction at a random moving surface, I, Pattern and paths of specular points, *J. Opt. Soc. Am.*, *50*, 838–844, 1960*a*.
Longuet-Higgins, M. S., Reflection and refraction at a random moving surface, II, Number of specular points in a Gaussian surface, *J. Opt. Soc. Am.*, *50*, 845–850, 1960*b*.
Longuet-Higgins, M. S., Reflection and refraction at a random moving surface, III, Frequency of twinkling in a Gaussian surface, *J. Opt. Soc. Am.*, *50*, 851–856, 1960*c*.
Longuet-Higgins, M. S., The generation of capillary waves by steep gravity waves, *J. Fluid Mech.*, *16*(1), 138–159, 1963.
Longuet-Higgins, M. S., Parametric solutions for breaking waves, *J. Fluid Mech.*, *121*, 403–424, 1982.
Longuet-Higgins, M. S., and D. E. Cartwright, The statistical distribution of the maxima of a random function, *Proc. R. Soc. London, Ser. A*, *237*, 212–232, 1956.
Longuet-Higgins, M. S., and E. D. Cokelet, The deformation of steep surface waves on water, I, A numerical method of computation, *Proc. R. Soc. London, Ser. A*, *350*, 1–26, 1976.
Longuet-Higgins, M. S., and J. S. Turner, An entraining plume model of a spilling breaker, 1, *J. Fluid Mech.*, *63*, 1–20, 1974.
Lyzenga, D. R., A. L. Maffett, and R. A. Shuchman, The contribution of wedge scattering to the radar cross section of the ocean surface, *IEEE Trans. Geosci. Remote Sens.*, *GE-21*(4), 502–505, 1983.
Masuko, H., K. Okamoto, M. Shimada, and S. Niwa, Measurements of microwave backscattering signatures of the ocean surface using *X* band and K_a band airborne scatterometers, *J. Geophys. Res.*, *91*(C11), 13,065–13,083, 1986.
Michell, J. H., The highest waves in water, *Philos. Mag.*, *36*(5), 430–437, 1893.
Miles, J. W., On the generation of surface waves by shear flows, *J. Fluid Mech.*, *3*, 185–204, 1957.
Miles, J. W., On the generation of surface waves by shear flows, 2, *J. Fluid Mech.*, *6*, 568–582, 1959.
Mitsuyasu, H., and T. Honda, The high frequency spectrum of wind-generated waves, *Rep. Res. Inst. Appl. Mech. Kyushu Univ.*, *22*, 327–355, 1975.
Mitsuyasu, H., and T. Honda, Wind-induced growth of water waves, *J. Fluid Mech.*, *123*, 425–442, 1982.
Monahan, E. C., Oceanic whitecaps, *J. Phys. Oceanogr.*, *1*, 139–144, 1971.
Monahan, E. C., The ocean as a source for atmospheric particles, in *The Role of Air-Sea Exchange in Geochemical Cycling*, edited by P. Buat-Menard, pp. 129–163, D. Reidel, Hingham, Mass., 1986.
Monahan, E. C., and C. F. Monahan, The influence of fetch on whitecap coverage as deduced from the Alte Weser lightstation observer's log, in *Oceanic Whitecaps and Their Role in Air-Sea Exchange Process*, edited by E. C. Monahan and G. MacNiocaill, pp. 275–277, D. Reidel, Hingham, Mass., 1986.
Monahan, E. C., and I. G. O'Muircheartaigh, Optimal power-law description of oceanic whitecap coverage dependence on wind speed, *J. Phys. Oceanogr.*, *10*, 2094–2099, 1980.
Monahan, E. C., and I. G. O'Muircheartaigh, Improved statement of the relationship between surface wind speed and oceanic whitecap coverage as required for the interpretation of satellite data, in *Oceanography From Space*, edited by J. F. R. Gower, pp. 751–755, Plenum, New York, 1981.
Monahan, E. C., and I. G. O'Muircheartaigh, Whitecaps and the passive remote sensing of the ocean surface, *Int. J. Remote Sens.*, *7*, 627–642, 1986.
Monin, A. S., and A. M. Obukhov, Basic laws of turbulent mixing in the ground layer of the atmosphere, (in Russian), *Tr. Geofiz. Inst. Akad. Nauk SSSR*, *24*(151), 163–187, 1954.
Moore, R. K., and A. K. Fung, Radar determination of winds at sea, *Proc. IEEE*, *67*, 1504–1521, 1979.
Moskowitz, L., Estimates of the power spectrums for fully developed seas for wind speeds of 20 to 40 knots, *J. Geophys. Res.*, *69*(24), 5161–5179, 1964.
Neumann, G., and W. J. Pierson, *Principles of Physical Oceanography*, 545 pp., Prentice Hall, Englewood Cliffs, N. J., 1966.
Peteherych, S., M. G. Wurtele, P. M. Woiceshyn, D. H. Boggs, and R. R. Atlas, First global analysis of SEASAT scatterometer winds and potential for meteorological research, *NASA Conf. Publ. CP2303*, 575–585, 1984.
Phillips, O. M., On the generation of waves by turbulent wind, *J. Fluid Mech.*, *2*, 417–495, 1957.
Phillips, O. M., The equilibrium range in the spectrum of wind-generated waves, *J. Fluid Mech.*, *4*, 426–434, 1958.
Phillips, O. M., Spectral and statistical properties of the equilibrium range in wind-generated gravity waves, *J. Fluid Mech.*, *156*, 505–531, 1985.
Pierson, W. J., The measurement of the synoptic scale wind over the ocean, *J. Geophys. Res.*, *88*(C3), 1683–1708, 1983.
Pierson, W. J., A Monte Carlo comparison of the recovery of winds near upwind and downwind from the SASS-1 model function by means of the sum of squares algorithm and a maximum likelihood estimator, *NASA Contract. Rep.*, *CR*-3839, 62 pp., 1984.
Pierson, W. J., and L. Moskowitz, A proposed spectral form for fully developed wind seas based on the similarity theory of S. A. Kitaigorodskii, *J. Geophys. Res.*, *69*(24), 5181–5190, 1964.
Pierson, W. J., and R. E. Salfi, Monte Carlo studies of ocean wind vector measurements by SCATT: Objective criteria and maximum likelihood estimates for removal of aliases, and effects of cell size on accuracy of vector winds, *NASA Contract. Rep.*, *CR-165837-1*, 282 pp., 1982.
Pierson, W. J., and R. A. Stacy, The elevation slope, and curvature spectra of a wind roughened sea surface, *NASA Contract Rep.*, *CR-2646*, 126 pp., 1973.
Pierson, W. J., W. B. Sylvester, and R. E. Salfi, Synoptic scale wind field properties from the SEASAT-SASS, *NASA Contract. Rep.*, *CR-3810*, 152 pp., 1984.
Pierson, W. J., W. B. Sylvester, and M. A. Donelan, Aspects of the determination of winds by means of scatterometry and of the utilization of vector wind data for meteorological forecasts, *J. Geophys. Res.*, *91*(C2), 2263–2272, 1986.
Plant, W. J., A relationship between wind stress and wave slope, *J. Geophys. Res.*, *87*(C3), 1961–1967, 1982.

Plant, W. J., A two-scale model of short wind-generated waves and scatterometry, *J. Geophys. Res.*, *91*(C9), 10,735–10,749, 1986.
Reece, A. M., Jr., Modulation of short waves by long waves, *Boundary Layer Meteorol.*, *13*, 203–214, 1978.
Rice, S. D., Reflection of electromagnetic waves from slightly rough surfaces, *Commun. Pure Appl. Math.*, *4*, (2/3), 361–378, 1951.
Ross, D. B., V. J. Cardone, J. Overland, R. D. McPherson, W. J. Pierson, and T. W. Yu, Oceanic surface winds, *Adv. Geophys. 27*, 101–140, 1985.
Saxton, J. A., and J. A. Lane, Electrical properties of sea water, *Wireless Eng.*, *291*, 269–275, 1952.
Schlichting, J., *Boundary Layer Theory*, 6th ed., 747 pp., McGraw-Hill, New York, 1968.
Schooley, A. H., Profiles of wind-created water waves in the capillary-gravity transition region, *J. Mar. Res.*, *16*, 100–108, 1958.
Schroeder, L. C., and J. L. Mitchell, Archival of aircraft scatterometer data from AAFE RADSCAT missions, *NASA Tech. Memo, TM-84608*, 22 pp., 1983. (Available as NTIS TB 84-214543 from Natl. Tech. Inf. Serv., Springfield, Va.)
Schroeder, L. C., W. L. Grantham, J. L. Mitchell, and J. L. Sweet, SASS measurements of the K_u-band radar signature of the ocean, *IEEE J. Oceanic Eng.*, *OE-7*, 3–14, 1982*a*.
Schroeder, L. C., D. H. Boggs, G. J. Dome, I. M. Halberstam, W. L. Jones, W. J. Pierson, and F. J. Wentz, The relationship between wind vector and normalized radar cross section used to derive Seasat-A satellite scatterometer winds, *J. Geophys. Res.*, *87*, 3318–3336, 1982*b*.
Schroeder, L. C., W. L. Jones, P. R. Schaffner and J. L. Mitchell, Flight measurement and analysis of AAFE RADSCAT wind speed signature of the ocean, *NASA Tech. Memo.*, *TM 85646*, 144 pp., 1984.
Schroeder, L. C., W. L. Jones, P. R. Schaffner, and J. L. Mitchell, AAFE Radscat 13.9 GHz measurements and analysis: Wind speed signature of the ocean, *IEEE J. Oceanic Eng.*, *OE-10*(4), 346–357, 1985.
Smith, S. D., Eddy flux measurements over Lake Ontario, *Boundary Layer Meteorol.*, *6*, 235–255, 1974.
Snyder, R. L., F. W. Dobson, J. A. Elliott, and R. B. Long, Array measurements of atmospheric pressure fluctuations above surface gravity waves, *J. Fluid Mech.*, *102*, 1–59, 1981.
Sverdrup, H. U., M. W. Johnson, and R. H. Fleming, *The Oceans, Their Physics, Chemistry and General Biology*, 1087 pp., Prentice-Hall, Englewood Cliffs, N. J., 1942.
Thompson, T. W., D. E. Weissman, and F. J. Gonzalez, *L* Band radar backscatter dependence upon surface wind stress: A summary of new Seasat 1 and aircraft observations, *J. Geophys. Res.*, *88*(C3), 1727–1735, 1983.
Toba, Y., Local balance in the air-sea boundary processes, III, On the spectrum of wind waves, *J. Oceanogr. Soc. Jpn.*, *29*, 209–220, 1973.
Ulaby, F T., F. Kouyate, B. Brisco, and T. H. L. Williams, Textural information in SAR images, *IEEE Trans. Geosci. Remote Sens.*, *GE-24*(2), 235–246, 1986.
Valenzuela, G. R., Scattering of electromagnetic waves from a tilted slightly rough surface, *Radio Sci.*, *3*, 1057–1066, 1968.
Valenzuela, G. R., The growth of gravity-capillary waves in a coupled shear flow, *J. Fluid Mech.*, *76*, 229–250, 1976.
Valenzuela, G. R., Theories for the interaction of electromagnetic and oceanic waves—A review, *Boundary Layer Meteorol. 13*, 61–85, 1978.
Valenzuela, G. R., and M. B. Laing, Study of Doppler spectra of radar sea echo, *J. Geophys. Res.*, *75*(3), 551–563, 1970.
Valenzuela, G. R., M. B. Laing, and J. C. Daley, Ocean spectra for the high-frequency waves as determined from airborne radar measurements, *J. Mar. Res.*, *29*, 69–84, 1971.
Valenzuela, G. R., W. J. Plant, D. L. Schuler, D. T. Chen, and W. C. Keller, Microwave probing of shallow water bottom topography in the Nantucket shoals, *J. Geophys. Res.*, *90*(C3), 4931–4942, 1985.
Weast, R. C., *Handbook of Chemistry and Physics*, 50th ed., p. F-36, Chemical Rubber Company, Boca Raton, Fla., 1970.
Wentz, F. J., A two-scale scattering model with application to the JONSWAP '75 aircraft microwave scatterometer experiment, *NASA Contract Rep.*, *CR*-2919, 122 pp., 1977.
Wentz, F. J., Estimation of the sea-surface's two-scale backscatter parameters, *NASA Contract Rep.*, *CR*-145255, 122 pp., 1978.
Wentz, F. J., S. Peteherych, and L. A. Thomas, A model function for ocean radar cross sections at 14.6 GHz, *J. Geophys. Res.*, *89*(C3), 3689–3704, 1984.
Wentz, F. J., L. A. Mattox, and S. Peteherych, New algorithms for microwave measurements of ocean winds: Applications to Seasat and the special sensor microwave imager, *J. Geophys. Res.*, *91*(C3), 2289–2307, 1986.
Wetzel, L., On microwave scattering by breaking waves, in *Wave Dynamics and Radio Probing of the Oceans Surface*, edited by O. M. Phillips and K. Hasselmann, pp. 273–284, Plenum, New York, 1986.
Woiceshyn, P. M., S. Peteherych, M. G. Wurtele, D. H. Boggs, M. M. Borowski, G. F. Cunningham, A. Davies, and G. Muttitt, Cover photo: Seasat scatterometer marine wind analysis, *IEEE J. Oceanic Eng.*, *OE-10*(4), 342, 1985.
Woiceshyn, P. M., M. G. Wurtele, D. H. Boggs, L. F. McGoldrick, and S. Peteherych, The necessity for a new parameterization of an empirical model for wind/ocean scatterometry, *J. Geophys. Res.*, *91*(C2), 2273–2288, 1986.
Wright, J. W., Backscattering from capillary waves with application to sea clutter, *IEEE Trans. Antennas Propag.*, *AP-14*, 749–754, 1966.
Wright, J. W., A new model for sea clutter, *IEEE Trans. Antennas Propag.*, *AP-16*, 217–223, 1968.
Wright, J. W., and W. C. Keller, Doppler spectra in microwave scattering from wind waves, *Phys. Fluids*, *14*, 466–474, 1971.
Yaplee, B. S., A. Shapiro, B. D. Hammond, and E. A. Uliana, Nanosecond radar observations of the ocean surface from a stable platform, *IEEE Trans. Geosci. Remote Sens.*, *GE-9*, 170–174, 1971.

M. A. Donelan, National Water Research Institute, Canada Centre for Inland Waters, Burlington, Ontario, Canada L7R 4A6.

W. J. Pierson, Jr., Institute of Marine and Atmospheric Sciences, The City College, City University of New York, New York, NY 10031.

(Received April 12, 1986;
accepted October 13, 1986.)